SURFACE SPECTROSCOPIC CHARACTERIZATION OF OXIDE THIN FILMS AND BIMETALLIC MODEL CATALYSTS

A Dissertation

by

TAO WEI

Submitted to the Office of Graduate Studies of
Texas A&M University
in partial fulfillment of the requirements for the degree of

DOCTOR OF PHILOSOPHY

December 2006

Major Subject: Chemistry

SURFACE SPECTROSCOPIC CHARACTERIZATION OF OXIDE THIN FILMS AND BIMETALLIC MODEL CATALYSTS

A Dissertation

by

TAO WEI

Submitted to the Office of Graduate Studies of
Texas A&M University
in partial fulfillment of the requirements for the degree of

DOCTOR OF PHILOSOPHY

Approved by:

Chair of Committee,	D. Wayne Goodman
Committee Members,	Paul S. Cremer
	Simon W. North
	Donald G. Naugle
Head of Department	David H. Russell

December 2006

Major Subject: Chemistry

ABSTRACT

Surface Spectroscopic Characterization of

Oxide Thin Films and Bimetallic Model Catalysts.

(December 2006)

Tao Wei, B.S., University of Science and Technology of China

Chair of Advisory Committee: Dr. D. Wayne Goodman

Oxide thin films and bimetallic model catalysts have been studied using metastable impact electron spectroscopy (MIES), ultraviolet photoelectron spectroscopy (UPS), low energy ion scattering spectroscopy (LEISS), X – ray photoelectron spectroscopy (XPS), low energy electron diffraction (LEED), infrared reflection absorption spectroscopy (IRAS) and temperature programmed desorption (TPD) under ultra high vacuum (UHV) conditions. Of particular interest in this investigation was the characterization of the surface morphology and electronic/geometric structure of the following catalysts: SiO_2/Mo(112), Ag/SiO_2/Mo(112), Au–Pd/Mo(110), Au–Pd/SiO_2/Mo(110), and Pd–Sn/Rh(100). Specifically, different types of oxide surface defects were directly identified by MIES. The interaction of metal clusters (Ag) with defects was examined by work function measurements. On various Pd related bimetallic alloy surfaces, CO chemisorption behavior was addressed by IRAS and TPD. Observed changes in the surface chemical properties during the CO adsorption-desorption processes were explained in terms of ensemble and ligand effects. The prospects of translating this

molecular-level information into fundamental understanding of ‘real world’ catalysts are discussed.

DEDICATION

To my parents

ACKNOWLEDGMENTS

I would like to thank my advisor, Dr. D. Wayne Goodman from the bottom of my heart, for his guidance and support throughout the course of my studies. I am also grateful to Drs. Donald G. Naugle, Simon W. North, and Paul S. Cremer for serving on my evaluation committee. Thanks also go to Amy Liu for her secretarial help and Tony Montalbano, Ken Greer, Bill Merka, and Michael Tullos for their technical assistance.

I also want to extend my gratitude to my past and present co-workers in Dr. Goodman's research group with whom I have had the honor of working. Specificlly, I thank Drs. Young Dok Kim, Mingshu Chen, Sungsik Lee, Jinhai Wang, Stefan Wendt, Yifan Han, and Ashok Santra for being models of dedication and resourcefulness. I also thank my fellow students, namely Dr. Cheol Woo Yi, Dr. Luo Kai, Dr. Dheeraj Kumar, Dr. Jeffrey Stultz, Dr. Emrah Ozensoy, Dr. Byoung Koun Min, Yun Cai, Zhen Yan, Stephanus Axnanda, and Matthew Lundwall for their camaraderie and occasional insight. Finally, a special thanks goes to my parents for their constant support and encouragement throughout my long years of education.

Funding for this research has been provided by the Department of Energy, Office of Basic Energy Sciences, Division of Chemical Sciences and the Robert A. Welch Foundation.

TABLE OF CONTENTS

Page

ABSTRACT iii

DEDICATION v

ACKNOWLEDGMENTS vi

TABLE OF CONTENTS vii

LIST OF FIGURES ix

INTRODUCTION 1

Surface Science Studies on Model Catalysts Systems 2
Oxide Thin Film Methodology 4
Defects on Oxide Surfaces 6
Bimetallic Model Catalysts 8
Ensemble and Ligand Effects 10

EXPERIMENTAL 14

UHV Surface Analysis Chambers 14
Auger Electron Spectroscopy (AES) 21
Photoelectron Spectroscopy 21
Metastable Impact Electron Spectroscopy (MIES) 24
Low Energy Ion Scattering Spectroscopy (LEISS) 28
Low Energy Electron Diffraction (LEED) 28
Temperature Programmed Desorption (TPD) 30
Infrared Reflection Adsorption Spectroscopy (IRAS) 31
Sample and Doser Preparation 37

RESULTS AND DISCUSSION 39

SiO_2/Mo(112) 39
Direct Identification of Surface Defect Sites 45
Xe Adsorption 52
Ag/SiO_2/Mo(112) 63
Pd–Au/Mo(110) 73
XPS and LEISS 75
IRAS and TPD 85
Ensemble and Ligand Effects 98

Page

Alloy Film as a Model Catalyst System 104
Pd-Au/SiO_2/Mo(110) 111
Growth of Pd–Au Alloy Clusters 112
Surface Adsorption Sites 119
Pd–Sn/Rh(100) 136
LEED, LEISS and XPS 138
IRAS and TPD 147
Acetylene Trimerization to Benzene 154

CONCLUSIONS 162

REFERENCES AND NOTES 166

VITA 177

LIST OF FIGURES

Page

Figure 1. Schematic of MIES UHV analysis chamber..... 15

Figure 2. Schematic of IRAS UHV analysis chamber. 17

Figure 3. Schematic of the front view of ISS analysis chamber. 19

Figure 4. Diagram of photoemission process. 23

Figure 5. The principle de-excitation mechanisms in MIES. 25

Figure 6. Schematic of the home built MIES/UPS source. 27

Figure 7. Schematic of LEED optics. 29

Figure 8. Schematic diagram of the experimental configuration used in IRAS..... 32

Figure 9. Illustration of surface selection rule in IRAS experiments. (Adopted from Ref. [46].) 34

Figure 10. Schematical representation of $2\pi^*$ backdonation for adsorbed CO. 36

Figure 11. LEED pattern for a well ordered SiO_2 thin film supported on Mo(112). ... 40

Figure 12. AES spectrum for a SiO_2 thin film supported on Mo(112).. 40

Figure 13. MIES and UPS spectra for a low–defect SiO_2 thin film.. 41

Figure 14. A magnified view of the MIES spectrum in Fig.13a.. 43

Figure 15. A enlarged view of a MIES spectrum for a MgO thin film on Mo(100)..... 44

Figure 16. MIES and UPS spectra for a defective SiO_2 film before and after annealing at 1050 K. The defective film was prepared by deposition of Si onto a well-ordered SiO_2 film at room temperature, followed by oxidation at 800 K. Further annealing at 1050 K results in the disappearance of the defect state.. 47

Page

Figure 17. MIES spectra for a SiO_2 thin film before and after e-beam bombardments.. 48

Figure 18. MIES spectra for a SiO_2 thin film as a function of Si deposition at 300 K. 50

Figure 19. MIES for the SiO_2 thin films prepared by annealing at 1050 and 1200 K, respectively. An enlarged image of the lower energy region of both spectra is show at top right.. 51

Figure 20. UPS for the SiO_2 thin films prepared by annealing at 1050 and 1200 K, respectively..... 53

Figure 21. (a) UPS/PAX and (b) MIES/MAX spectra for MgO thin film on Mo(100).. 54

Figure 22. (a) UPS/PAX and (b) MIES/MAX spectra for SiO_2 thin film on Mo(112).. 56

Figure 23. MIES spectra of adsorbed Xe (MAX) from (a) SiO_2/Mo(112), (b) Mo(100), and (c) MgO/Mo(100).. 57

Figure 24. MIES and MAX for MgO surfaces with (a) low and (b) high defect densities. In (c), MAX spectra for both surfaces are compared. The high-defect surface was prepared by deposition of Mg in an O_2 background of 1 x 10^{-7} Torr at room temperature. The low defective surface was prepared by deposition of Mg in a O_2 background of 1 x 10^{-7} Torr at 600 K, followed by multiple anneals at 1150 K.. 59

Figure 25. MAX for low and high defect SiO_2 films on Mo(112).. 61

Figure 26. MIES spectra collected from a low-defect SiO_2 surface as a function of Ag exposure.. 64

Figure 27. UPS spectra collected from a low-defect SiO_2 surface as a function of Ag exposure. 65

Figure 28. (a) Changes in the intensities of the MIES O(2p)–AN and Ag (5s/5s) –AN features, and (b) work function from a low–defect surface as a function of Ag coverage as determined by the onset of secondary electrons in UPS. 67

Page

Figure 29. Work function changes for various SiO_2 surfaces as a function of Ag coverage determined by the onset of secondary electrons in UPS. The oxygen depleted surface was prepared by Si deposition on SiO_2, and the oxygen surplus surface was prepared by oxygen treatment of a Si/SiO_2 surface at 800 K. 70

Figure 30. Work function changes from UPS for low- and high-defect MgO surfaces as a function of Ag coverage. The high-defect MgO surface was produced by sputtering and heating the low-defect MgO surface to 600 K. 71

Figure 31. Core-level binding energy from XPS spectra of Au $4f_{7/2}$ (A) and Pd $3d_{3/2}$ (B) of 5ML Pd/5ML Au/Mo(110) (○) and 5ML Au/ 5ML Pd/Mo(110) (■) with respect to annealing temperature. 76

Figure 32. LEISS spectra of 5ML Pd/5ML Au/Mo(110) as a function of annealing temperature. LEISS spectra were collected at 300 K after the sample was annealed to the specified temperature. 78

Figure 33. Surface concentration of Au and Pd of 5ML Pd/5ML Au/Mo(110) (○) and 5ML Au/5ML Pd/Mo(110) (■)as a function of annealing temperature. The sample was annealed at each temperature for 20 minutes..... 80

Figure 34. Surface concentration of 5ML Pd/5ML Au/Mo(110) and 5ML Au/5ML Pd/Mo(110) measured by LEISS as a function of annealing time at 800 K.. 82

Figure 35. Surface concentration of various Pd-Au alloys on Mo(110) measured by LEISS compared to the corresponding bulk concentration. The sample was annealed at 800 K for 20 minutes. 84

Figure 36. IRAS spectra for CO adsorption on 10ML Pd/Mo(110) surface as a function of temperature. 87

Figure 37. IRAS spectra for CO adsorption on 10ML Au/Mo(110) surface at the indicated exposures and temperatures. 90

Figure 38. Coverage (a) and temperature (b) dependent IRAS spectra for CO adsorption on 5ML Pd/5ML Au/Mo(110) system. The alloy film was annealed at 600 K for 30 minutes..... 92

Page

Figure 39. Coverage (a) and temperature (b) dependent IRAS spectra for CO adsorption on 5ML Pd/5ML Au/Mo(110) system. The alloy film was annealed at 800 K for 45 minutes.. 94

Figure 40. TPD of CO on 5ML Pd/5ML Au/Mo(110) annealed at 800 K for 20 minutes (0.01 ~ 0.5 L of CO).. 96

Figure 41. Comparison of IRAS spectra for CO adsorption on 10ML Pd film, 5ML Pd/5ML Au alloy film and 10ML Au film on Mo(110) at saturation CO coverage. The alloy film was annealed at 800 K for 45 minutes, and the spectra were acquired at 80 K. 99

Figure 42. IRAS spectra for CO adsorption on 10 ML Pd film and 5ML Pd/5ML Au alloy film on Mo(110). The top and middle spectra were collected in 5×10^{-8} Torr CO background at the indicated temperatures. The bottom spectrum corresponds to the saturation CO coverage at 80 K. The right hand schematics represent the side-views of CO adsorption models on the respective surfaces. 103

Figure 43. IRAS spectra for saturation CO on (a) 7.5ML Pd/2.5ML Au/Mo(110) and (b) 2.5ML Au/7.5ML Pd/Mo(110) alloy films as a function of the sample annealing temperature. The sample was annealed for 20 minutes at each temperature, and the spectra were acquired at 80 K..... 105

Figure 44. (A) CO-IRAS spectra for alloy films with different Pd to Au ratios. All the alloy films were annealed at 800K for 30 minutes, and the spectra were acquired at 80 K with saturation CO coverage. (B) The peak area for the isolated Pd feature as a function of the surface Pd concentration obtained from Ref. 103. Point (e) corresponds to the peak area of the CO Pd atop feature on 10 ML Pd film.. 108

Figure 45 AES spectra for clean Mo(110), partially, and fully oxidized SiO_2 surfaces..... 113

Figure 46. LEIS spectra of (a) 1.0ML Pd/SiO_2 after a 800 K anneal; (b) after deposition of 1.0 ML Au deposition 300 K on 800 K pre-annealed 1.0ML Pd/SiO_2; and (c) 1.0ML Au/1.0ML Pd/SiO_2 annealed to 800 K. All spectra were collected at 300 K.. 114

Figure 47. LEIS data for 1.0ML Au/1.0ML Pd/SiO_2 after 800 K annealing (solid line) and 5.0ML Au/5.0ML Pd/Mo(110) after 800 K annealing (dashed line). All spectra were collected at 300 K.. 116

Page

Figure 48. TPD spectra of CO: (a) with 1.0 L CO exposure at 90 K on bare SiO_2; (b) 1.0ML Pd/SiO_2; (c) 1.0ML Au/SiO_2 ; (d) 1.0ML Pd/1.0ML Au/SiO_2; and (e) 1.0ML Au/1.0ML Pd/SiO_2.. 118

Figure 49. Surface concentration of Pd as a function of Au/Pd atomic ratio for various Au coverage (0.1-1.0 ML) on 1.0ML Pd/SiO_2 after 800 K annealing (■); for Au–Pd/Mo(110) after 800 K annealing (●). 120

Figure 50. CO TPD with 1.0 L CO exposure at 90 K of different Au coverage (0.1-1.0 ML) on 1.0 ML Pd/SiO_2. 122

Figure 51. IRAS spectra of CO adsorption on 1.0ML Au/SiO_2/Mo(110) as a function of temperature.. 124

Figure 52. IRAS spectra of CO adsorption on 1.0ML Pd/SiO_2/Mo(110) as a function of temperature. 125

Figure 53. IRAS spectra of CO adsorption on 1.0ML Au/1.0ML Pd/SiO_2/Mo(110) as a function of temperature. 127

Figure 54. IRAS spectra of CO adsorption on 1.0ML Au/3.0ML Pd/SiO_2 / Mo(110) as a function of temperature. 129

Figure 55. IRAS spectra of CO adsorption on 1.0ML Au/5.0ML Pd/SiO_2/ Mo(110) as a function of temperature. 130

Figure 56. IRAS spectra of CO adsorption on 1.0ML Pd/1.0ML Au/SiO_2/ Mo(110) as a function of temperature. 132

Figure 57. IRAS spectra of CO adsorption on 3.0ML Pd/1.0ML Au/SiO_2/ Mo(110) as a function of temperature. 133

Figure 58. IRAS spectra of CO adsorption on 5.0ML Pd/1.0 MLAu/SiO_2/ Mo(110) as a function of temperature.. 134

Figure 59. Ne^+ scattering LEIS spectra for 1ML Sn/4ML Pd/Rh(100) system as a function of annealing temperature.. 139

Figure 60. Surface concentration of Sn and Pd for 1ML Sn/4ML Pd/Rh(100) as a function of annealing temperature... 140

Page

Figure 61. Top: LEED pictures for (a) the clean Rh(100) substrate, (1×1); (b) the 4ML Pd/Rh(100) surface, (1×1); and (c) the 1ML Sn/ 4ML Pd/Rh(100) surface, c(2×2). Both the Pd film and the Pd–Sn alloy film were annealed at 700 K for 1 min before checking the LEED. The photos were taken at 300 K, and the incident electron beam energies were shown along with the pictures. Bottom: Ball-structure representations of pure Pd and ordered alloy films.. 142

Figure 62. Surface concentration of Sn and Pd for different amount of Sn deposited on 4ML Pd/Rh(100) surface. Each alloy surface was annealed at 700 K for 1 min before performing LEISS experiment.. 144

Figure 63. XPS Sn 3d core level spectra of 1ML Sn/4ML Pd/Rh(100) as a function of annealing temperature. 145

Figure 64. XPS Pd 3d core level spectra of 1ML Sn/4ML Pd/Rh(100) as a function of annealing temperature.. 146

Figure 65. IRAS spectra for CO adsorption on 4ML Pd/Rh(100) surface as a function of sample temperature..... 148

Figure 66. IRAS spectra for CO adsorption on 1ML Sn/4ML Pd/Rh(100) surface as a function of sample temperature. The alloy surface was annealed at 700 K for 1 minute. 149

Figure 67. Comparison of IRAS spectra for CO adsorption on 4ML Pd film, 1ML Sn/4ML Pd alloy film and 4ML Sn film on Rh(100) at saturation CO coverage. The alloy film was annealed at 700 K for 1 minute, and the spectra were acquired at 80 K. 151

Figure 68. Comparison of CO-TPD spectra for clean Rh(100), 4ML Pd film, 1ML Sn/4ML Pd alloy film, and 4ML Sn film on Rh(100). The alloy film was annealed at 700 K for 1 minute, and all the spectra represent saturation coverage..... 153

Figure 69. TPD of benzene from acetylene adsorbed on 10ML Pd/Mo(110) film and Pd–Au/Mo(110) alloy films with different compositions. Acetylene was exposed at 80 K, and 10 L was used in order to obtain saturation results. Each alloy surface was annealed at 800 K for 20 minutes prior to acetylene dosage. 157

Page

Figure 70. TPD of benzene from acetylene adsorbed on clean Rh(100), 4ML Pd/Rh(100) film, and Pd–Sn/Rh(100) alloy films with different compositions. Acetylene was exposed at 80 K, and 10 L was used in order to obtain saturation results. Each alloy surface was annealed at 700 K for 1 min prior to acetylene dosage.. 158

Figure 71. Comparison of benzene TPD spectra from acetylene adsorbed on 10ML Pd/Mo(110) film, 4ML Pd/Rh(100) film, 1ML Sn/ 4ML Pd/Rh(100), and 1ML Au/9ML Pd/Mo(110) alloy films. Acetylene was exposed at 80 K, and 10 L was used in order to obtain saturation results.. 160

INTRODUCTION

A chemical substance that can facilitate certain chemical reactions, without itself being consumed at the end, is called a catalyst. Catalysts are paramount to our daily life, since most biological reactions and the majority of chemical processes in nature are catalytic. It is estimated that 20–30 % of the gross national product in developed countries is dependent one way or another on catalysts. Most catalytic processes are heterogeneous in nature, typically involving solid catalysts and gas or liquid phase reactants. Catalyst surfaces are engaged in these processes by first adsorbing the reactants and then encouraging them to react until desorbing the products. Despite the importance, many aspects of heterogeneous catalysis on solid catalysts surfaces are not well understood.[1]

To illustrate a variety of topics in heterogeneous catalysis, two historically well–known reactions are selected. The Fischer–Tropsch process converts synthesis gas (H_2 + CO) into more useful chemical intermediate and fuels (methanol or liquid fuels or other hydrocarbons and oxygenates). Interest in this reaction has been renewed in recent years because of the shortage of crude oil and the emergence of new sources of synthesis gas such as biomass. In this process, selectivity is a major concern because numerous products are possible but only some are wanted for the particular applications. The catalytic conversion of noxious automobile exhaust gases (CO, NO_x and some

---

This dissertation follows the style of the *Journal of Physical Chemistry B.*

hydrocarbons) to more benign chemicals (CO_2, N_2 and H_2O) is another example. This reaction has become more and more important nowadays because of the need to reduce automotive pollution. Precious metals, such as platinum, rhodium and palladium, are used as catalysts for this process. However, a trivial amount of sulfur and lead contained in the gasoline normally poison these catalysts dramatically. Hence, finding a way to prepare more robust catalysts while using less expensive metal appears to be the most intensively studied topic in this area.[2]

Industry-used heterogeneous catalysts possess very complex structures, typically containing metal particles deposited on high surface area oxide supports and certain promoters. Normally, the design of these catalysts requires exhaustive trial and error tests. Only the results from those trials that provide both high catalytic activities and selectivities can be used for the development of some empirical intuition. A direct correlation between the desired catalytic performances with certain catalysts structural or electronic properties is difficult to obtain. This is mainly due to the lack of appropriate surface spectroscopic methods to scrutinize the catalyst morphology, composition, and physicochemical properties.

Surface Science Studies on Model Catalysts Systems

With the advent in the last forty years of a growing arsenal of ultra high vacuum (UHV) surface science techniques, a molecular level examination of the crucial phenomena that take place on the surface of a working catalyst has been made possible. The employment of metal single crystals as the simplest model catalyst systems has

further improved the experimental accuracy and reproducibility of surface characterization. Detailed studies of surface morphology, structure, and particular surface–adsorbate bonding sites yield useful information regarding all the aforementioned practical problems. In addition, all these analyses can be carried out before, after, and sometimes even during a low pressure surface catalytic reaction. The kinetics of such a reaction can also be monitored. Therefore, important reaction intermediates, active surface reaction sites, and special surface structural/morphological properties can be identified and further correlated to the catalytic performances.

Although this approach clearly offers many new opportunities for the study of heterogeneous catalysis, there have been doubts expressed concerning its validity. Industrial catalytic reactions are typically carried out at atmospheric (or higher) pressures and with far more complex surfaces then single crystal surfaces. The discrepancies between these two areas have been referred to as 'the pressure and material gaps'. The 'pressure gap' has been addressed in recent years through implications of a combined UHV–high pressure apparatus, which allow a sample to be transferred between a UHV chamber and a high pressure reactor cell via a series of differentially pumped sliding seals. The kinetics of certain catalytic reactions can be measured for a given surface in the elevated pressure reactor, while surface characterizations both before and after reactions can be accomplished in the UHV analysis chamber. This approach has allowed a direct comparison of kinetics measured on the single crystal model catalysts to that observed on real technical catalysts, and important issues like structure sensitivity can be addressed.[3,4] Additionally, newly

developed in-situ techniques such as polarization modulation infrared reflection absorption spectroscopy (PM-IRAS) have provided other means to bridge the pressure gap. These in-situ techniques are capable of microscopically scanning the realistic catalysts under working conditions, and monitoring the morphological modifications during a real catalytic reaction.[5,6]

Despite these successes in bridging the pressure gap, there is also a clear need to develop new model systems with higher levels of complexity to address important issues like metal–support interactions and special properties of multimetallic catalysts. The employments of bimetallic model catalysts and oxide thin film supported catalysts represent attempts to do so. The present investigation is devoted to this goal. The surface composition, morphology, electronic structure, and chemisorptive behavior of five model catalysts, *viz.* SiO_2/Mo(112), Ag/SiO_2/Mo(112), Au–Pd/Mo(110), Au–Pd/SiO_2/Mo(110), and Sn–Pd/Rh(100) are examined with a variety of surface science techniques. Important issues, such as identification of defect sites on the oxide surfaces and understanding of alloying effects (ligand and ensemble effects) in bimetallic catalysts systems, are addressed. In the succeeding sections, detailed rationales for these chosen systems are described.

Oxide Thin Film Methodology

Oxides are common materials with diverse properties ranging from conductors to semiconductors and insulators. This fascinating characteristic makes oxides useful in various fields besides heterogeneous catalysis. Compared with metal and semiconductor

surfaces, significantly less research work has been accomplished on oxides surfaces. One of the practical reasons is that many important oxides (such as MgO, Al_2O_3 and SiO_2) are very good electrical insulators. Many surface science techniques involve the emission or absorption of charged particles, whether electrons or ions, at some point in the measurement process. Studying these oxide surfaces then becomes difficult due to the surface charging. To overcome this problem, oxide thin films grown on refractory metal substrates are employed. This approach avoids the surface charge accumulation because the induced charge can be quickly dissipated to the metal substrate. Using an oxide thin film prepared under UHV conditions also allows the flexibility of controlling the oxide purity, composition, thickness, stoichiometry, and doping. More importantly, oxide thin films prepared in this manner have been shown to have similar chemical and physical properties with the corresponding bulk single crystals.[3,4,7]

Once these ultra thin oxide films are synthesized and characterized, the metal particles of catalytic interests can be vapor deposited onto these supports. This type of model catalysts serves as an ideal intermediate between single crystal model catalysts and 'real world' high surface area supported catalysts. It features many advantages of single crystals, such as well-defined in structure relative to powered catalysts and amenable to most surface science techniques. Many important issues, such as metal-support interactions and particle size effects, can be better studied thereafter. Moreover, by utilizing this type of model system, the size and structure of metal clusters can, in principle, be controlled. This is quite important for obtaining the possible structure-activity relationships. In addition, the oxide thin film surface is flat and conductive;

scanning tunneling microscopy (STM) and atomic force microscopy (AFM) can be used for imaging studies. Atomic resolution of Cu particles deposited on a SiO_2 thin film has been achieved by previous studies.[8]

SiO_2 has been chosen as a model oxide system in this study mainly due to its wide applications in both catalysis and microelectronics fields. The following studies were conducted on this model system: direct identification of surface defects, indirect observation of defects by studying the adsorption of probe molecules (Xe), and the investigation of metal deposition on oxide surfaces (Ag on SiO_2).

Defects on Oxide Surfaces

Coordinately unsaturated surface imperfections, such as steps, kinks, adatoms, and vacancies, are always present on oxide surfaces. The low coordination nature of these defect sites determines that the electronic structure and chemical behavior of oxide surfaces may be significantly influenced by these sites. As a result, defect sites are crucially involved in many important catalytic reactions on oxide surfaces. For instance, it was reported that water adsorption on a perfect MgO single crystal surface is predominately molecular in nature, while sputtering produces a highly defective surface upon which water is predominately dissociated.[9,10] Goodman *et al.* have found that color centers in the near-surface region promoted by $[Li^+O^-]$ centers are most probably responsible for the oxidative coupling of methane to ethane on Li-promoted MgO catalysts.[11] The electronic configuration of metal particles has also been shown to be

altered by oxide surface defects, which leads to an enhancement of catalytic reactivity in the reactions like CO oxidation in Au/MgO and Au/TiO_2 systems.[12-14]

Generally, defects on oxide surfaces can be classified as extended defects and point defects. Extended defects consist of steps, kinks, and grain boundaries, while isolated defects, such as vacancies, interstitials, and impurities, are point defects. Point defects, such as cation and anion vacancies, can trap holes or electrons to form V and F centers respectively. Normally, this will introduce additional energy levels within the band gap and cause selective absorption of some components of the visible light. The crystals are then colored, and hence the term 'color center' is also used to describe these types of defect centers. The predominant analytical techniques employed to study defects include optical methods such as ultra-violet spectroscopy and magnetic resonance methods such as electron paramagnetic resonance (EPR). However, all these techniques are aimed for bulk-property studies. Obtaining information about surface defects is quite difficult. Electron energy loss spectroscopy (EELS) and later high resolution EELS (HREELS) have been successfully used to identify various types of point defects within the first few atomic layers of the surface.[15,16] For example, the characteristic electron energy losses at 1.15, 3.58 and 5.33 eV upon thermal quenching or Li doping of MgO surfaces have been assigned to surface F–centers, F–aggregates. and F/F^+ centers, respectively.

In the present study, another technique, metastable impact electron spectroscopy (MIES) is used to specifically detect the surface defects. Due to its extreme surface sensitivity (this will be discussed in detail in the next section), the identification of

defects in the outmost oxide surface layer is possible, and the interactions of oxide surfaces with different adsorbates (both gas and metal probe molecules) as a function of defect type and density are also studied.

Bimetallic Model Catalysts

One of the most important discoveries in heterogeneous catalysis during the last several decades is the remarkable promotion of catalytic properties when adding a second metal component to a single metal catalyst, known as the alloying effect. Even for a binary alloy AB, with A being the metal with high catalytic activity and B being inert for the reaction considered, the reactivity and selectivity of alloy can be enhanced markedly from that of pure metal A. Many widespread commercial applications nowadays employ supported mixed metal systems as the catalysts, such as the catalytic reforming of saturated hydrocarbons to olefinic and aromatic ones (important in producing high performance gasoline) and the simultaneous oxidation of CO, unburned hydrocarbons with the reduction of NO (important for automobile emission control).[17] The prospect of using this phenomenon to make novel catalysts with improved properties has led to continuous interests in the surface science studies of multimetallic catalysts systems. The monometallic model catalyst systems have accordingly been extended to mixed metal model systems in order to address the special properties of multimetallic catalysts. The major objective of the present investigation is to enrich the fundamental understanding of surface morphology, composition, geometric structure, electronic, and chemical properties of bimetallic alloy catalysts. The establishment of

possible surface structure-reactivity relationships is expected to fulfill the long–term motivation of designing alloy catalysts at the atomic level.

In literature, a considerable amount of effort has already been directed to build different types of model bimetal catalysts. Single crystal or polycrystalline (prepared by melting high purity metals together) alloy surfaces were first utilized.[18-21] However, the difficulties in preparation and cleaning processes limited the application of these types of model systems. Later, systems prepared by physical vapor deposition of one metal on the single crystal of another metal substrate (such as Au on Pd(111) or Pd on Au(111)) have been extensively investigated.[22-26] But in this case, the metal surface compositions have been found to change significantly as the function of sample annealing temperature and time. Without the ability to form stable surface alloys, results based on this type of model systems are questionable. Another type of model system was introduced recently by deposition of both metal components onto a third metal substrate.[27-29] Experiments on this type of monolayer (ML) bimetallic films have been reported, but a major concern arises from the uncertainty of substrate influence. Therefore, a total 10 ML thick bimetallic alloy film supported on a third metal substrate is proposed as the first model alloy system in the present investigation. This guarantees the bimetallic film is thick enough to remove any potential substrate influence, while still providing merits of easy preparation and cleaning. Using Pd–Au bimetallic alloy film as an example, Mo(110) surface is chosen as the substrate. Because the bulk diffusion and intermixing ability of Pd and Au into Mo(110) is limited, a stable alloy film is expected to be formed after sequence annealing. Relatively small lattice misfits between substrate and adlayer alloys

should also be considered so that a flat pseudomorphic alloy overlayer with desired orientation can be obtained.[30,31]

Besides the planar bimetallic model systems (alloy films), oxide thin film supported bimetallic nano–particles (clusters) are also utilized in the present study. As discussed earlier, this type of supported model catalysts can better simulate the 'real world' high surface area catalysts. In particular, the Pd-Au bimetal nano-clusters are synthesized on an amorphous ultrathin SiO_2 film in this study, serving as an excellent oxide-supported bimetallic model catalyst.

In contrast to previous studies on model bimetallic systems where more focus was placed on the individual system, another goal of the current research is to identify possible trends existing among several related systems. Particularly, Pd related bimetallic alloy systems are emphasized in the present investigation because of their catalytic importance. The chemical properties of these bimetallic surfaces probed by CO adsorption behavior are one of the primary focuses in this study.

Ensemble and Ligand Effects

The alloying effect can in principle be ascribed into two causes:

The geometric ensemble effect: An adsorbate can bond with either one or several surface atoms on a pure reactive metal surface. Upon further reaction, adsorbates with different coordination will lead to different reaction products. Alloying with an inert metal can produce special ensembles with a smaller number of reactive metal atoms, which makes the formation of the desired chemisorption bonds more likely.

The electronic ligand effect: The chemical nature of inert neighbor metal atoms can substantially affect the chemisorption bonding between the reactive metal atom and an adsorbate. Catalytic selectivity is often determined by the relative chance of an absorbed intermediate either to react further or to be desorbed. It is obvious that weakening the adsorption bond by alloying can in principle change the activity and selectivity.

A good example for understanding the ensemble effect can be found in the literature by this STM, fourier transform infrared spectroscopy (FTIR), and voltammetric study on electrochemically prepared Pd-Au (111) alloy surfaces.[32] Their atomically resolved STM images of $Pd_{07}Au_{93}$ and $Pd_{15}Au_{85}$ alloy surfaces enabled access to the densities of various types of surface Pd ensembles, such as monomers, dimmers, and trimmers. It was then found that there is a clear correlation between the surface Pd monomer concentration and the surface CO coverage. Hence, the Pd monomers were identified as the surface critical ensembles for CO adsorption and oxidation. This is strong evidence that the special atomic arrangements, a single Pd atom surrounded by six Au atoms, are directly involved in determining the reactivity of bimetallic electrocatalysts.

The phenomenon of CO preferential adsorption on Pt–Co single crystal alloy surfaces provides a nice example for illustrating the ligand effects.[33] In this particular study from Varga *et al.*, STM was first used to image the Pt–Co alloy surfaces with chemical contrast. Then the positions of the adsorbates (CO) in the same surface image area were also determined. A comparison of these images indicated that CO molecules reside exclusively on top of Pt sites and never on Co. More interestingly, the probability to find CO on a Pt atom was found to increase drastically with the number of its Co

nearest neighbors. Their theoretical calculation showed that the shift of the Pt *d*-band center due to the neighboring Co atoms may be the reason for this observation. In this case, the CO bonding is quite sensitive to the chemical environment, and the difference in Co coordination numbers significantly influences the CO adsorption possibilities on Pt.

Even though these two mechanisms are commonly accepted and widely utilized to explain the enhancement of reactivity and selectivity for certain catalytic reactions, a stark differentiation between these two explanations is normally difficult because the arrangement of surface atoms usually affects the electronic structure of the surface and vice versa. The relative importance of ensemble and ligand effects has been examined by infrared spectroscopy for CO adsorption on a series of silica-supported, high surface area Pd–Au alloy catalysts.[34] In this study, the CO IR frequency for Pd atop sites was found red shifted from 2090 cm^{-1} to 2060 cm^{-1} after forming the alloy. This is considered as an indication of ligand effect since a red shift in CO IR frequency typically means an increase in the surface–CO bonding strength. Also, the CO IR intensity for the Pd bridge and three–fold hollow feature was found to decrease quickly with the increase of Au loadings. For the alloy sample with 40 % Pd, the broad bridge and hollow feature around 1900 cm^{-1} had already disappeared, while the atop Pd feature was still quite strong. An ensemble effect was inferred from this, indicating small Pd ensembles with relatively isolated Pd atoms are likely produced when the alloy forms. However, no further speculation about the exact ensemble size and formation was made, partially due

to the fact that the IR features from this high surface area samples were too broad and obscure.

Inspired by this early study, similar experiments on Pd–Au model bimetallic alloy catalysts have been performed using infrared reflection adsorption spectroscopy (IRAS) under UHV condition. Since CO adsorption on various low-index Pd and Au single crystal surfaces is well studied,[35-43] a comparison of the vibrational spectra between these systems enables us to address the potential of using IRAS to understand the fundamentals of ensemble and ligand effects. Despite the importance of ensemble and ligand effects in the application of bimetallic catalysts research, few techniques can actually be used to provide useful information about the primitive parameters for these effects. The superior sensitivity and resolution of IRAS offer us opportunities to examine ligand and ensemble effects quantitatively, which in the long term will definitely improve our capability of optimizing catalyst design.

EXPERIMENTAL

This section provides a description of all the experimental details for the studies performed in this dissertation.

UHV Surface Analysis Chambers

All of the experiments and sample preparations in this study were conducted in ultra high vacuum chambers. The primary reason for extreme low pressures is the sample cleanliness and function of electron and adsorption spectroscopies. Only under a UHV environment can a freshly cleaned surface be sustained long enough for spectroscopic probing. For all the techniques employing electrons, ions or molecular beams, UHV conditions assure the mean free path of these particles long enough to reach the detectors without interferences with other background gas molecules.

Three separated multi-technique UHV analysis chambers were utilized in this study. The electronic spectroscopy work was carried out in a chamber equipped with metastable impact electron spectroscopy (MIES). (This technique will be discussed in detail in the following section.) A schematic of this chamber is shown in Fig. 1. This chamber has a base pressure of 1×10^{-10} Torr, and consists of two interconnected compartments. The lower compartment is equipped with low energy electron diffraction (LEED), temperature programmed desorption (TPD), and an ion sputtering gun. In the upper level are facilities for Auger electron spectroscopy (AES), X-ray photoelectron spectroscopy (XPS), and metastable impact electron and ultraviolet photoelectron

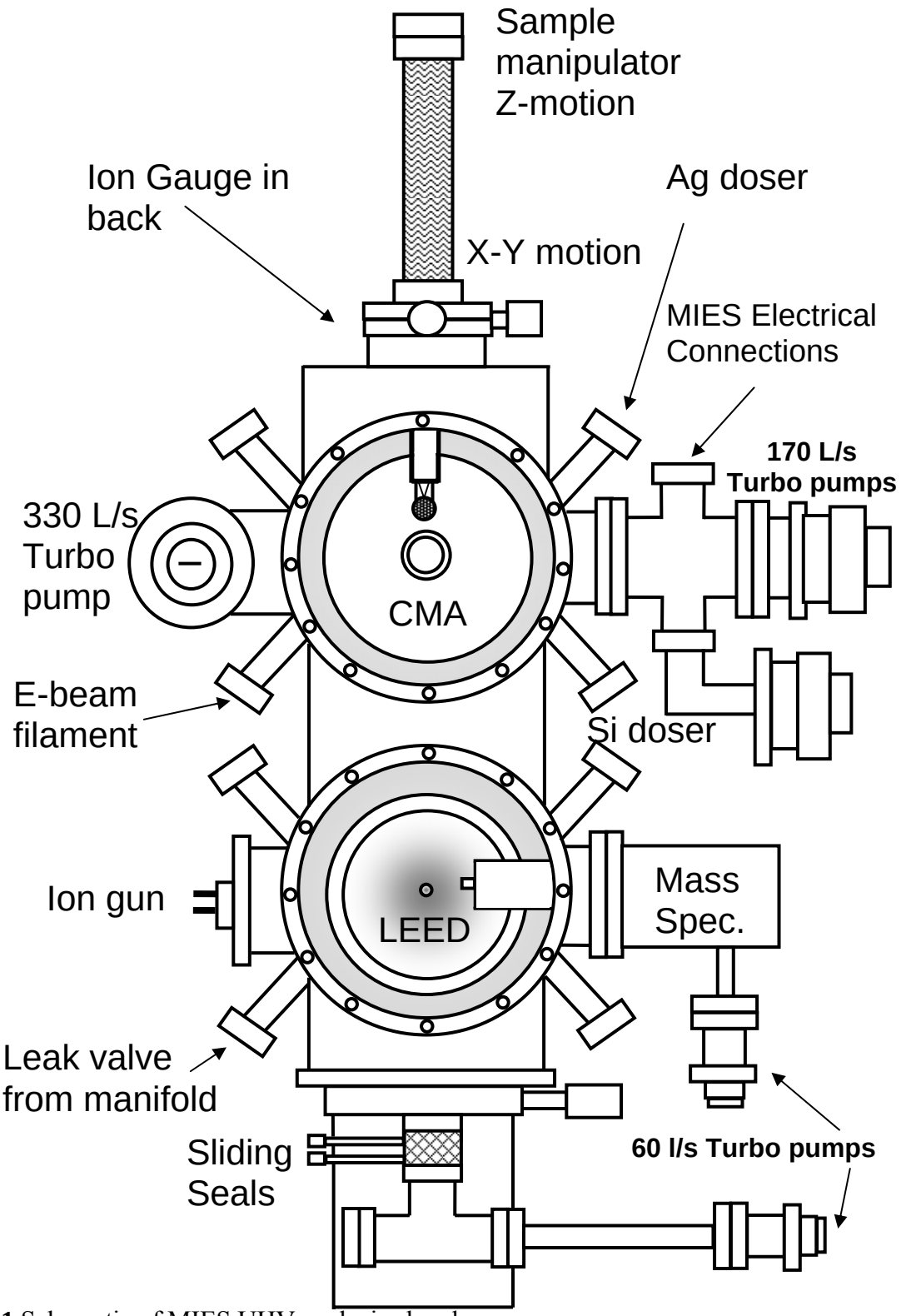

Fig. 1 Schematic of MIES UHV analysis chamber.

spectroscopies (MIES/UPS). MIES/UPS data are acquired simultaneously using a cold-cathode discharge source that provides ultraviolet photons and metastable He 2^3S (E* = 19.8 eV) atoms with thermal kinetic energy.[44,45] Signals from metastable and photon excitation are separated by a time–of-flight method using a mechanical chopper. MIES and UPS spectra are acquired using a double pass cylindrical mirror analyzer (CMA), and with incident photon/metastable beams at 45° with respect to the surface normal. The resolution of the analyzer, based on the width of the Fermi edge (E_F), is estimated to be 0.4 eV. The energy denoted by E_F in the spectra corresponds to electrons emitted from the Fermi level of the Mo substrate. In the following spectra, all binding energies are referenced to E_F.

The vibrational spectroscopic work was performed in an IRAS chamber. The schematic of this instrument is shown in Fig. 2. This chamber also has a base pressure of 1×10^{-10} Torr, and is equipped with a Perkin-Elmer Auger electron spectrometer (AES), a UTI quadrupole mass analyzer (TPD), and an infrared cell for IRAS measurements. The infrared cell is fitted with flange-mounted CaF_2 windows in the infrared beam path, and separated from the main chamber by a sliding seal (This will be discussed in details later.). While the sample is in the infrared cell, it can be pressurized independently of the main UHV chamber by this sliding seal design. Pressures in both the main chamber and the infrared cell are measured using a Granville-Phillips ionization gauge. IRAS spectra are collected using the Mattson Cygnus 100 spectrometer in single beam mode with external optics aligned for an incident angle 85˚ from sample normal. The detecting is via a liquid nitrogen-cooled mercury cadmium

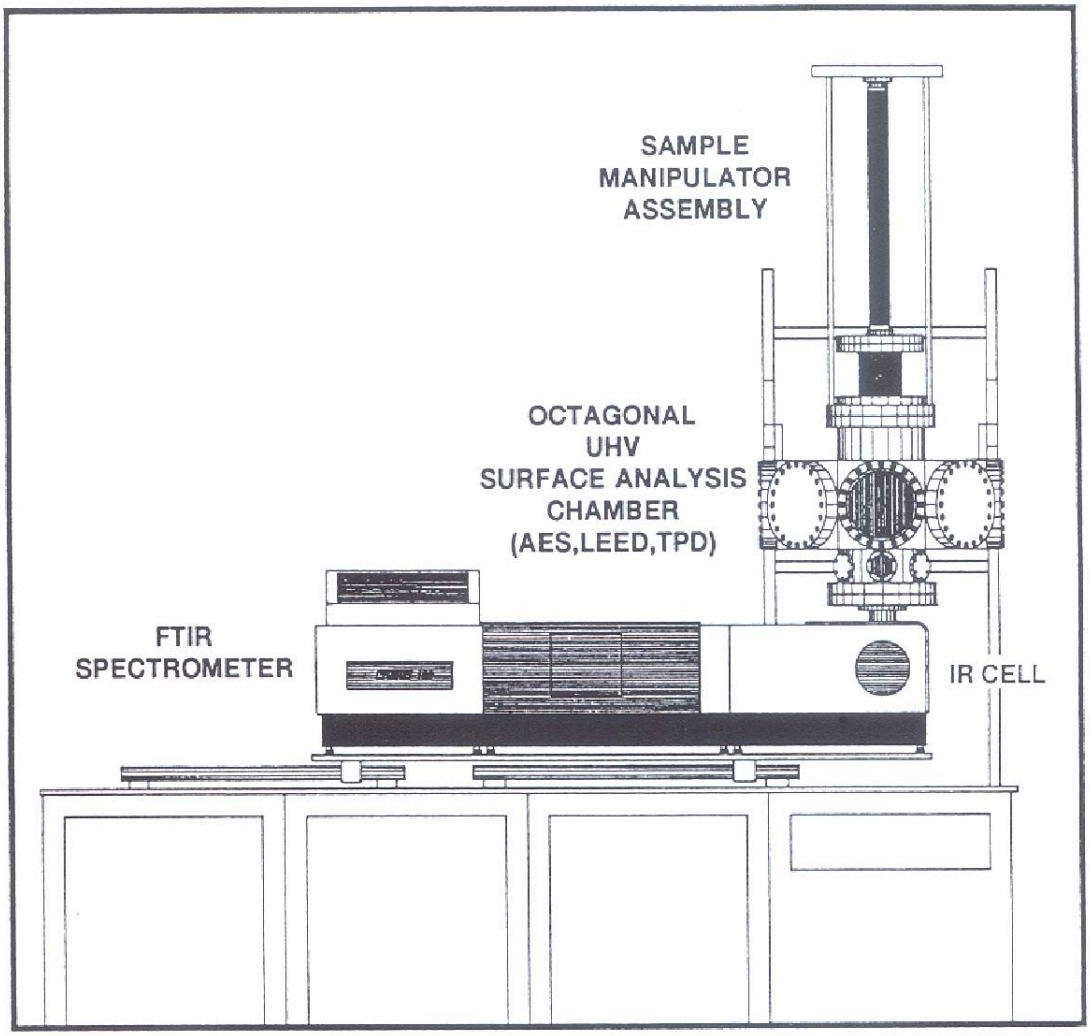

Fig. 2 Schematic of IRAS UHV analysis chamber.

telluride detector (MCT) and all spectra are averages of 512 scans at 4 cm^{-1} resolution. About 4.5 min is needed to take one spectrum. In TPD experiments, generally 5 K / s is used as the heating speed.

The last chamber is equipped with X–ray photoelectron spectroscopy (XPS), low energy ion scattering spectroscopy (LEISS), AES, LEED, and TPD. The schematic of the front view of this machine is displayed in Fig. 3. This chamber has a base pressure of 2 x 10^{-10} Torr. The XPS and LEISS spectra are collected using a concentric hemispherical analyzer (PHI, SCA 10-360). The Mg Kα XPS spectra are calibrated in most cases with the Mo $3d_{5/2}$ transition at 227.7 eV. LEISS is performed using He^+ ions at 1.09 keV and an ion beam scattering angle of ~ 55° with respect to the surface normal. The beam is rastered (5 mm × 5 mm) to minimize the ion beam damage. The rate of the sputtering depletion during LEISS is determined to be negligible for the relatively low beam energy employed.

There are some common designs shared by all these three instruments. For example, the sample is typically mounted on a sample probe at the top of the chamber. The sample probe is normally a stainless steel tube that has metal–ceramic feedthroughs at one end. There are four connections, two copper leads for sample heating and cooling, and two thermocouple connections. A type C thermocouple (W–5% Re/W–26% Re, provided by H. Cross Co.) is used to monitor the sample temperature because of its wide range of temperature measurement. Liquid nitrogen can be filled into the probe to cool the sample to around 80 K. Sample heating is possible using a DC power supply to run current through the sample to heat it resistively. The sample can be heated to around

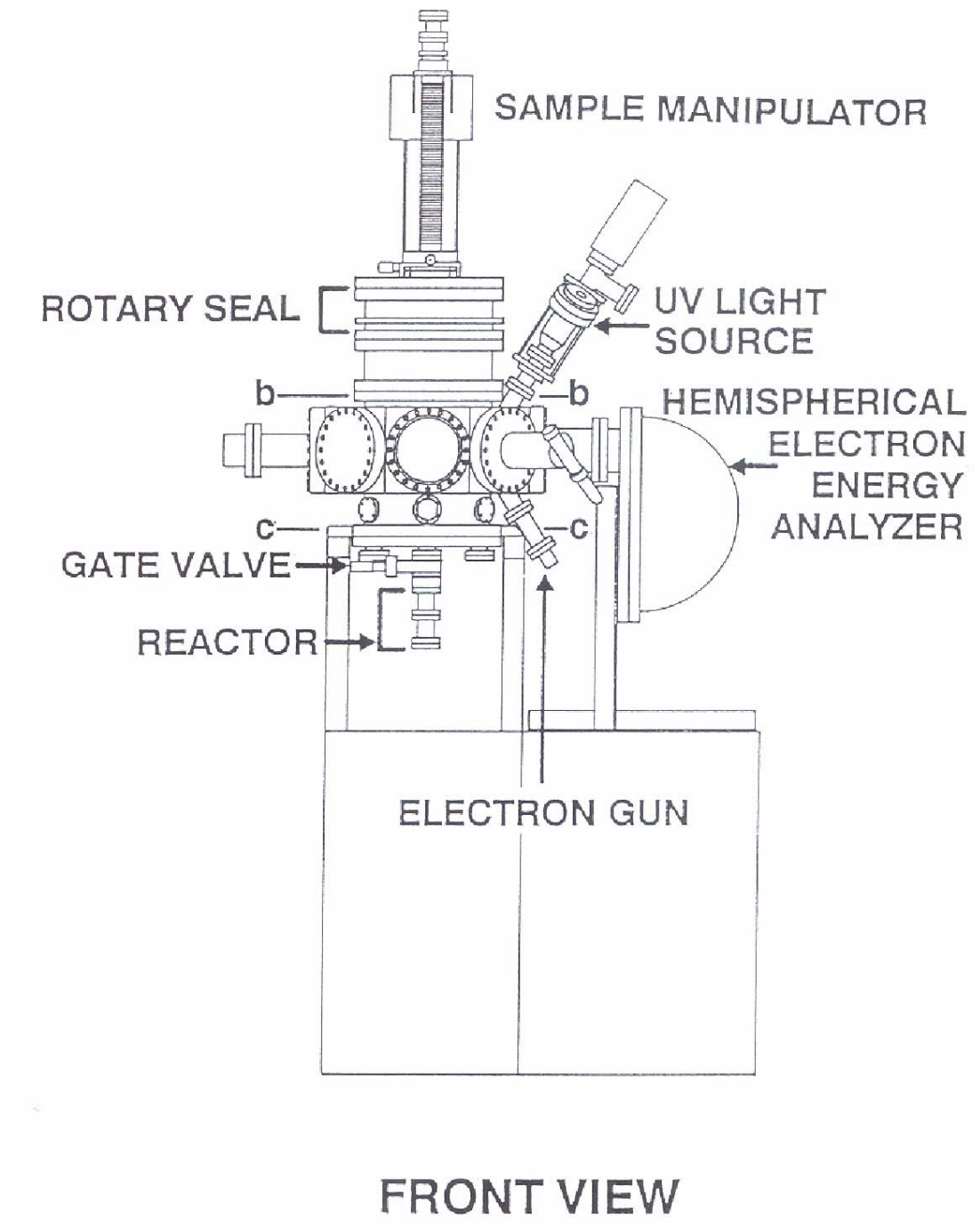

Fig. 3 Schematic of the front view of ISS analysis chamber**.**

1500 K by this way. If higher temperatures are needed, the electron bombardment heating can be performed. In this scheme, the sample is heated by a tungsten filament placed behind the sample. The sample will be bias positively (up to 600 volts) in order to better attract the electrons from W filament. It is possible to heat a metal sample (like molybdenum) to well over 2000 K by this method. The sample is mounted on a tantalum wire loop which is connected to the two copper leads. 0.030-inch wire (diameter) is usually used because of its better heat transfer ability.

The sliding seal design is also used in all these three machines. It consists of three Teflon seals and two pump-out ports in between these seals. The bottom port is pumped with a mechanical pump, while the upper one is pumped with a turbo-molecular pump. The inside diameters of Teflon seals are well designed to fit perfectly over the polished and chrome plated probe. Once the probe is inserted in the sliding seal, and the pumping lines are connected, it is possible to do high pressure exposures to the sample without interference of the UHV environment in the main chamber. In addition, the flange of the high pressure cell can be removed to provide access to the sample to either change it or make repairs to the mount without breaking vacuum. At the top of the bellows is a rotary seal which has the similar design as the sliding seal except only two Teflon seals and one pump out port are used. This differential pumping allows the probe to be rotated without losing vacuum inside the chamber. In all cases, the sample probe is attached to an upright linear motion table to provide movement in the Z–axis. An electrical motor is used to drive this table. Horizontal movements in the X and Y–axes

are controlled by a manipulator at the base of the bellows. Two micrometers are used to provide the movements in these two directions up to several centimeters.

Auger Electron Spectroscopy (AES)

AES is mainly used for the determination of the elemental composition of the sample surface, which is crucial for the identification of contaminates and calibration of metal dosers.[46,47] In AES, an incident electron causes photoemission of a core electron. This hole (or electron vacancy) in the core level may be filled by a second electron from higher level, while there is a simultaneous emission of a third electron (Auger electron). The kinetic energy of this Auger electron is determined by the difference in the energies of the first and second electrons. Hence, this energy is independent of the incident electron energy, but is solely characteristic of the binding energies of certain atom. This provides a fingerprint for every element. A cylindrical mirror analyzer (CMA, for example Phi model 15–255 G) is typically used to detect the Auger electrons. Incident electrons are provided by an electron gun inside of CMA, normally 2 or 3 kV energy and a 0.5 to 10 μ A current are used.

Photoelectron Spectroscopy

Photoelectron spectroscopy is widely utilized to probe the electronic structure of solid surfaces.[46,47] The basis of this technique is Einstein's photoelectric effect, whereby photons ($h\nu$) can induce electrons emission from a solid surface provided the photon energy is greater than the work function (Φ). (The work function of a solid surface is

defined as the minimum energy required to remove an electron from the highest occupied energy level in the solid to the 'vacuum level'.) An X-ray photoemission process is illustrated in Fig. 4.

In XPS, a monochromatic beam of X–ray is incident on a solid surface, ejecting electrons from both core and valence energy levels. Core levels are defined as the inner deep quantum shells, which do not participate in chemical bonding, while valence levels are more weakly bound, partially filled outer quantum shells. Because of the involvements in the chemical bonding, the outmost electrons are broadened into a 'valence band'. Emission from the valence band is more effectively probed by ultraviolet photoemission spectroscopy (UPS).

In XPS, the kinetic energy of a photo-emitted electron can be estimated as:

$$E_{kin} = h\nu - E_b - \Phi$$

Where E_b represents the binding energy of the particular core level. Due to the less influence of the chemical bonding, the binding energies of core levels typically are signatures of the atom type. The electron energy distribution (N (E) as a function of E_{kin}) measured by an electrostatic energy analyzer will provide information about the elemental composition of a sample surface. In addition, binding energy shift relative to the original level normally contains useful information, such as charge transfer, changes in oxidation states, and electron orbital redistributions.

Low energy ultra violet (UV) photons, which are generated from MIES source in our case, are used in UPS experiments. The photons are from the He I line at 21.22 eV. The reason that UV photons are used over X–ray is its better energy resolution and

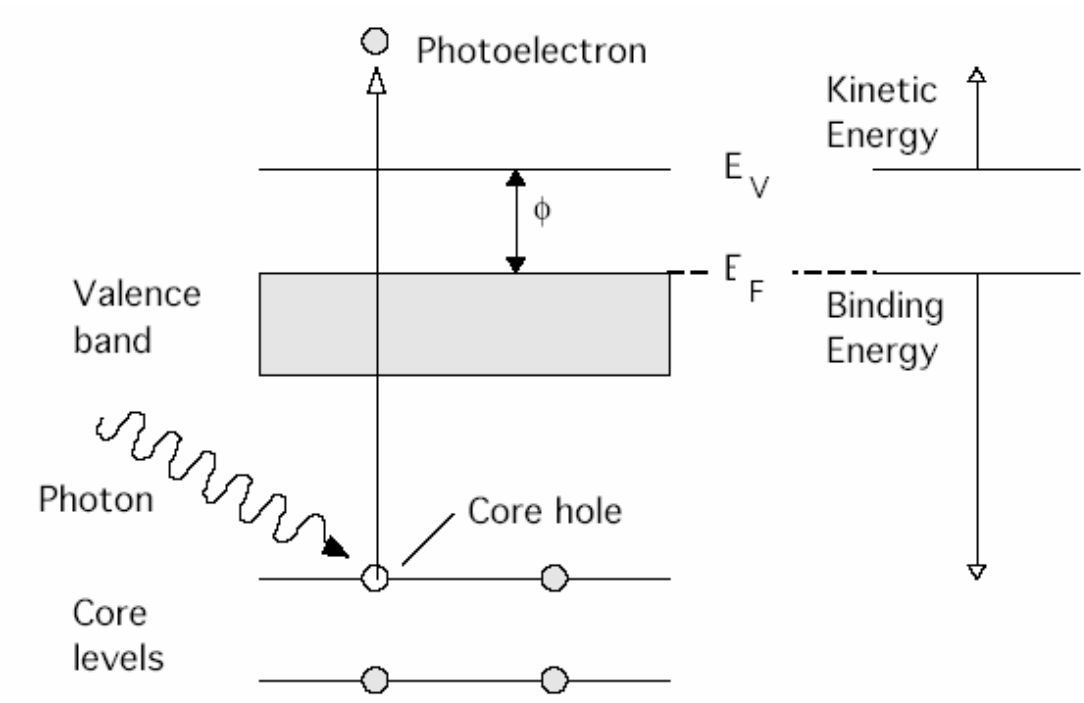

Fig. 4 Diagram of photoemission process.

surface sensitivity. UPS is also a more suitable technique to study the surface–adsorbate bonding conditions. It can provide information like which orbital has been substantially implicated in the bonding just by comparing the shift in the energy levels of adsorbates from the gas phase. The orientation of the adsorbate molecules can also be determined by observing the changes in the spectra while altering the incident light angles. In addition, UPS is commonly used for the measurement of work functions.

Metastable Impact Electron Spectroscopy

Unlike other electron spectroscopic methods, MIES has extreme surface sensitivity because the metastable helium (1s2s state) with only thermal kinetic energy is used for the surface probe. These relatively low energy atoms do not penetrate into the surface, but de-excite at the outermost atomic layer of the sample. There are two principle mechanisms in which they can relax, Auger Neutralization or Auger De-excitation.[48] Both mechanisms are pictured in Fig. 5. For metal and narrow band gap semiconductor surfaces, there are empty surface energy states in resonance with the Helium 2s energy level, so the Auger Neutralization process dominates. In this process, the first step is resonance ionization where an electron transfers from the 2s energy level of metastable helium to the empty energy state of the surface. The helium ion is then neutralized by the transfer of an electron from the valence band of surface to the helium 1s energy level with the simultaneous emission of a second electron from the valence band to the vacuum. Since two surface electrons are involved in this process, the spectrum is difficult to interpret. But for wide band gap materials, like oxides, there are no

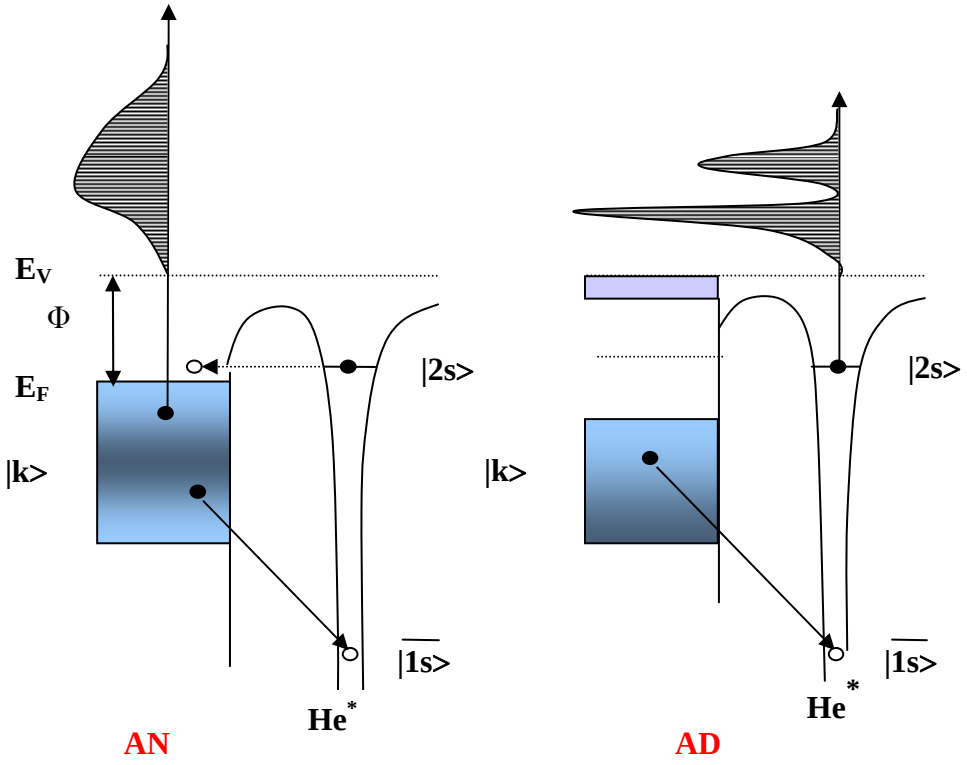

Fig. 5 The principle de-excitation mechanisms in MIES.

empty energy states available for resonance ionization, so only one electron from the valence band of the surface transfers to the Helium 1s energy level, and at the same time, the electron from the helium 2s state emits to the vacuum. This is referred to as the Auger De-excitation process. Since only one surface electron is involved in this process, the spectra should be able to map out the valence band electronic structure, comparable with UPS results. But in contrast to UPS, which relies on the finite escape depth of emitted electrons to provide surface sensitivity, the unique mechanism of MIES give us much more surface sensitivity.

Our MIES source is a custom made cold cathode discharge which provides both metastable He atoms and UV photons simultaneously. A schematic of the source is shown in Fig. 6. The source contains two differentially pumped chambers: a discharge chamber and a buffer chamber. The pressure for each part is also displayed in Fig. 6. A Mo cathode, 318 stainless steel anode, and He gas are used for discharge. In a stable discharge condition, the voltage of the discharge is lower than 250 volts and the current is around 60 mA. There is a mechanical chopper in the buffer chamber which is used to modulate the beam to separate signals from He metastable atoms and UV photons. This chopper usually operates at 2500 Hz. A capacitor up to 100 volts is utilized to remove any charged particles in the metastable/photon beam. The overall intensity of metastable He beam is around 5×10^{14} atoms/steradian.

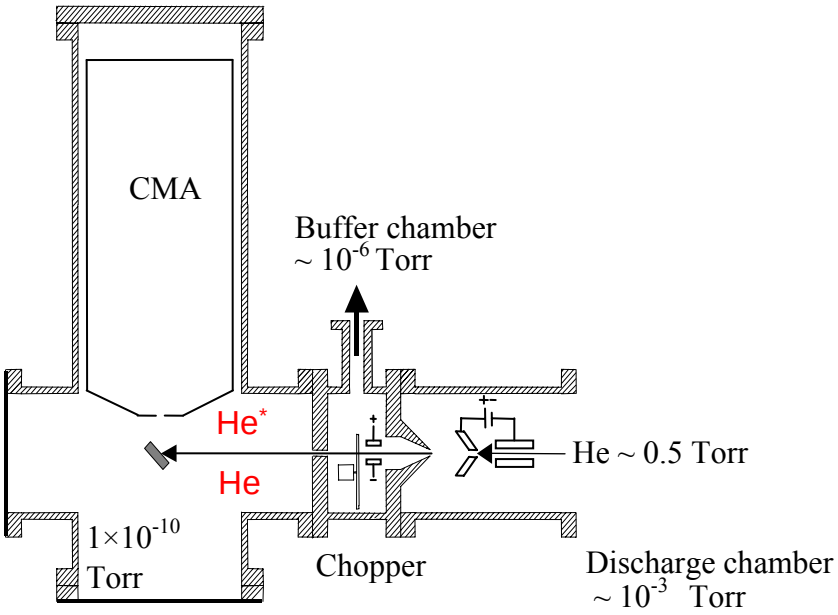

Fig. 6 Schematic of the home-built MIES/UPS source.

Low Energy Ion Scattering Spectroscopy (LEISS)

Low energy ion scattering spectroscopy (LEISS) is widely used for the determination of surface atomic composition. Typically in a LEISS experiment, a monoenergetic ion beam impinges on a target surface and the primary backscattered ions are detected at a defined direction. He^+, Ne^+, and Ar^+ are the most commonly used incident ions, and the beam energy used normally ranges from a few hundred to a few thousand electron volts (eV). At a fixed scattering angle, the energy losses of impinging ions are solely dependent on the masses of the surface atoms. Therefore, an energy spectrum with features corresponding to different energy losses will represent surface elements with specific masses.[49]

Because the cross section for the interaction of the ion and the suface atom is large, the atoms in the first surface layer will effectively screen the atoms in the second layer. Therefore, LEISS is an extreme surface-sensitive technique. Proper calibration has to be carried out in order to obtain the relative elemental sensitivities, which are crucial to the accurate quantitative analysis. Surface structural information can also be derived from LEISS studies, such as the growth mode of metal clusters. But in this case, scattering angle has to be changed systematically in order to get this type of information.

Low Energy Electron Diffraction (LEED)

Low energy electron diffraction (LEED) is a technique primarily used for determining the crystal surface structure. An illustration of LEED instrumentation is presented in Fig. 7. LEED uses low energy electrons (50 ~ 200 eV) to diffract off the

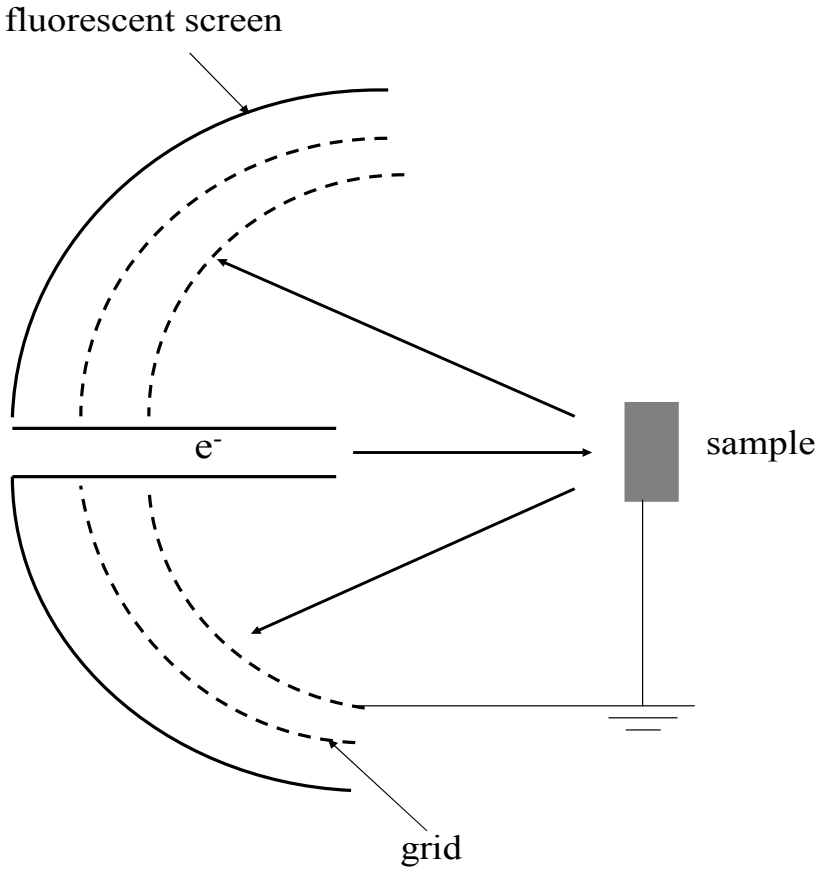

Fig. 7 Schematic of LEED optics.

crystal surface lattice and then project on a fluorescent screen. The design of a set of grids is used to allow only the elastically scattered electrons to reach the fluorescent screen. The elastic scattered electrons will form constructive/destructive interference patterns on the screen when scattered from an ordered surface. Due to the small mean free path (a few Å) of low energy electrons, LEED is a surface sensitive technique. Additionally, the structure of ordered adsorbate overlayers can also be studied by LEED.[47]

In this work, LEED was employed to check the cleanliness of the substrate and confirm the quality during oxide thin film growth. It was also used in Pd–Sn/Rh(100) bimetallic system to observe the structural changes as the function of the annealing temperature.

Temperature Programmed Desorption (TPD)

Temperature programmed desorption (TPD) is a simple yet powerful technique to study surface-adsorbate bonding strength and desorption kinetics. In a typical TPD experiment, a temperature ramp is applied to the sample and the rate of desorption is followed by monitoring the amount of adsorbate desorbed into the gas phase as a function of temperature. The heating rate is normally controlled to be linear with time (5 K/s is chosen for the most experiments in this study). The heating is also restricted only to the sample, thus avoiding desorption from other surfaces such as the sample holder. In this study, a quadrupole mass spectrometer was used to detect the gas product, and it is positioned closely to the front side of sample (~ 1 mm) in direct line of sight.[46]

TPD spectra are usually collected as a family of curves with increasing initial surface coverage. By applying Redhead, leading edge, or other analysis methods, information about the activation energy for desorption, the strength of lateral adatom interactions, and the relative surface coverage of adsorbate can be yielded from these spectra. Specifically in this work, TPD was employed to study CO adsorption on different bimetallic surfaces. CO desorption temperature and its shift from these systems were used to identify the surface adsorption site changes and correlate to the corresponding IRAS results. Dosing coverage calibrations for Au and Pd on Mo(110) substrate were also performed using TPD.

Infrared Reflection Adsorption Spectroscopy (IRAS)

Infrared reflection absorption spectroscopy (IRAS) is a vibrational spectroscopic technique extensively used in surface science studies. The vibrational excitation of surface adsorbates is based upon the interaction of the electronic field of the incident infrared light with the dipole moment of the surface adsorbates. The generated spectral fingerprints can be used to identify surface adsorbed species. And particularly, the high sensitivity (< 5/l000 of a CO monolayer) and resolution (l-3 cm^{-1}) make this method suitable to study the interaction between metal substrate and adsorbed molecules as well as intermolecular interactions within an adsorbed layer of molecules.[37,46]

Many surfaces are opaque to infrared radiation, so transmission experiments are not viable. Most surface science IR studies thus use the so–called reflection mode. Fig. 8 illustrates a typical experimental set–up for a vacuum IRAS experiment. Infrared light

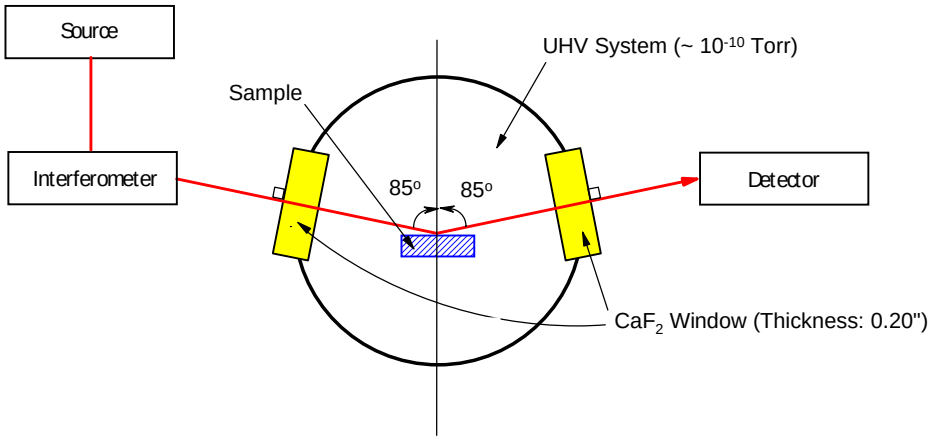

Fig. 8 Schematic diagram of the experimental configuration used in IRAS.

is focused through an IR–transparent window (CaF_2 in this case) on to the sample surface at grazing incidence. The sample acts as a mirror, reflects the beam out of a second vacuum–sealed window, where infrared radiation is refocused on to a photoconductive semiconductor detector such as mercury cadmium telluride (MCT) (detection range 5000–800 cm^{-1}). A purge gas generator is normally used to produce H_2O and CO_2 free compressed air. The IR beam path outside of the UHV chamber can be purged by this gas in order to minimize interference from gas phase absorption bands associated with H_2O and CO_2.

IRAS experiment is performed in a grazing incidence geometry mainly due to the need of maximizing surface sensitivity. This can be rationalized in several ways. First, in the reflection mode the IR beam will pass through the surface layer twice (before and after hitting the reflecting substrate). This leads to an increase in path length, hence improving the surface sensitivity. Second, the magnitude and the phase of the radiation also change drastically upon reflection as the angle of incidence approaches grazing. The exact mechanism by which these changes occur is complex. However, the net result is an enhancement in the electric field vector of the IR photon perpendicular to the surface for grazing incidence geometry, and zero magnitude for the component parallel to the surface. Therefore, only molecular vibration giving rise to a dynamic dipole moment perpendicular to the surface will yield IR absorption. This is called the surface selection rule. Another way of understanding the surface selection rule is to consider the induced 'image dipole moment' of the substrate to the molecular vibrations of an adsorbate (Fig. 9). As can be seen in Fig. 9 (b), the dipole moments of the image charge

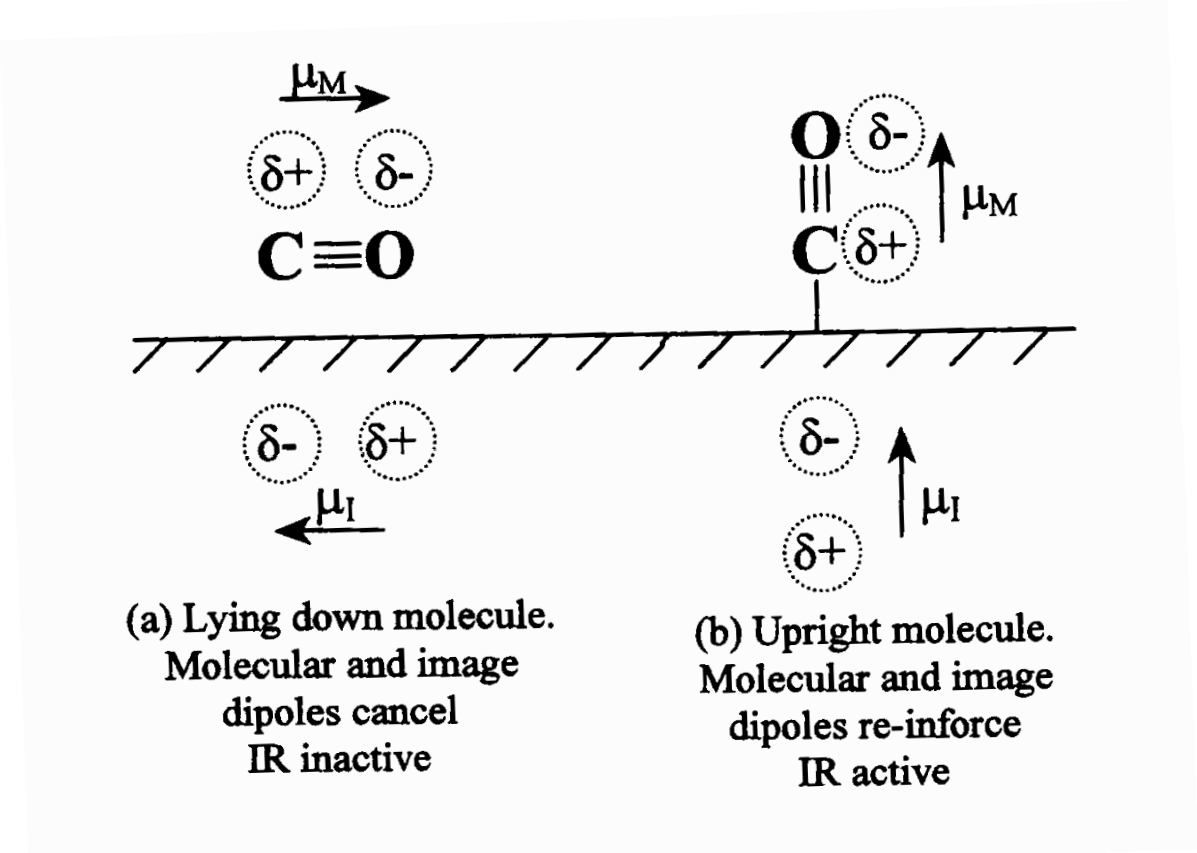

Fig. 9 Illustration of surface selection rule in IRAS experiments. (Adopted from Ref. [46])

and the surface CO molecule reinforce each other in the upright configuration. Hence, a significant IR absorption is obtained due to this surface–enhanced change. In contrast, for a molecular dipole aligned parallel to the surface, the image and surface molecular dipoles cancel each other and no IR absorption is observed.

The interaction between gas adsorbates and substrate typically leads to frequency shifts in the vibrational modes of adsorbates from the gas phase value. For example, the CO stretching frequency shifts to a lower number (red–shift) when CO is adsorbed on most metal surfaces (The gas phase value is 2143 cm^{-1}.). This shift is influenced primarily by three contributions: mechanical renormalization, the interaction with image dipole, and the chemical bond with surface. Mechanical renormalization, or so–called 'wall effect', arises because CO is attached to a rigid substrate. A shift to a higher frequency (blue–shift) approximately 50 cm^{-1} has been estimated due to this effect. The interaction of an adsorbed CO dipole with its own image in the metal surface normally causes a downward shift about 30–50 cm^{-1}. The bonding between adsorbed CO and metal surface is often described by Blyholder model (Fig. 10). This model assumes that the chemical bond between CO and metal is formed by charge transfer from the 5 σ -molecular orbital (MO) of CO into the metal substrate and by 'backdonation' from metal d-bands into the unoccupied 2 π *-MO of CO. Since the 5 σ -MO is only weakly bonding, but the 2 π * strongly antibonding, the C-O bond is weakened by the chemisorption bond and the amount of backdonation into the 2 π * is drastically reflected by a lowering of the C-O stretching frequency. Moreover, the vibrational frequency of CO varies significantly depending on the different bonding sites of the

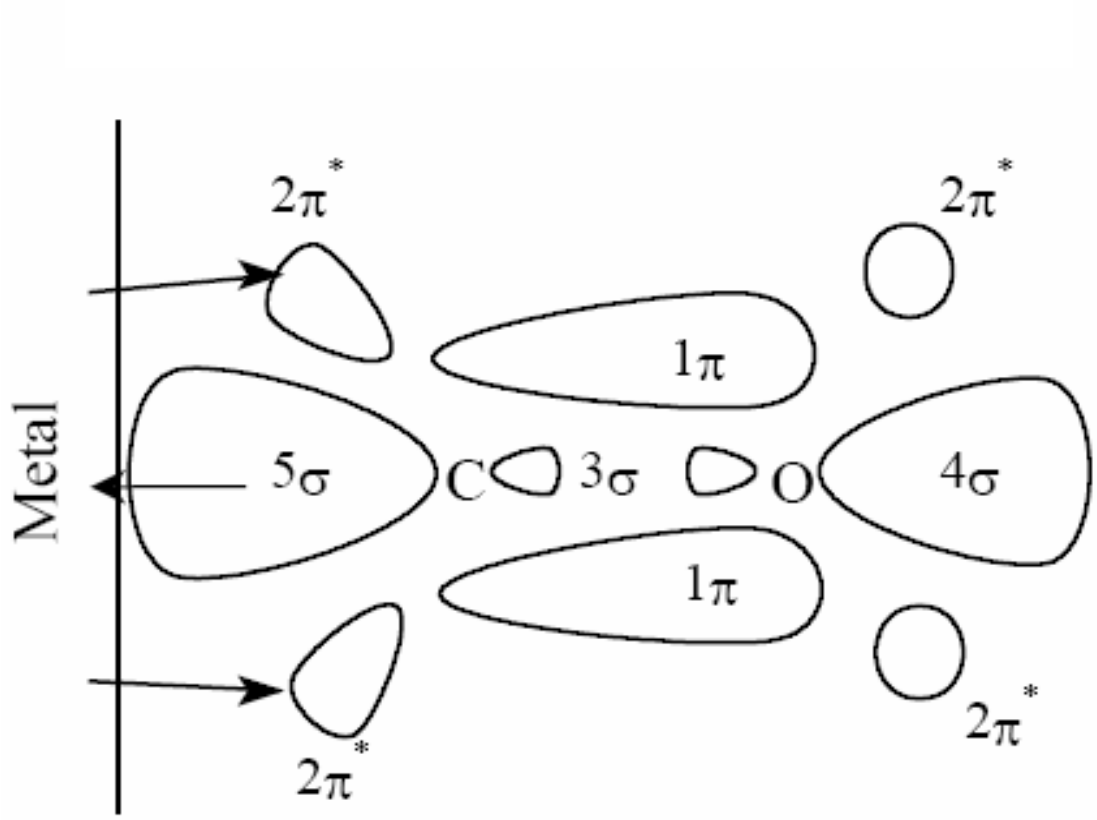

Fig. 10 Schematical representation of 2 π * backdonation for adsorbed CO.

metal surface: typically 2130–2000 cm^{-1} for a linear bound species, 2000–1860 cm^{-1} for a 2–fold bridging species, 1920–1800 cm^{-1} for a 3–fold bridging configuration, and 1800–1700 cm^{-1} for a 4–fold bridging CO.[37]

IRAS was primarily used in this work to identify the adsorption sites for CO onto bimetallic model catalysts

Sample and Doser Preparation

The Mo(112) and Mo(110) single crystal substrates were cleaned by oxidation (1200 K, 1×10^{-7} Torr O_2) and flash (e-beam heating to 2100 K) cycles until no carbon and oxygen can be observed in AES and sharp substrate LEED pattern can be observed. The clean Rh(100) substrate was prepared by repeated cycles of Ar^+ sputtering (5×10^{-5} Torr Ar, 2 kV, 30 mA) and surface annealing at 1200 K until a contaminant–free surface with a clear substrate (1×1) LEED pattern can be obtained.[50]

The Au, Ag, and Pd dosers were made by wrapping high purity metal wires around a tungsten wire. The Mg, Si, and Sn dosers were made with high purity metal wires inserted into a W wire-wrapped alumina tube. Impurities were removed by thoroughly degassing before dosing. All the metal depositions were performed with the sample at the room temperature. The dosing rates were calibrated by TPD, AES and LEISS.

Ultra-high purity O_2 (99.98%, Matheson Tri-gas) and CO (99.99%, Matheson Tri-gas) were introduced into the ultra high vacuum chamber using leak valves. Details of the SiO_2 films preparation have been described previously.[51] Surface characterization by AES showed that the SiO_2 films were fully oxidized. The thickness of the SiO_2 films

was measured using the attenuation of the AES Mo substrate signals and the known mean free paths of Auger electrons.

Due to the small difference in atomic mass between Sn and Pd, the two elements could not be readily discriminated by LEISS using He^+ probe. Hence, Ne^+ was used as the incident ion probe with a kinetic energy of 0.75 keV.

RESULTS AND DISCUSSION

Detailed experimental characterization of every model catalyst systems is presented in this chapter. For SiO_2/Mo(112) and Ag/SiO_2/Mo(112) systems, MIES and UPS were mainly used to study the electronic structures of these systems. For the rest bimetallic model catalyst systems, IRAS and TPD using CO as a probe molecule were the main techniques utilized for investigating the chemical properties of these alloy surfaces.

SiO_2/Mo(112)*

The recipe of preparing a well ordered SiO_2 thin film on a Mo(112) substrate was adopted from Freund group.[52,53] The Si was first deposited on the cleaned Mo(112) sample at room temperature and oxidized at 800K in 1×10^{-7} Torr oxygen background for 15 minutes. Subsequently, the film was annealed at 1200K for 5 minutes in 1×10^{-7} Torr oxygen. LEED for the SiO_2 films synthesized as above showed a c(2×2) periodicity, indicating the formation of a well ordered SiO_2 network (Fig. 11). For these SiO_2 thin films, Si^{4+} features were evident at 76 eV in the AES spectra with no Si^0 features at 92 eV, indicating that the Si is completely oxidized (Fig. 12). The thickness of the film was estimated to be 0.4-0.7 nm through AES Mo substrate peak (186 eV) attenuation.[54]

∗ Reproduced in part with permission from: Kim, Y. D.; Wei, T.; Goodman, D. W. *Langmuir*, **2003**, 19, 354; Kim, Y. D.; Stultz, J.; Wei, T.; Goodman, D. W. *Journal of Physical Chemistry B*, **2003**, 107, 592, Copyright 2005 American Chemical Society.

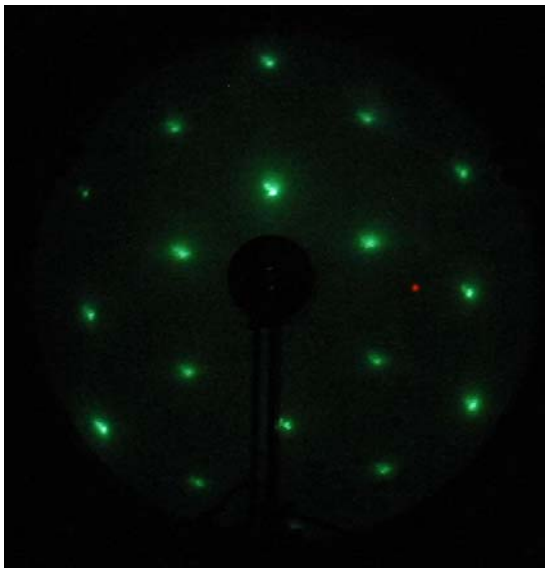

Fig. 11 LEED pattern for a well ordered SiO_2 thin film supported on Mo(112).

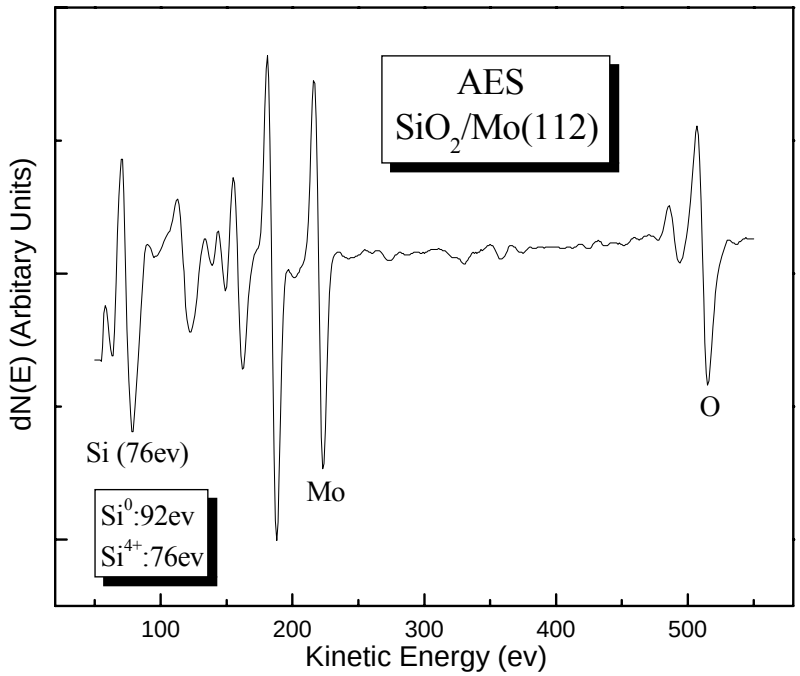

Fig. 12 AES spectrum for a SiO_2 thin film supported on Mo(112).

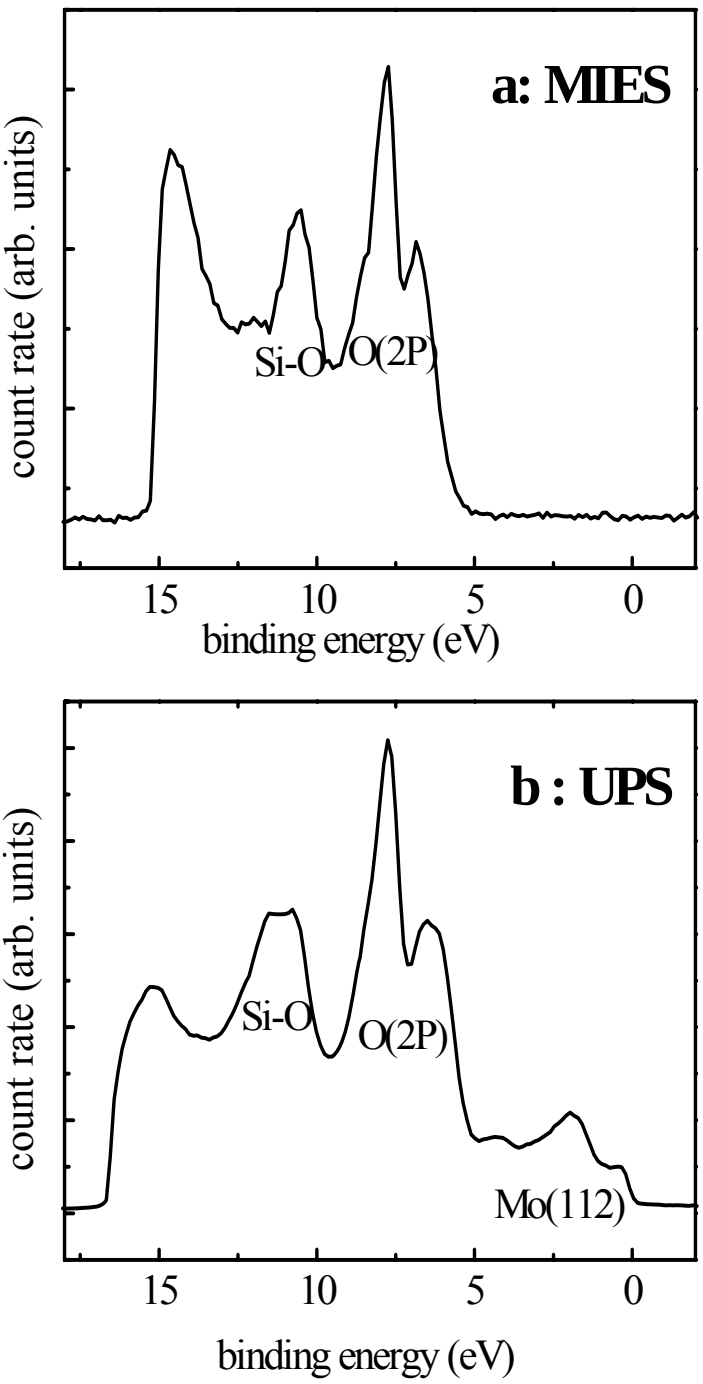

Fig. 13 MIES and UPS spectra for a low–defect SiO_2 thin film.

The MIES/UPS spectra for a low-defect SiO_2 thin film are shown in Fig. 13. The main features in the MIES spectrum are doublet peaks at 6–8 eV and another smaller peak at 11 eV, which correspond to the O(2p) nonbonding states and the Si–O bonding state respectively.[55] The UPS spectrum for this SiO_2 thin film is similar to the MIES spectrum, i.e., the O(2p) and the Si–O features are at similar energy positions. But there are slight differences in bonding energies because MIES is sensitive to the topmost surface layer, whereas UPS integrates over the surface and near-surface region. In the UPS data, additional features with lower intensities originating from the Mo(112) substrate are apparent between 0 and 4 eV in contrast to the MIES data.[54]

It is also noteworthy that the MIES/UPS spectra for these SiO_2 thin films are identical to previously published photoemission spectra for SiO_2 bulk crystals,[55] indicating that the electronic properties of the SiO_2 thin films with a thickness of 0.4-0.7 nm are essentially identical to those of bulk SiO_2. Recent scanning tunneling spectroscopy (STS) studies in combination with UPS and electron energy loss spectroscopy (EELS) show that bulk-like electronic properties of MgO thin films on Ag(100) develop within the first 2-3 monolayers (ca. 0.5–0.8 nm).[56]

Fig. 14 shows a magnified view for the low energy portion of the MIES spectrum of Fig. 13a, in which the onset of the first filled state of the valence band appears at 4.4 eV. Assuming that the Fermi level of Mo(112) is located at the midpoint between the conduction and valence bands of the SiO_2 films,[57] the measured band gap of the SiO_2 thin films is approximately 8.8 eV, in good agreement with the band gap found for bulk SiO_2.[58]

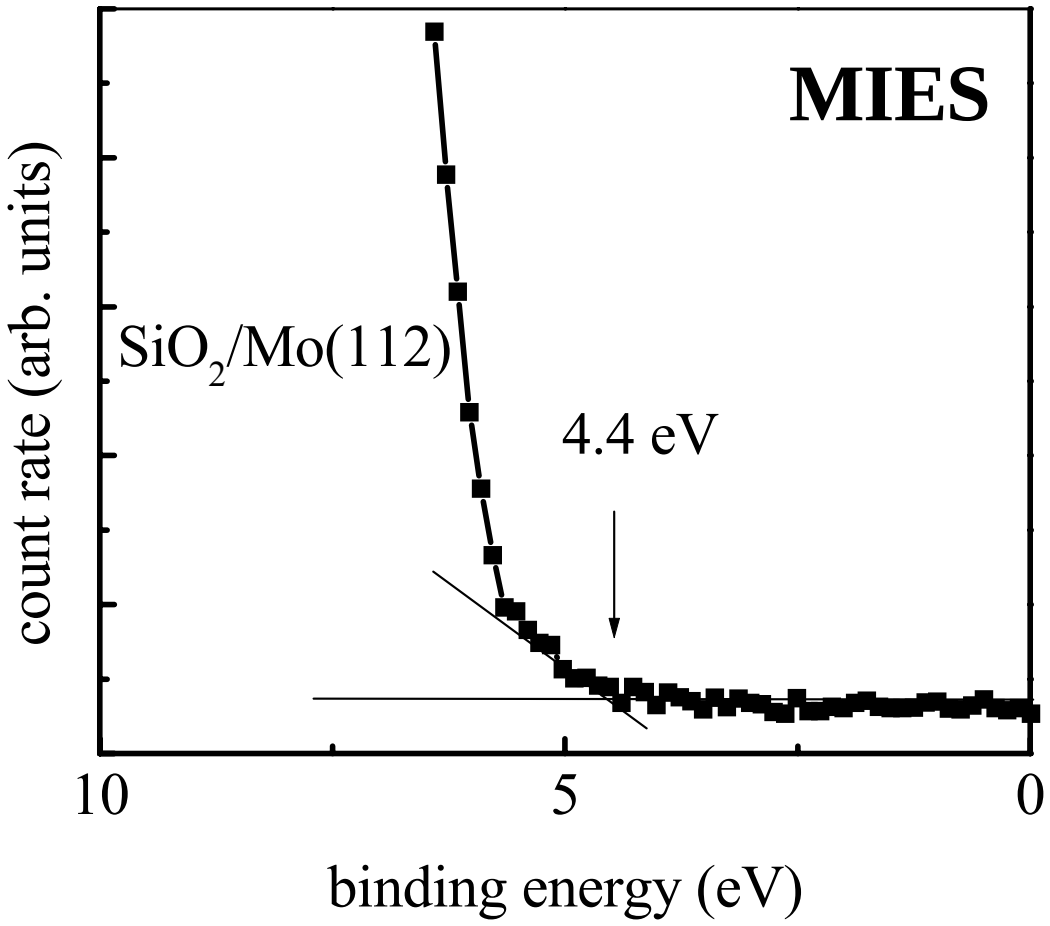

Fig. 14 A magnified view of the MIES spectrum in Fig. 13a.

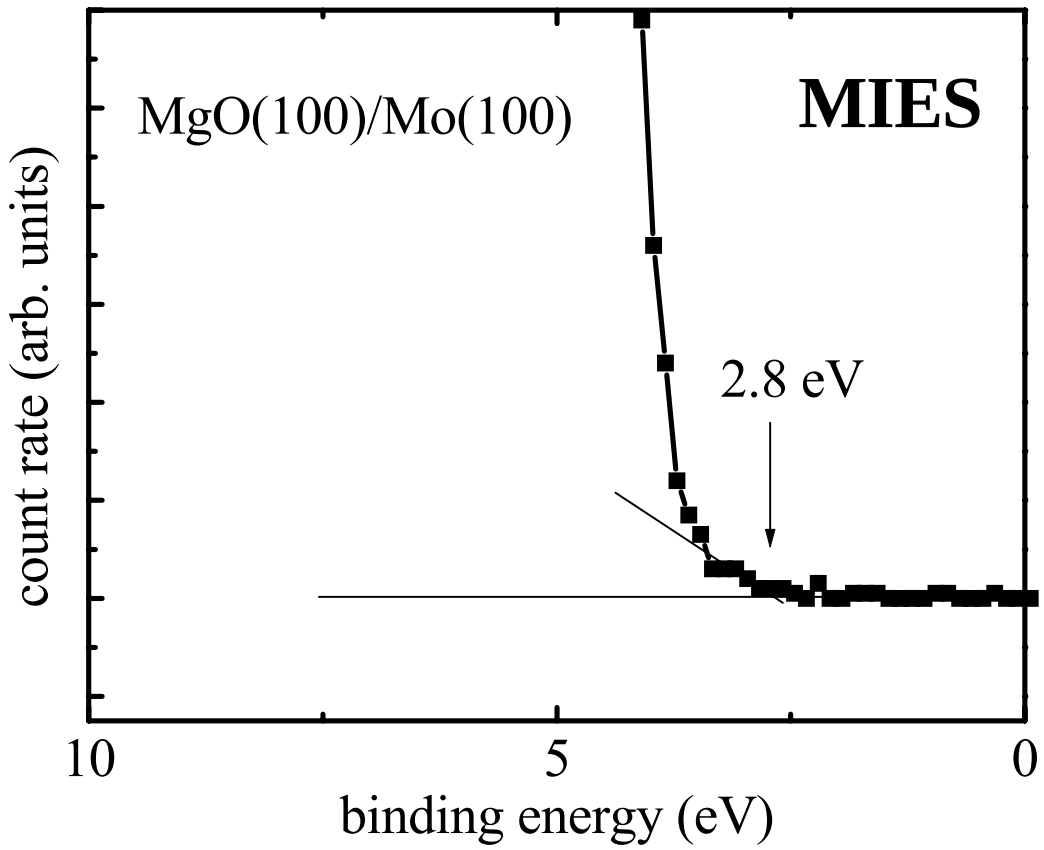

Fig. 15 An enlarged view of a MIES spectrum for a MgO thin film on Mo(100).

To check the reliability of the method used for determining the band gap of the SiO_2 thin films, the band gap of a low defect MgO thin film on Mo(100) was determined from its MIES spectrum. Previous studies have shown that the electronic and chemical properties of MgO thin films prepared by deposition of Mg in O_2 background at 600 K followed by annealing at 1150 K are identical to those of well-ordered MgO(100) single crystals.[59,60] The onset of the valence band of the well-ordered MgO thin film is at 2.8 eV (Fig. 15). With the same assumptions used for the determination of the SiO_2 thin film band gap, the band gap of the MgO thin film is estimated to be 5.8 eV, consistent with the value determined with electron energy loss (EELS) and optical spectroscopies.[16]

Direct Identification of Surface Defect Sites

The easiest way to study defects on an oxide surface is through direct observation. In order to have evidence of the defect, it must cause an observable change in the physical or electronic properties of the sample. When a defect is an occupied energy state, it can be directly seen with electron spectroscopic technique.

Previous optical spectroscopy measurements indicated various absorption and luminescence bands for defective SiO_2.[61-68] Theoretical studies, carried out to better understand the optical absorption and photoluminescence spectra of SiO_2,[58,67,69-74] have shown that additional occupied and unoccupied states are present in the band gap region when various defect sites (oxygen vacancies or excess oxygen) are present. These defect sites are responsible for the experimentally observed color centers.

Previous MIES studies have shown that small amounts of oxygen vacancies on MgO surfaces can be identified using MIES, whereas UPS is not as sensitive as MIES for assessing oxygen vacancies.[48,75] If defect sites on SiO_2 surfaces lead to additional occupied states in the band gap, MIES should identify these defect states.

An additional occupied state in the band gap, which is not present on low defect SiO_2 surfaces, is observed for a defective SiO_2 surface (Fig. 16a) prepared by depositing excess Si onto a well-ordered SiO_2 surface at room temperature followed by oxidation at 800 K. Following an anneal to 1050 K, the band gap state disappears (Fig. 16a) indicating that the anneal reduces the number of defect sites.

Given that the defective surface in Fig. 16 was created by oxygen treatment at 800 K, it is reasonable to assume that the number of oxygen vacancies on this surface is relatively low. Furthermore, no Si^0 was detected with AES, consistent with the number of oxygen vacancies being low. Therefore, it is likely that defect sites other than oxygen vacancies, such as a peroxyl bridge, a peroxyl radical, or a nonbridging oxygen,[58] are responsible for the appearance of the band gap states in Fig. 16a.

In contrast to MIES, no additional electronic state induced by defect sites can be clearly identified by UPS (Fig. 16b). The UPS spectra consist of contributions from the SiO_2 film as well as features from the underlying Mo(112) substrate that overlap the band gap states from various defect sites of SiO_2. This superposition of the Mo(112) features and the defect states complicate the unambiguous identification of defect states in the band gap using UPS.

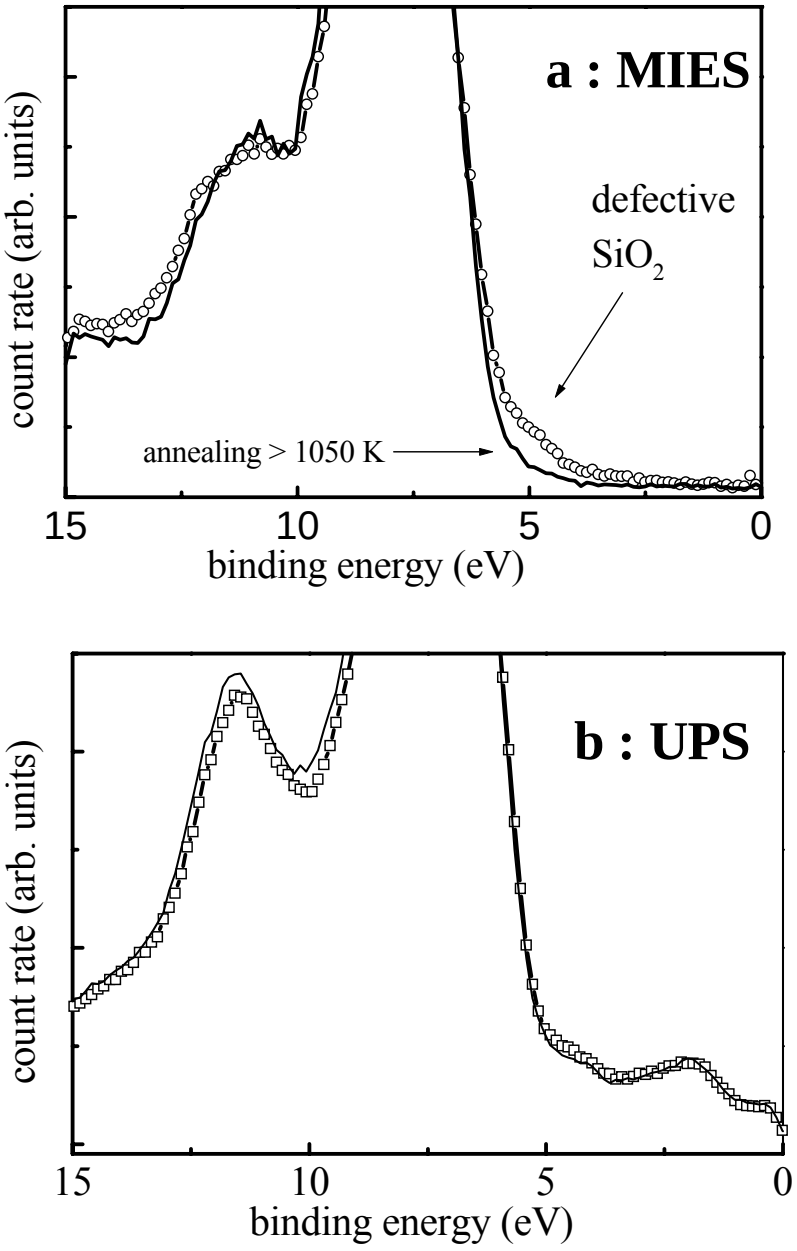

Fig. 16 MIES and UPS spectra for a defective SiO_2 film before and after annealing at 1050 K. The defective film was prepared by deposition of Si onto a well-ordered SiO_2 film at room temperature, followed by oxidation at 800 K. Further annealing at 1050 K results in the disappearance of the defect state.

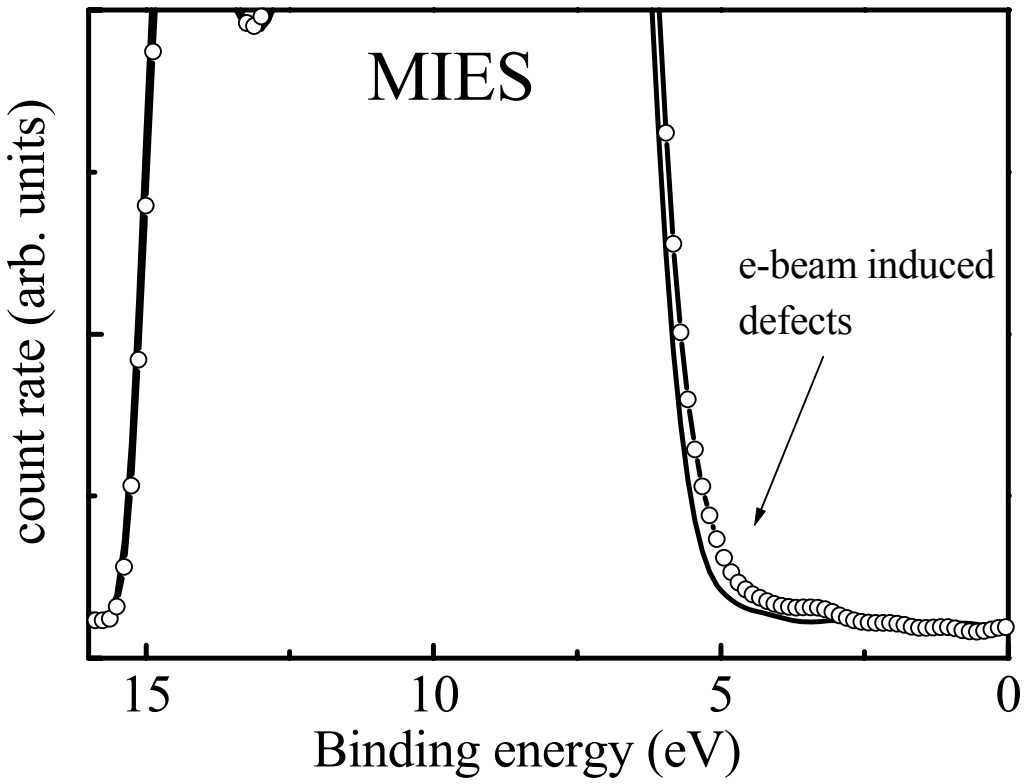

Fig. 17 MIES spectra for a SiO_2 thin film before and after e-beam bombardments.

Additional band gap states were observed on a SiO_2 thin film damaged by 3 kV– electron beam (Fig. 17). On MgO surfaces, high energy electron beam treatments selectively remove oxygen atoms from the surface, creating F/F^+ centers.[75] Likewise, electron bombardments induce the formation of oxygen vacancies on SiO_2 thin films, which can form additional states in the band gap. Band gap states are also introduced in the SiO_2 films by deposition of Si at room temperature. As is apparent in Fig. 18, Si deposition onto SiO_2 at room temperature introduces features in the MIES spectrum similar to those found for the defective SiO_2 surfaces of Fig.16 and 17. Si deposition onto SiO_2 can create an oxygen-depleted SiO_2 surface with an electronic structure essentially identical to a surface with oxygen vacancies. Analogously, Mg deposition onto MgO produces additional features in the band gap as measured by EELS, and has been assigned to oxygen vacancies (e.g., neutral F centers).[76]

Fig. 19 shows MIES spectra for two SiO_2 thin films prepared by annealing at 1050 and 1200 K, respectively. The 1050K-annealed film exhibited a c(2x2) LEED pattern with weak spots and a high background intensity, suggesting a rough surface with relatively small grains. Annealing at 1200 K leads to an increase in the intensity of the LEED diffraction spots with a concomitant decrease in the background intensity, indicating that a more atomically smooth and ordered surface is formed by the anneal. MIES spectra for the 1200 K-annealed SiO_2 surfaces show much narrower O(2p) features in comparison to those from the 1050 K-annealed SiO_2 thin films, indicating that the widths of the O(2p) bands are a measure of the extended defect (step, corner, etc.) densities. The energy of the valence band in the MIES spectra for both SiO_2 films are

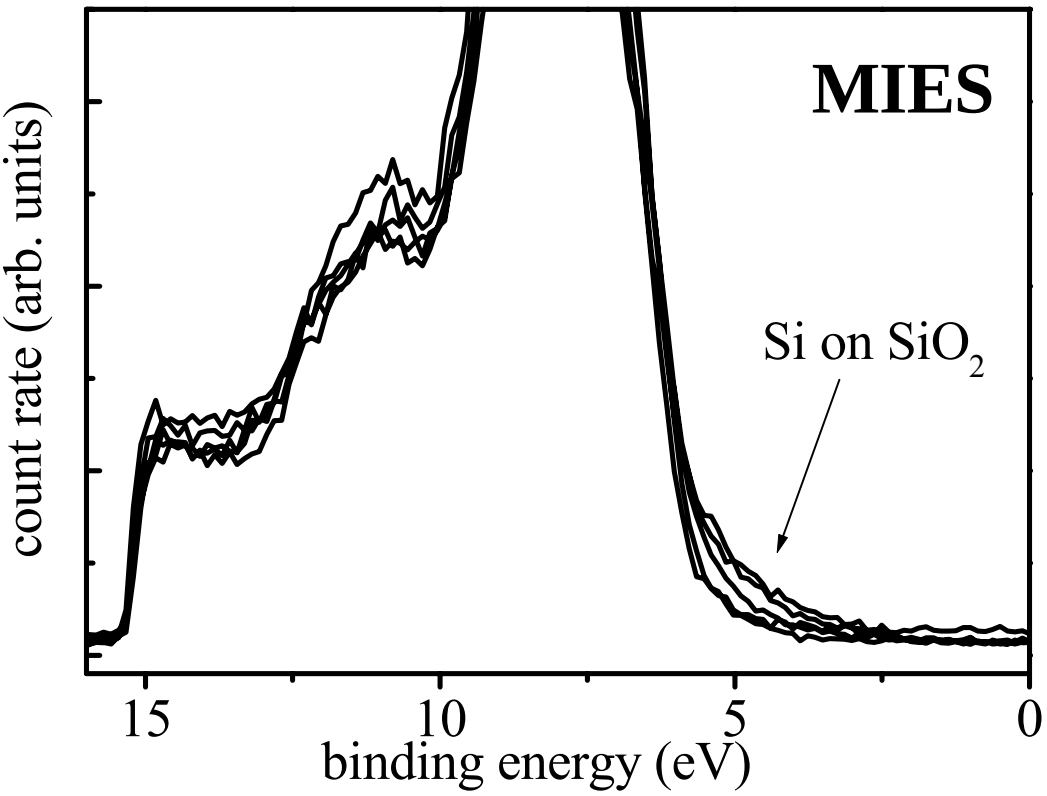

Fig. 18 MIES spectra for a SiO_2 thin film as a function of Si deposition at 300 K.

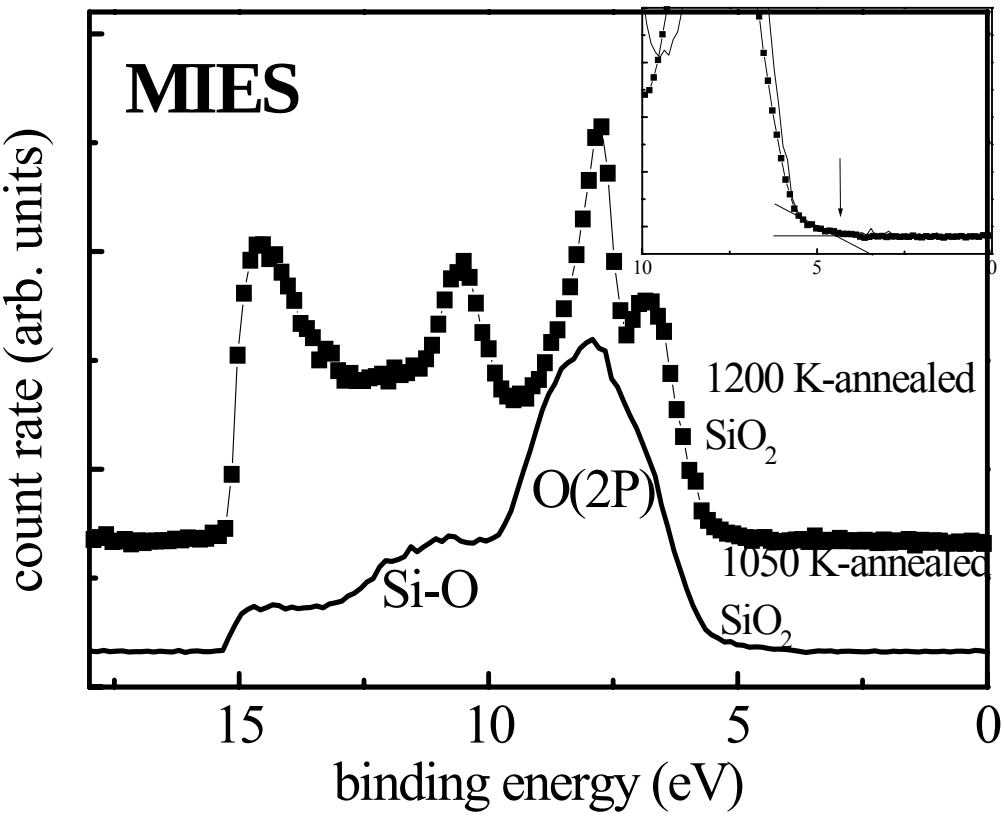

Fig. 19 MIES for the SiO_2 thin films prepared by annealing at 1050 and 1200 K, respectively. An enlarged image of the lower energy region of both spectra is show at top right.

.

identical, showing that the valence band edge is insensitive to surface roughness or grain size. These results are consistent with the band gap states at 3.3 eV corresponding to point defects rather than arising from surface roughness.

In Fig.20 UPS spectra for both SiO_2 surfaces are presented. Similar to the MIES results, UPS also shows changes in the O(2p) features with increasing extended defect densities.

Xe Adsorption

UPS is quite useful for the characterizations of clean and adsorbate-covered solid surfaces. But quantifying UPS data can oftentimes be problematic. Photoemission of adsorbed Xe (PAX) has been shown to be quantitative particularly regarding the outmost surface layer.[77,78] However, in many cases, PAX does not give completely reliable information when superposition of the Xe-peaks and the substrate features occurs. A new method, MIES of adsorbed Xe (MAX), is shown to give more accurate information with respect to binding energies, peak intensities, and full width–at–half-maxima (FWHM) of the Xe 5p-states. It is demonstrated that MAX can be used for the characterization of surfaces for which the application of PAX is difficult due to the superposition of the Xe-peaks and substrate signals.

In Fig. 21, the UPS and MIES spectra for a clean, well-ordered MgO(100) surface are compared with that of the same sample acquired in a Xe background pressure of 5×10^{-5} Torr at a sample temperature of 80K. Under these conditions, only a Xe monolayer is formed on the surface.[79] Usually, Xe monolayer on solid surface gives rise

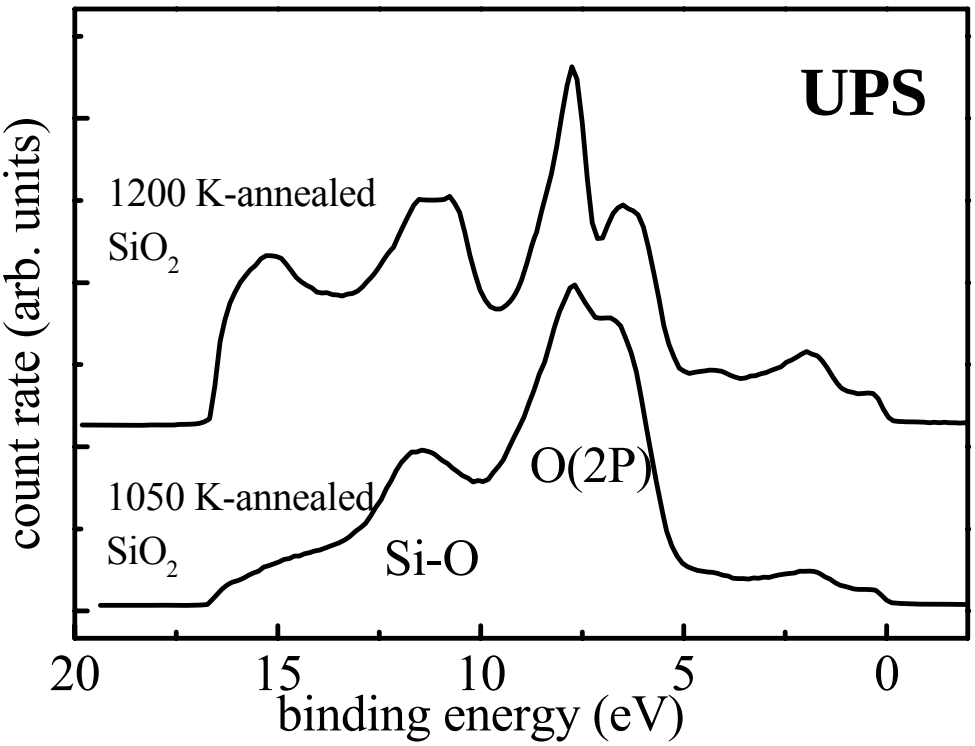

Fig. 20 UPS for the SiO_2 thin films prepared by annealing at 1050 and 1200 K, respectively.

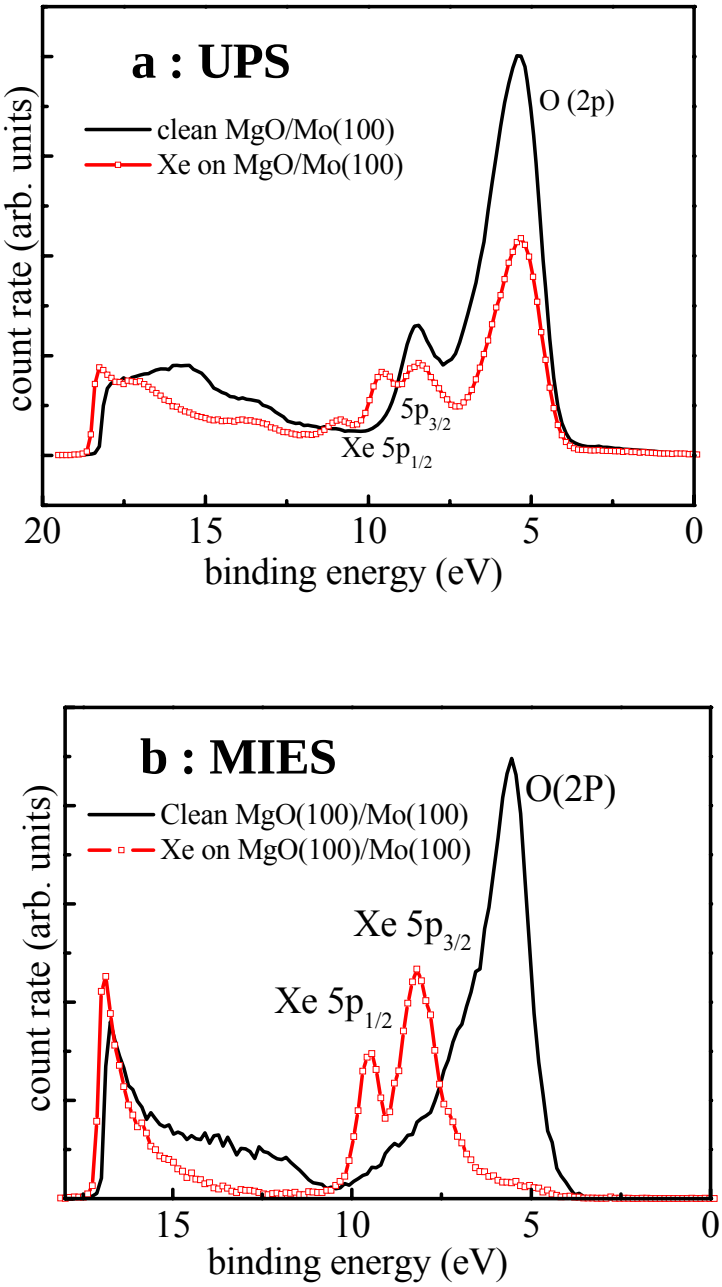

Fig. 21 (a) UPS/PAX and (b) MIES/MAX spectra for MgO thin film on Mo(100).

to a sharp doublet feature in UPS, originating from the $5p_{1/2}$ and $5p_{3/2}$ states of the adsorbed Xe atoms. But for MgO, the Xe induced peaks overlap with the MgO-O(2p) features (Fig. 21a), so the features from adsorbed Xe are very difficult to see. In contrast to UPS, MIES is exclusively sensitive to the surface outermost layer, so the MIES spectrum in Fig. 21b only shows sharp peaks from the Xe-5p states. The MgO-O(2p) features are completely attenuated, illustrating that MIES for adsorbed xenon can be used for the systems in which the application of the PAX is limited due to the superposition of the Xe and substrate features.

Similar experiments have been carried out on the SiO_2 thin films. The MAX spectrum of SiO_2 thin film (Fig. 22b) shows two narrow Xe-5p peaks, whose widths are comparable to those from the clean MgO(100) (Fig. 21) surface, indicating that the SiO_2/Mo(112) surface is quite uniform, and the wettability of a SiO_2 thin film on Mo(112) is very high. In contrast to MAX, the Xe 5p-features and the O(2p) peaks from SiO_2 overlap in the PAX spectrum (Fig. 22a).

In Fig. 23, the MIES spectra for Mo(100), MgO/Mo(100) and SiO_2/Mo(112) collected with a Xe background pressure of 5×10^{-5} Torr at a sample temperature of 80 K are compared. The Xe $5p_{1/2}$ peak positions for SiO_2/Mo(112), Mo(100), and MgO/Mo(100) are at 7.5 eV, 8.0 eV, and 9.5 eV, respectively. The work functions of SiO_2/Mo(112), Mo(100), and MgO/Mo(100) estimated by the energy positions of the on-set of the secondary electrons in the UPS spectra are 4.9 eV, 4.4 eV and 2.9 eV, respectively. Thus, the sums of the work functions and the $5p_{1/2}$ energy positions for these three surfaces are constant, indicating that the Xe $5p_{1/2}$ positions reflect the surface

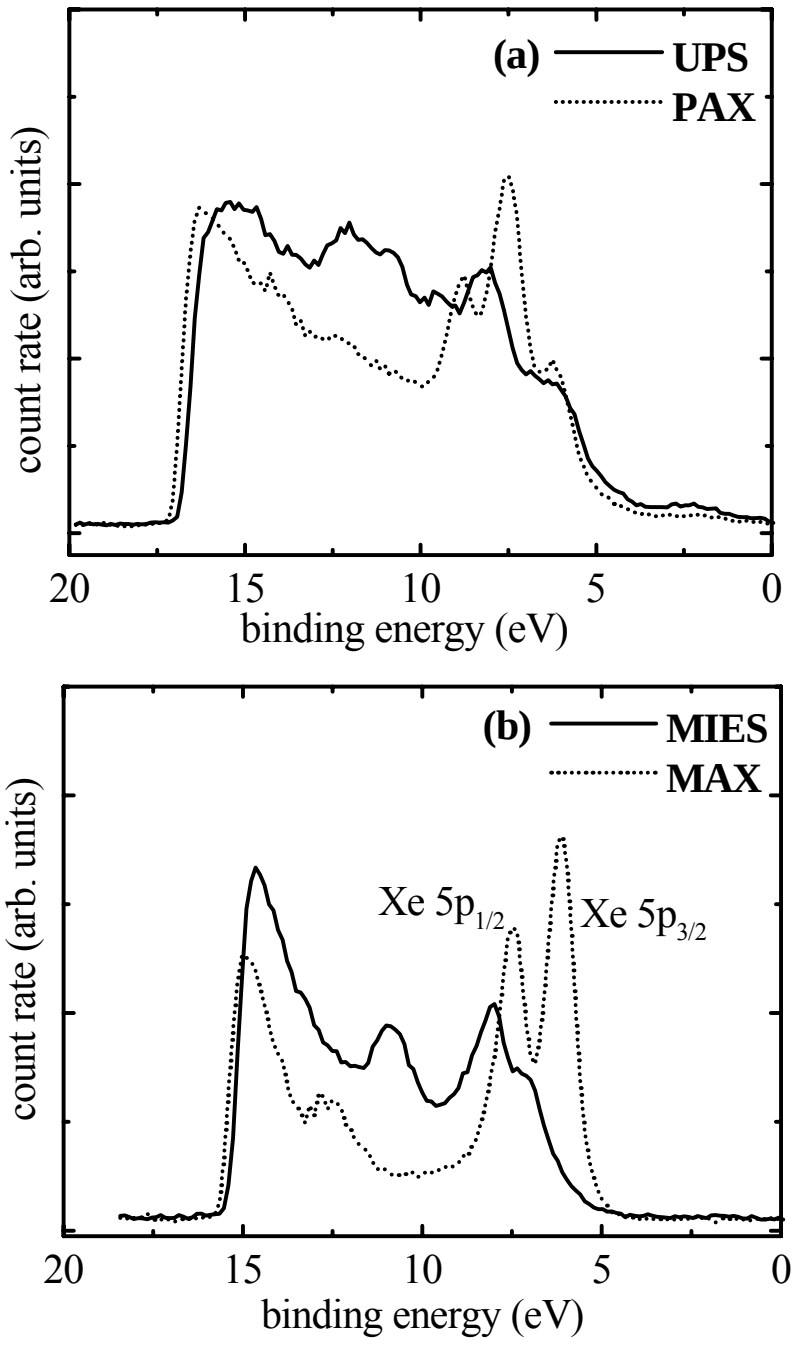

Fig. 22 (a) UPS/PAX and (b) MIES/MAX spectra for SiO_2 thin film on Mo(112).

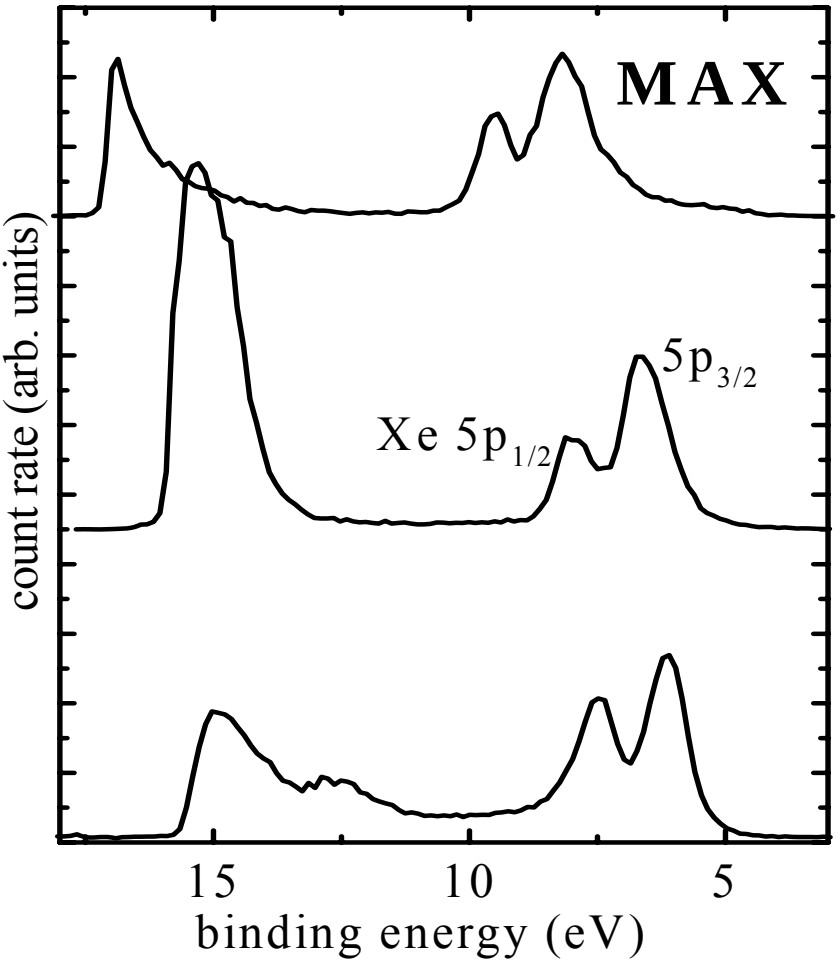

Fig. 23 MIES spectra of adsorbed Xe (MAX) from (a) SiO_2/Mo(112), (b) Mo(100), and (c) MgO/Mo(100).

work function. It has been suggested that the $5p_{1/2}$ binding energy of a Xe atom on the surface is pinned to the vacuum level of the surface such that the energy position of the Xe $5p_{1/2}$ level with respect to the Fermi level can provide information about the surface work function,[78] in agreement with the results of Fig. 23. The results in Fig. 23 show that MAX can be used for wide band gap materials as well as metals, whereas the application of MIES is problematic for most transition metals.

MAX has also been utilized to characterize the surface defect sites. Fig. 24 presents the MIES and MAS spectra for low and high defect MgO(100) surfaces. The 300K-grown MgO(100) film shows broader Xe 5p features in comparison to those of the 1150 K-annealed MgO(100) films, indicating that the surface of the 300K-grown MgO(100) film is more heterogeneous. The MAX results are in line with the MIES and LEED results, since the 300 K-grown MgO film shows a broader O(2p) band, and a more diffuse LEED pattern, signatures for a higher defect density.[59]

The MAX spectrum of the high-defect MgO surface shows much less resolved features at lower binding energies with respect to the Xe 5p states of the low-defect surface. Assuming that the Xe-5p level is pinned to the vacuum level of the surface, the local work function of the defect sites in the 300K-grown MgO(100) films should be higher than that of the perfect MgO(100) surface. However, the work function of the 300K-grown MgO(100) film determined by the on-set of the secondary electrons in UPS is lower than that of the vacuum-annealed MgO(100) film, which does not agree with the MAX-results. In contrast to the results for the low-defect surfaces (Fig. 23), Fig. 24 demonstrates that the Xe 5p levels in MAX do not always reflect the surface local work

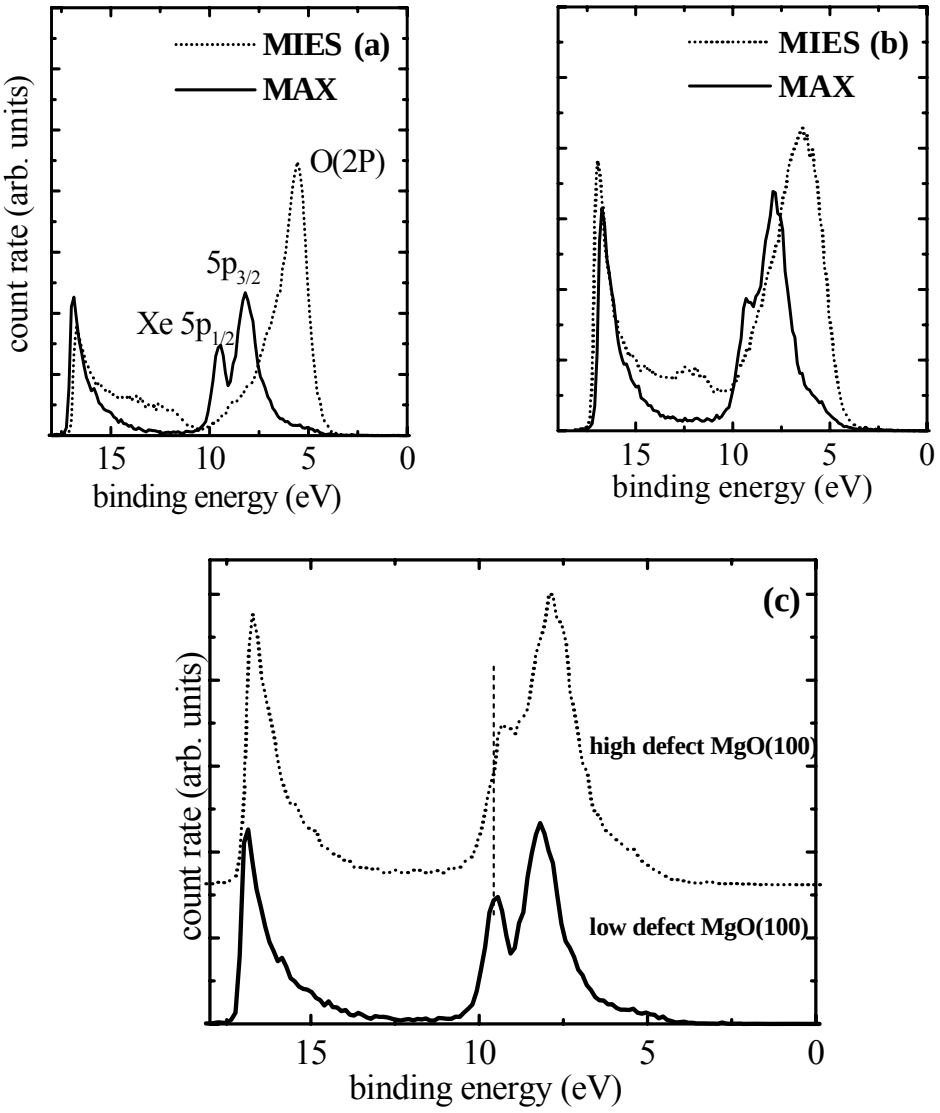

Fig. 24 MIES and MAX for MgO surfaces with (a) low and (b) high defect densities. In (c), MAX spectra for both surfaces are compared. The high defect surface was prepared by deposition of Mg in an O_2 background of 1 x 10^{-7} Torr at room temperature. The low defective surface was prepared by deposition of Mg in a O_2 background of 1 x 10^{-7} Torr at 600 K, followed by multiple anneals at 1150 K.

functions, and thus one should be careful in the determination for the local work functions of a heterogeneous surface using the Xe 5p energy positions, in particular for defect sites.

In Fig. 25, MAX spectra are shown for high- and low-defect SiO_2 surfaces prepared by annealing the 800 K-prepared film at 1050 and 1200 K, respectively. The defect sites on the high defect SiO_2 surface can be identified by a shoulder at higher binding energies with respect to the narrow doublet feature. For the high defect SiO_2 surface, no band gap state can be found in MIES, indicating that point defects such as oxygen vacancies and oxygen surplus sites are not present.[58] A broadening of the O(2p) band was found for the high-defect surface, resulting perhaps from an increased extended defect density, suggesting that the defect sites identified using MAX are extended defect sites such as steps and kinks.

In conclusion, SiO_2 thin films on Mo(112) have been characterized using MIES and UPS. The electronic properties of SiO_2 thin films with a thickness of 0.7–0.8 nm are identical to those of bulk SiO_2. For defective SiO_2 surfaces prepared by three different

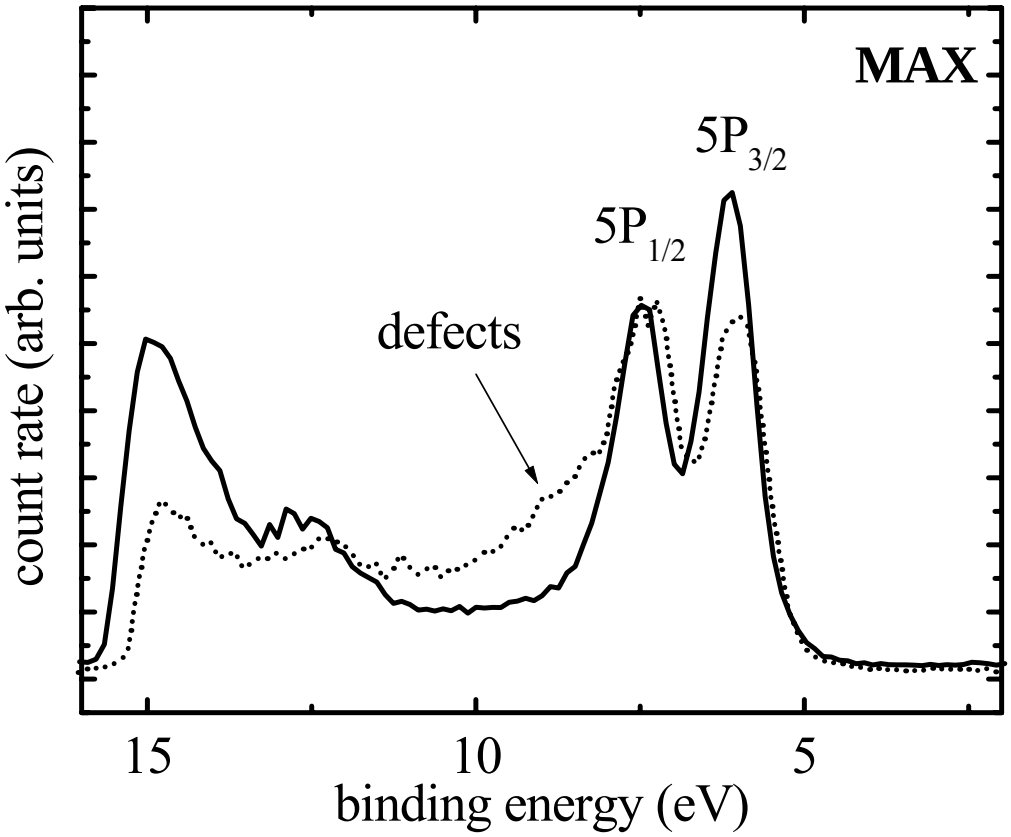

Fig. 25 MAX for low and high defect SiO_2 films on Mo(112).

ways (synthesis without an anneal, e-beam bombardment and Si-deposition), additional features are observed in the band gap using MIES that are consistent with theoretical predictions of additional occupied states in the band gap of SiO_2 due to vacancies or excess oxygen. In contrast, UPS did not show any changes within the band gap in the presence of these defects. Extended defect sites on SiO_2 are identified using MIES/UPS by a narrowing of the O(2P) features with a reduction in the density of extended defect sites. In addition, PAX has been shown to yield ambiguous results when the Xe-features overlap with the substrate signals. With MAX, the substrate signals are completely quenched, and only the Xe features appear due to the high surface sensitivity of MIES. MAX, therefore, can provide more accurate information than PAX with respect to binding energies, energy positions, and the widths of the Xe 5p states. Several examples are given to show that MAX can be informative for the quantitative characterizations of uniform and non-uniform surfaces, illustrating that, in contrast to MIES, MAX can be used on metals as well as wide band gap materials.

Ag/SiO_2/Mo(112)*

The interaction of metals with oxides is central to various technologies. Because metals generally interact weakly with oxide surfaces, three-dimensional metal growth typically occurs. Defects sites, however, can lead to a much stronger interaction between the oxide and the metal,[80-83] leading to preferential nucleation of metal atoms at defect sites.[84,85] Moreover, defect sites can modify the electronic and chemical properties of supported metals, especially as a result of charge transfer between the substrate and the metal cluster.[80,86,87] As a consequence, defect sites are thought to play an important role in altering the properties of oxide-supported metal catalysts. In this work, the interaction of Ag with SiO_2 surfaces of varying defect concentration has been studied using MIES and UPS. Ag was chosen because of its relevance to a variety of catalytic processes. For example, highly dispersed Ag clusters have recently been shown to exhibit interesting size dependent variation for selective catalytic oxidation.[88]

MIES and UPS spectra collected from a low defect SiO_2 surface as a function of Ag coverage at room temperature are shown in Figs. 26 and 27. With increasing Ag coverage, the O(2p) feature attenuates, and concomitantly new Ag-related features appear. Based on previous results from Kempter, et al,[89] the Ag-related features between 2-10 eV in MIES are attributed to the electron emission from Ag 5s and 4d

---

* Reproduced in part with permission from: Kim, Y. D.; Wei, T.; Wendt, S.; Goodman, D. W. *Langmuir*, **2003**, 19, 7929, Copyright 2005 American Chemical Society.

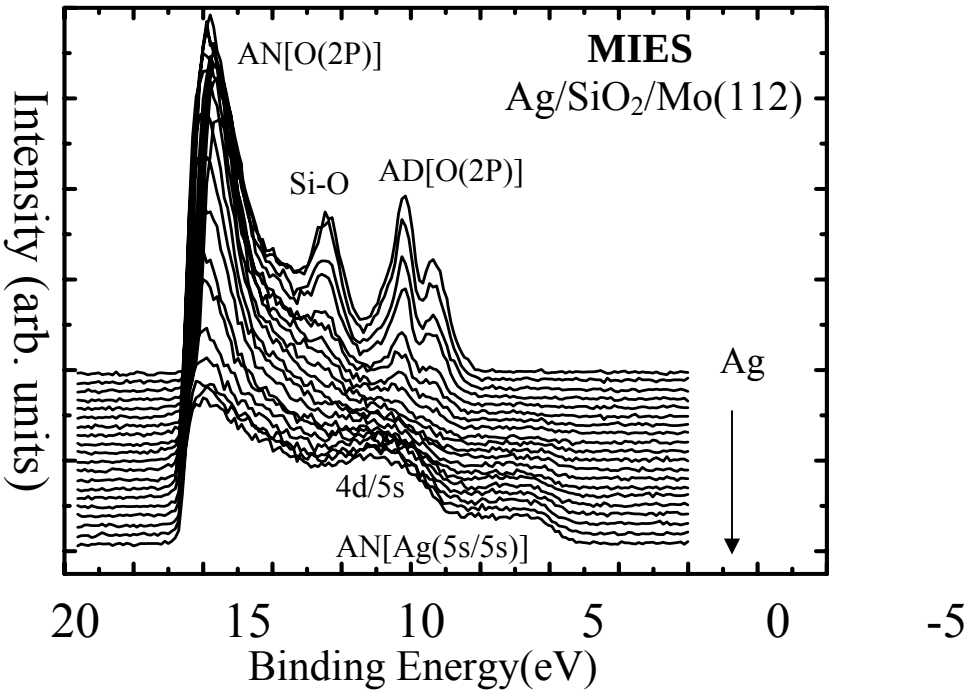

Fig. 26 MIES spectra collected from a low-defect SiO_2 surface as a function of Ag exposure.

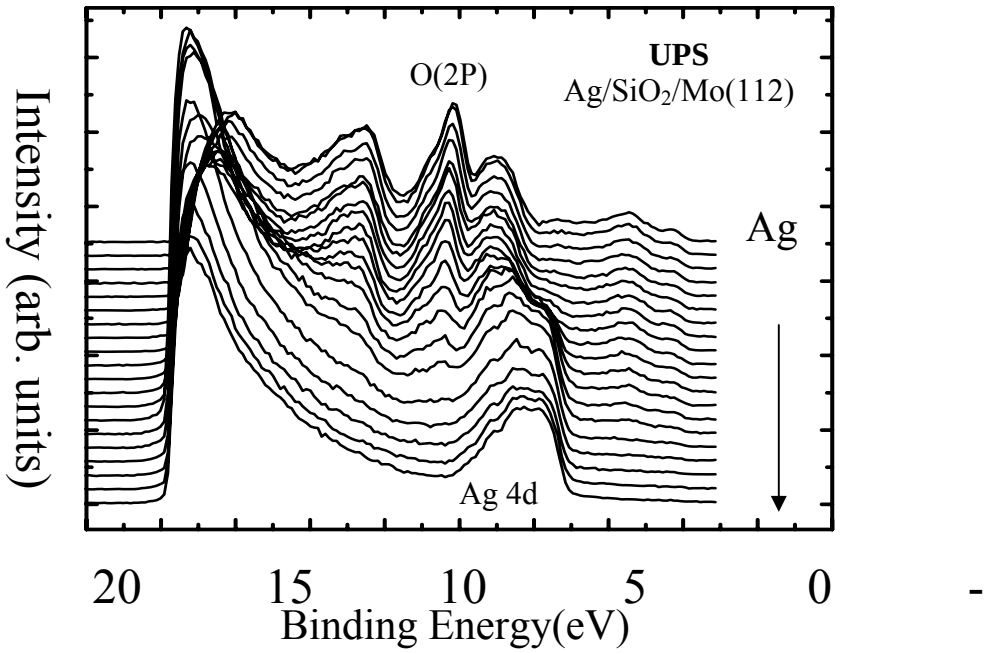

Fig. 27 UPS spectra collected from a low-defect SiO_2 surface as a function of Ag exposure.

bands and arise from a combination of resonance ionization (RI) and Auger neutralization (AN) mechanisms. Due to the relatively high work function of Ag, no Auger deexcitation features for Ag are observed.[48] The feature at 14 eV corresponds to the (RI + AN) feature of SiO_2-O(2p), i. e., He^+ formed at Ag clusters via the RI mechanism interact with the bare SiO_2 surface, and as a consequence, electrons are emitted from the O(2p) band of SiO_2 via the AN process. For a more detailed description of this MIES mechanism, see Ref. [48] and [89].

In Fig. 28, the Ag(5s/5s)-AN and O(2p)-AN features as well as the work function versus the Ag coverage (from the data of Figs. 26 and 27) are summarized. The work function data of Fig. 28b were acquired by noting the energy of the onset of secondary electrons in UPS. The O(2p)-AN feature initially grows as a function of the Ag coverage because the number of He^+ produced by the RI mechanism at the Ag clusters increases with increasing Ag coverage.[89] At higher Ag coverages, the intensity of the O(2p)-AN feature is reduced because the area of the uncovered SiO_2 surface decreases.[89] The intensity of the Ag(5s/5s)-AN feature increases linearly initially, whereas at higher Ag coverages (above 0.5 ML) the growth rate of this feature is attenuated. The work function (Fig. 28b) decreases rapidly at the initial stage of the Ag exposure and is followed by a slight increase at Ag coverages above 0.5 ML. The linear increase in the intensity of the Ag(5s/5s)-AN feature and the linear decrease of the work function at the early stage of Ag deposition may suggest that the Ag initially wets the SiO_2 surface, i.e., 2D-clusters are formed. Above the coverage of 0.5 ML, Ag likely grows with a 3D morphology, leading to the attenuated change in the work function and intensity of the

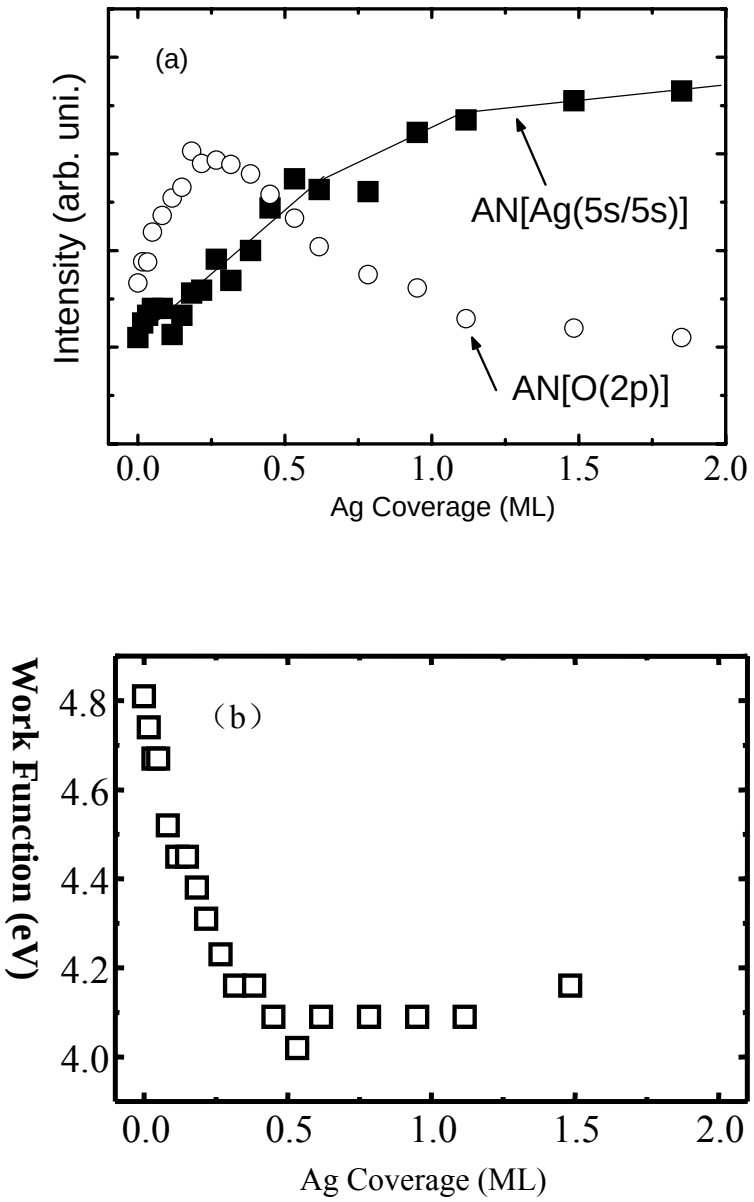

Fig. 28 (a) Changes in the intensities of the MIES O(2p)–AN and Ag (5s/5s)–AN features, and (b) work function from a low–defect surface as a function of Ag coverage as determined by the onset of secondary electrons in UPS.

Ag (5s/5s)-AN feature. For Ag/MgO systems similar changes of the AN-feature intensities also have been interpreted in terms of a 2D-3D transition.[89] It is noteworthy that a 2D-3D transition in the growth mode of metal clusters with increasing metal coverage has been observed for several metal/oxide systems.[13,90,91]

The work function of Ag is between 4.1-4.6 eV, depending on the surface morphology, whereas the work function for SiO_2 films is approximately 5.0 eV. Considering that the work function of a non-uniform surface is simply the geometrical average of the local work functions, and that the work function of the Ag clusters is constant as a function of Ag coverage, a monotonic decrease in the work function with increasing Ag exposure is anticipated. The data, however, show an initial decrease of the work function at relatively low Ag coverages, followed by an increase as the Ag coverage is increased above 0.5 ML (Fig. 28b). The most plausible explanation for the minimum in the work function as a function of Ag coverage is that at relative low Ag coverages, Ag clusters become partially positively charged via transfer of electronic charge from Ag to SiO_2. Similar work function changes for Ni/TiO_2,[92] Ag/MgO,[89] and Cu/ZnO[91] have been interpreted in terms of charge transfer from the metal to the oxides. Previous XPS studies have also indicated that charge transfer from Ag to SiO_2 takes place,[93] consistent with the present data. Also, recent theoretical calculations for the Cu/SiO_2 systems have shown that metal clusters can become charge deficient on a perfect SiO_2 surface, leading to electrostatic bonding between the metal cluster and two nearest-neighbor O atoms. That is, polarization of charge on the metal cluster can occur in the absence of defects. An alternative but less likely explanation for the minimum in

the work function as a function of Ag coverage, is that the smaller clusters exhibit greater surface roughness giving rise to significantly lower local work functions.[94]

To obtain a better understanding of the interactions between Ag and defect sites on SiO_2, MIES/UPS data were acquired as a function of Ag exposure on SiO_2 surfaces with varying defect densities. Ag adsorption on various SiO_2 surfaces yields similar changes in MIES and UPS compared with the data of Fig. 26 and 27, i.e., a decrease in the O(2p) feature, an increase in the Ag-related features, and an initial increase followed by a decrease in the intensity of the O(2p)-AN features, with increasing Ag exposure. The work function changes of the defective SiO_2 surface as a function of Ag exposure are quite analogous to those of the low defect SiO_2 surface (Fig. 29). These results are markedly different in comparison with the corresponding data for MgO(100),[80] shown in Fig. 30. For a high defective MgO surface a pronounced minimum at low Ag coverage occurs, whereas for a low defect MgO surface, the work function gradually increases with increasing Ag exposure. For various SiO_2 surfaces there is no significant influence of defect density on the work function as a function of the Ag coverage, i.e. the three curves in Fig. 29 are almost identical. For the SiO_2 films the changes of the work function as a function of the Ag coverage for high and low defective surfaces are much less pronounced than for MgO, a more ionic oxide than SiO_2.

It is generally accepted that interactions of metals with defective oxide surfaces are much stronger than those with a defect-free oxide surface. According to recent theoretical studies,[81-83] this is generally thought to be true for SiO_2. The work function data presented here indicate that the interactions of Ag with regular and defect sites are

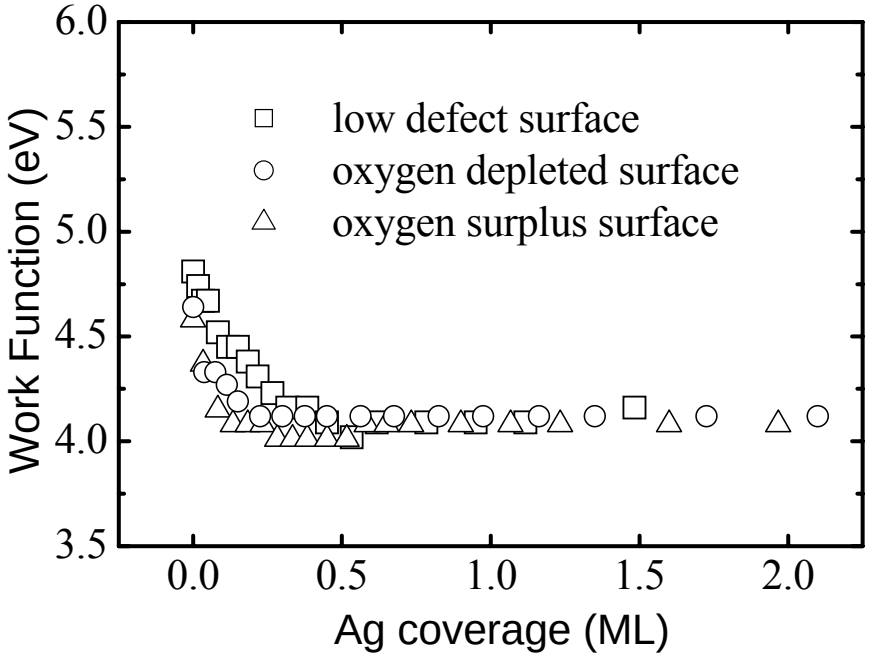

Fig. 29 Work function changes for various SiO_2 surfaces as a function of Ag coverage determined by the onset of secondary electrons in UPS. The oxygen depleted surface was prepared by Si deposition on SiO_2, and the oxygen surplus surface was prepared by oxygen treatment of a Si/SiO_2 surface at 800 K.

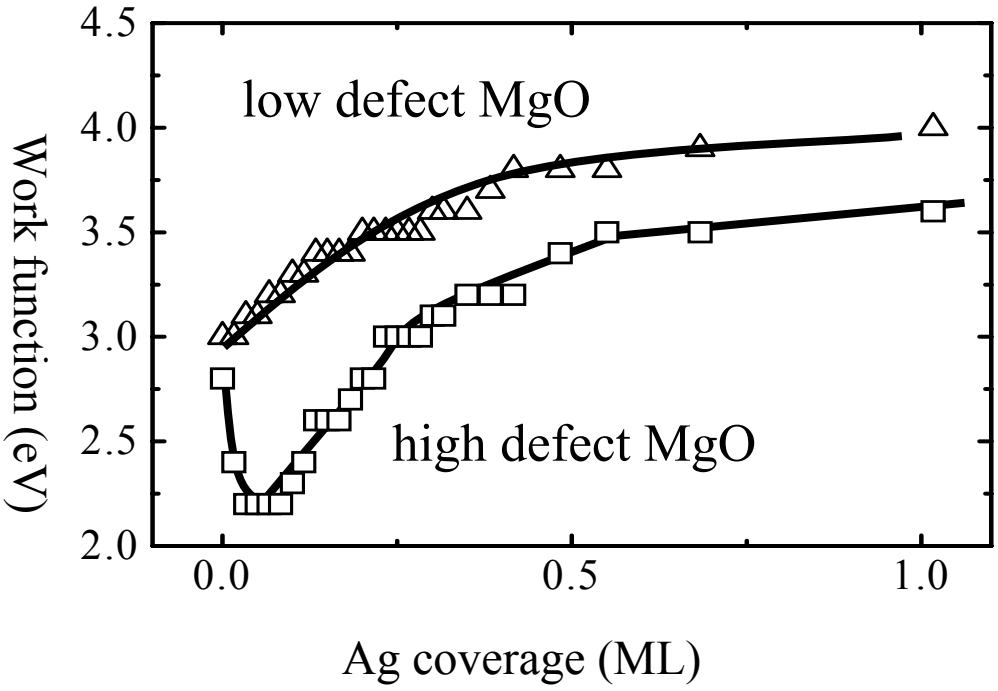

Fig. 30 Work function changes from UPS for low and high defect MgO surfaces as a function of Ag coverage. The high defect MgO surface was produced by sputtering and heating the low defect MgO surface to 600 K.

almost identical in terms of the electrostatic interaction resulting from the partial charge transfer from Ag to the substrate. These results suggest that relative to regular sites, the interaction between Ag and defect sites on SiO_2 may be enhanced by relative strong covalent bonds. Recent theoretical investigations have shown that transition metals such as Pd, and Cu and various point defects on SiO_2 form strong covalent bonds,[82,83] whereas for MgO, enhanced charge transfer between point defects and adsorbed metals has been suggested.[86,87,95] The results found in these recent theoretical studies are consistent with the work function data for SiO_2 and MgO presented here (Figs. 29 and 30).

To summarize, the adsorptive behavior of Ag on low and high defect SiO_2 surfaces has been studied with MIES and UPS. Changes of the MIES spectrum of a low defect SiO_2 surface as a function of Ag exposure can be interpreted in terms of 2D growth at low Ag coverages, followed by 3D growth at higher coverages. In contrast to previous studies on MgO, charge transfer between Ag and SiO_2 is not significantly enhanced in the presence of defect sites, suggesting that the bonding between Ag and defect sites on SiO_2 is primarily covalent.

Pd–Au/Mo(110)*

Alloying is widely used to alter the chemical properties of metal surfaces.[96,97] Especially, the catalytic properties of alloys are often remarkably different from those of the single components.[98,99] This prospect of making novel catalysts with improved properties leads to continuous interest in the surface science study of model alloy systems. The Pd-Au alloys are particularly important because of their application in the vinyl acetate synthesis reaction.[100-102]

Early studies on the Pd–Au alloys have been mainly performed on two types of model systems: stable bulk alloys and thin film surface alloys prepared by deposition one metal on the single crystal of the other (like deposition of Pd on Au(111) surface or vice versa). However, these studies were limited because of the difficulties in the preparation and the control of surface alloy concentrations. To avoid this problem, the Pd–Au alloy films prepared by depositing both metals on the third metal subtract Mo(110) were proposed recently.[103] Since both Pd and Au have limited solubilities into Mo(110), a stable alloy film would be formed after sequent annealing. Previous low energy electron diffraction (LEED) studies indicated pseudomorphic, (111)-like surface was formed when multilayer Pd or Au grown on a Mo(110) substrate.[30,31,104-106] So the mixed Pd-Au thin films prepared in the same manner could be expected to mimic (111)-like bulk alloy surface. Besides the flexibility of changing bulk Pd to Au ratios, this

---

* Reproduced in part with permission from: Yi, C.W.; Luo, K.; Wei, T.; Goodman, D.W. *Journal of Physical Chemistry B* **2005**,109,18535, Copyright 2005 American Chemical Society.

model system also has the merits in the easy preparation. The only complication probably arises from the influence of Mo subtract to these alloy films. Relatively thick film (total 10 ML) was used in order to minimize this effect.

The surface composition, morphology and electronic structures of Pd–Au model catalysts are the most studied topics in the literatures. Strong surface segregation of Au has been observed by Auger electron spectroscopy (AES), low energy ion scattering spectroscopy (LEISS) and scanning tunneling microscopy (STM).[18-21,107-109] Using electronic spectroscopic methods, like X-ray photoelectron spectroscopy (XPS), X-ray absorption near-edge spectra (XANES) and ultraviolet photoelectron spectroscopy (UPS), the net charge transfer from the Pd site to Au site was found to be very small due to the electron redistribution or orbital rehybridization.[110-112] Several studies also indicated the thermal annealing temperature and time are crucial to the alloy surface morphology and composition, normally high temperature annealing smoothes out the alloy surface, and drives the low–surface–free-energy component enriched on the surface.[22,24,103,113] In addition, ensemble effects have been purposed to play an dominant role in the enhancement of catalytic reactivity for several reactions.[22,23,32,114]

In the present work, a combination of XPS and LEISS were used to investigate the surface concentration, the extent of alloying, and the electronic properties of Pd-Au bimetallic films. Both IRAS and TPD using CO as a probe molecule were used to elucidate the surface structure, the Pd-Au surface ensembles, and the corresponding variation in chemical properties. This study demonstrates a facile method for studying

the surface versus bulk composition of mixed - metal phases using mutilayer metal films on a refractory metal substrate.

XPS and LEISS

In order to investigate alloy formation, the electronic properties, and the surface concentration of the Pd-Au films, XPS and LEISS measurements were performed. For Pd, the less intense Pd $3d_{3/2}$ feature was monitored because of the overlap of the Pd $3d_{5/2}$ and the Au $4d_{5/2}$ peak. Fig. 31 shows Au $4f_{7/2}$ and Pd $3d_{3/2}$ core-level binding energies as a function of annealing temperature for 5ML Pd/5ML Au/Mo(110) (Au deposited first) and 5ML Au/5ML Pd/Mo(110) films (Pd deposited first). For 5ML Pd deposited on 5ML Au/Mo(110), the XPS peak position of the Au $4f_{7/2}$ is 83.7 eV at 300 K, gradually shifting toward lower binding energies as the annealing temperature is increased to 600 K. Between 600 and 800 K, the Au $4f_{7/2}$ peak position is steady at 83.3 eV with a slight shift to 83.4 eV upon annealing to 1100 K. At 300 K, the XPS feature of Pd $3d_{3/2}$ is centered at 340.3 eV, gradually shifting to 340 eV at 700 K, then shifting back to 340.7 eV at 1200 K.

Upon annealing to 800 K, the Au $4f_{7/2}$ and Pd $3d_{3/2}$ peak positions shift to lower binding energies by ~ 0.45 eV and ~ 0.15 eV, respectively, relative to bulk Au and Pd. Previously, Lee and co-workers[110] reported that the Pd $3d_{3/2}$ and the Au $4f_{7/2}$ core levels shift to lower binding energies upon alloying, in excellent agreement with the core level shifts of Au $4f_{7/2}$ and Pd $3d_{3/2}$ seen here. These authors also assert that the core-level binding energy shifts conform to a charge compensation model and propose that Au

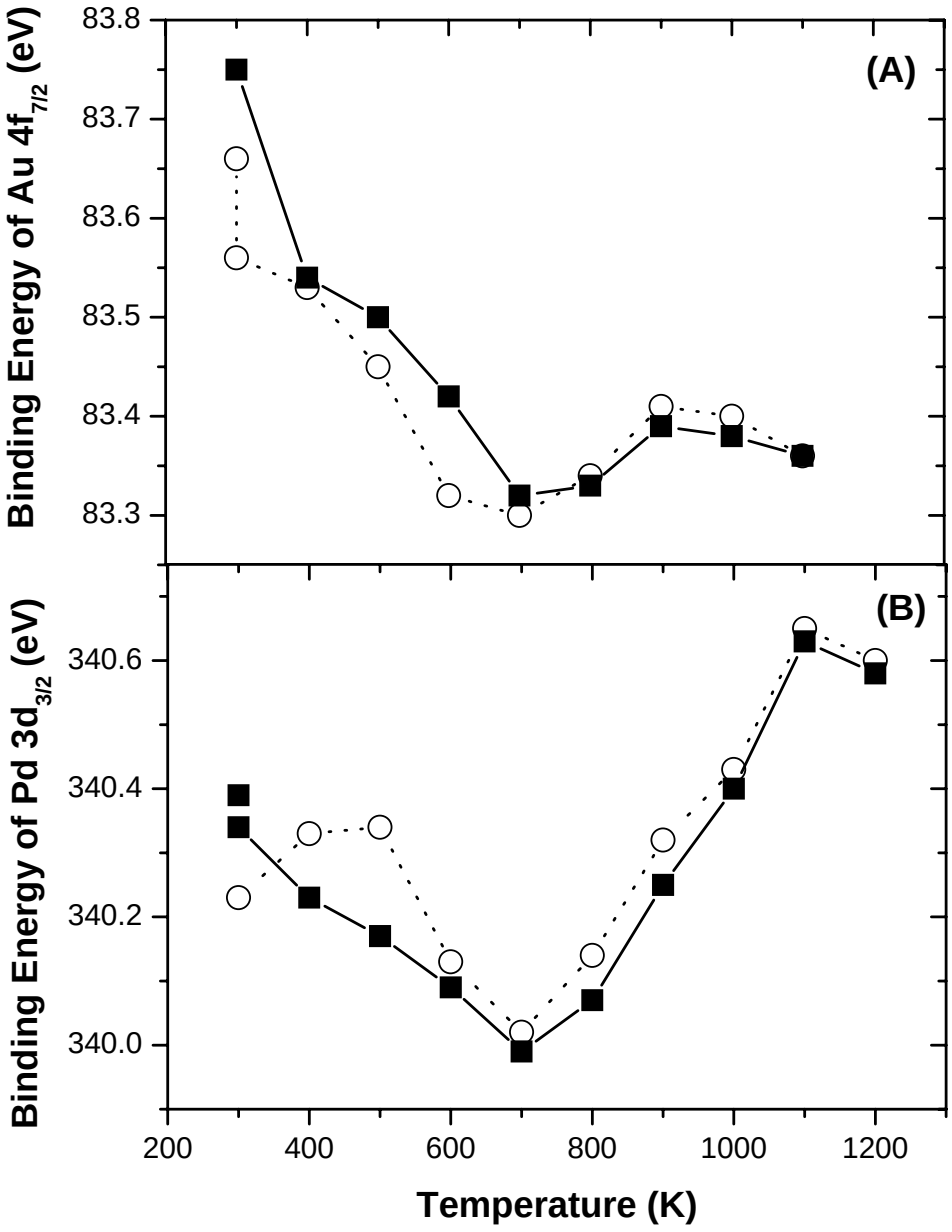

Fig. 31 Core-level binding energy from XPS spectra of Au $4f_{7/2}$ (A) and Pd $3d_{3/2}$ (B) of 5ML Pd/5ML Au/Mo(110) (○) and 5ML Au/5ML Pd/Mo(110) (■) with respect to annealing temperature.

gains *sp*-type electrons and loses *d*-electrons whereas Pd loses *sp*-electrons and gains *d*-electrons.[110] In any case, the core-level binding energy shifts observed here clearly show that alloy formation indeed occurs.

With a further increase in the annealing temperature, the core level of Pd $3d_{3/2}$ shifts to higher binding energy due to desorption of Au. The film thickness of Au-Pd alloy was monitored by attenuation of the Mo $3d_{5/2}$ feature. The thickness of the alloy film begins to decrease as the annealing temperature reaches 1000 K, and is significantly reduced at 1100 K. The TPD results (not shown) indicate that Au desorbs initially followed by Pd. Therefore, at annealing temperatures higher than 1000 K, the film thickness attenuates due to desorption of Au, and the binding energy of Pd $3d_{3/2}$ shifts to higher binding energy due to the strong interaction between Pd overlayers and the Mo substrate.[115]

LEISS was used to determine the surface composition of the Pd-Au alloy surfaces. Fig. 32 shows the LEISS spectra of 5ML Pd/5ML Au/Mo(110) as a function of annealing temperature. Following deposition of 5ML Au onto Mo(110) at 300 K, the Au LEISS feature appears at 1.03 keV whereas no Mo feature is observed at 0.94 keV. After Pd deposition onto 5ML Au / Mo(110), the Pd LEISS feature appears at 0.97 keV, whereas the Au feature is significantly reduced. Due to the Pd-Au inter-diffusion even at room temperature, [116] a Au LEISS feature was still apparent after deposition of 5ML Pd. Upon annealing to 600 K, the Pd peak intensity gradually decreases with a corresponding increase in the Au peak intensity. At elevated annealing temperatures, Au-Pd inter-diffusion is clearly apparent in the series of LEISS spectra of Fig. 32. With

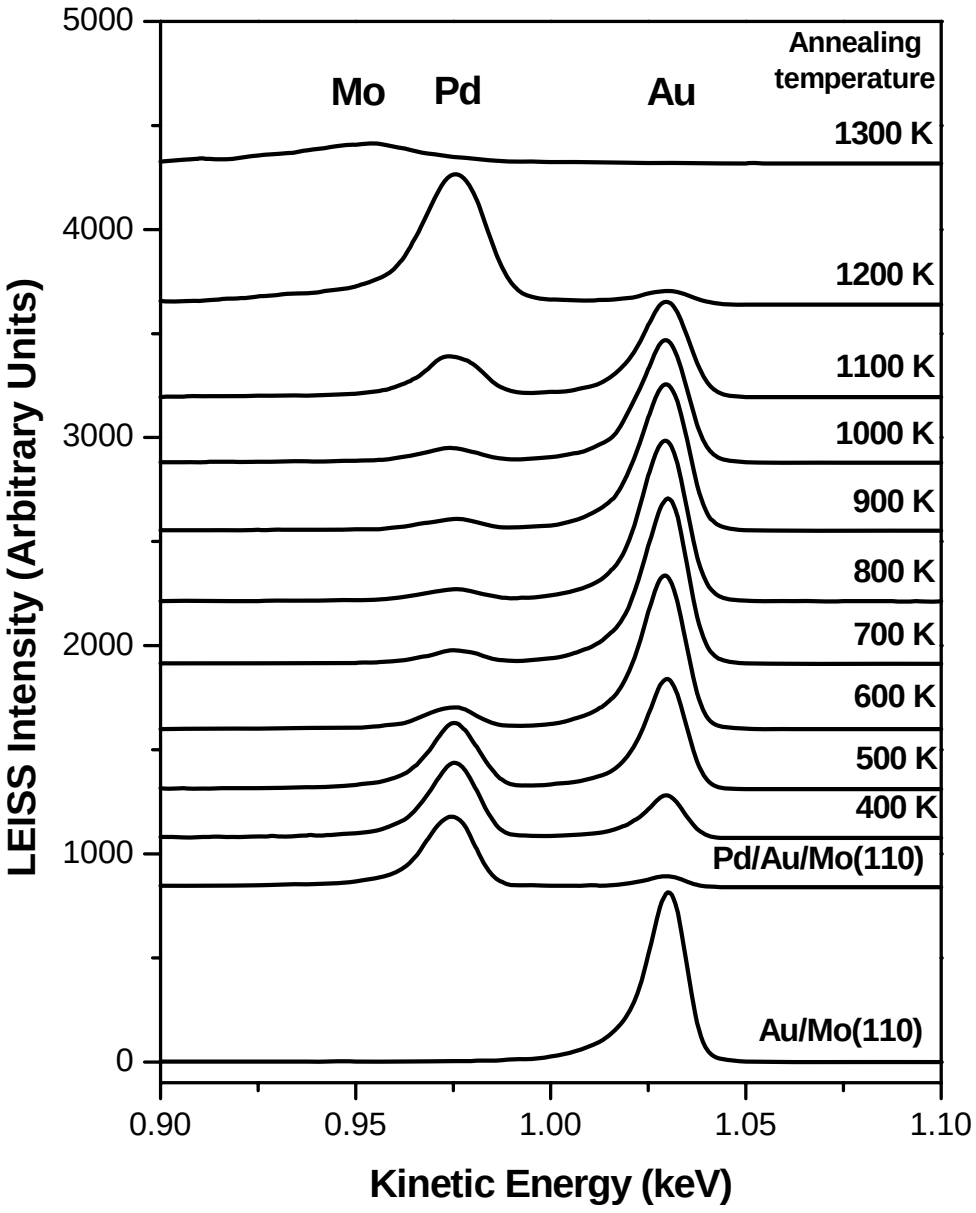

Fig. 32 LEISS spectra of 5ML Pd/5ML Au/Mo(110) as a function of annealing temperature. LEISS spectra were collected at 300 K after the sample was annealed to the specified temperature**.**

further annealing up to 1000 K, the Au and Pd LEISS peak intensities change very little. Finally, the Au and Pd LEISS features disappear at 1200 and 1300 K, respectively, due to desorption of Au and Pd, with a concomitant appearance of Mo scattering features which appear at 0.94 keV following an anneal at 1300 K. Following an anneal at 1200 K, only trace amounts of Au are evident by XPS. Similar to the present work, Shih, *et al.*,[117] report alloying of Pd and Au at room temperature with the disappearance of the Pd Auger signal following an anneal as a result of Pd diffusion into Au. The Auger signals of Au significantly decrease and those of Mo and Pd reappear when a 1ML Pd/multilayer Au/Mo(110) surface is heated to approximately 1150 K.[117]

Based on the results of Fig. 32, the surface concentrations of each constituent of the 5ML Pd-5ML Au mixtures were calculated using Equation (1).[49] For a Au-Pd alloy, the surface concentration of Au is given by

$$c_{Au} = \frac{I_{Au}}{I_{Au} + f_{Au/Pd} \cdot I_{Pd}} \qquad (1)$$

where $f_{Au/Pd}$ is the ratio of the scattering intensity for 10ML Au and 10ML Pd, and I_{Au} and I_{Pd} are the scattering intensity from Au and Pd from the alloy surfaces, respectively.[49,109] Fig. 33 shows the surface concentrations of Pd and Au as a function of annealing temperature. For a 5ML Pd/5ML Au surface (open circle and dashed line), the surface concentration of Au gradually increases from 4 to 80 % with increasing anneal temperature up to 700 K. Between 700 and 1000 K the surface compositions of Pd and Au, $Au_{0.8}Pd_{0.2}$, remain constant. These results are consistent with considerations of the surface free energy, i.e. the surface free energy of Pd (2.043 J/m^2)[118] is higher

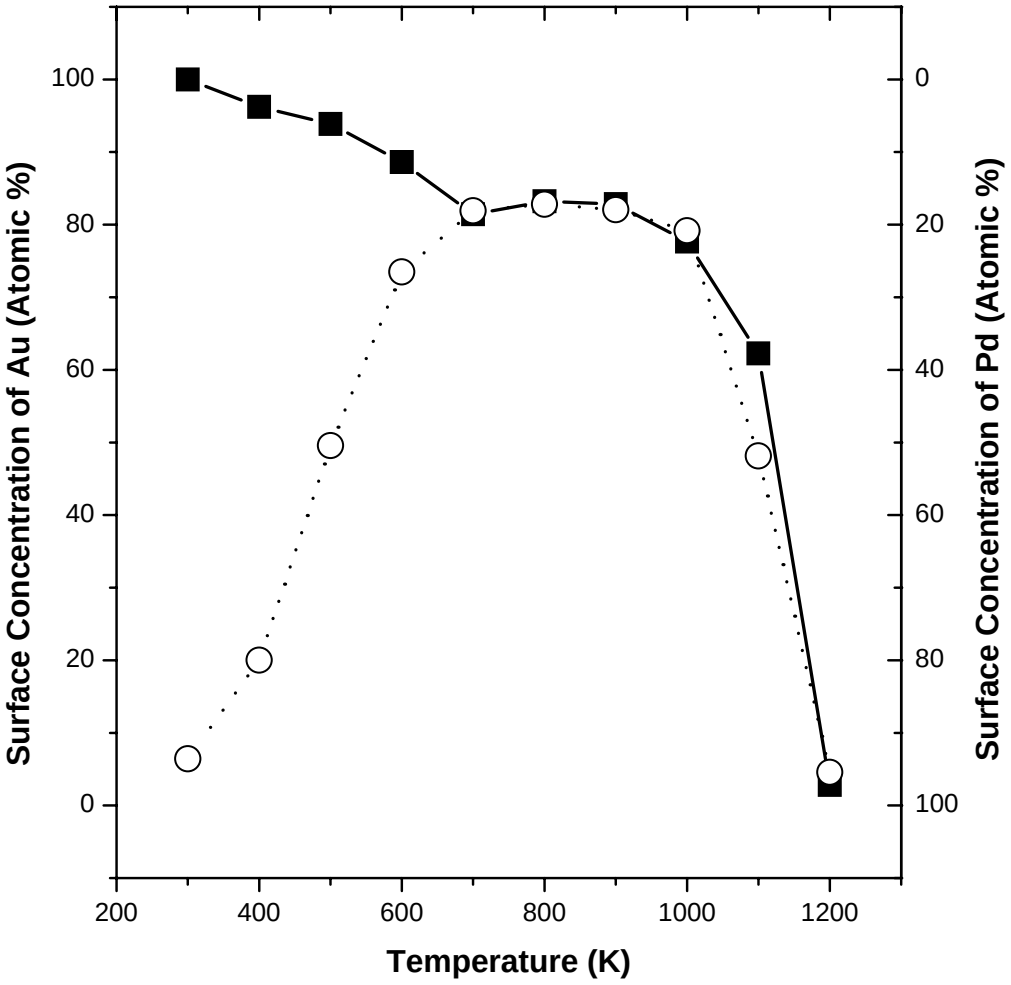

Fig. 33 Surface concentration of Au and Pd of 5ML Pd/5ML Au/Mo(110) (○) and 5ML Au/5ML Pd/Mo(110) (■)as a function of annealing temperature. The sample was annealed at each temperature for 20 minutes.

than that of Au (1.626 J/m^2).[107] Hence, in order to minimize the surface free energy, Au preferentially decorates the surface. Above 1000 K the Au surface concentration abruptly decreases due to Au desorption and Pd becomes dominated on the surface. LEISS experiments of the inverted system, 5ML Au/5ML Pd/Mo(110) (filled square), were also carried out, and the surface concentrations of Pd and Au for each system similarly calculated as above. For 5ML Au/5ML Pd/Mo(110) the Pd surface concentration gradually increases from 0 to 20 % up to 700 K, where an alloy surface, $Au_{0.8}Pd_{0.2}$, forms and remains stable up to 1000 K. At higher annealing temperatures, the Pd surface concentration increases significantly due to Au desorption. Therefore, independent of the order of deposition, 5ML Pd-5ML Au mixtures form a stable alloy between 700 and 1000 K, with a surface consisting of ~20 % Pd and ~80 % Au.

Fig. 34 shows the surface concentrations of Au and Pd for 5ML Pd-5ML Au on Mo(110) as a function of annealing time at 800 K. After depositing 5ML Pd onto 5ML Au/Mo(110) at room temperature, the Au and Pd surface compositions are 4 and 96 atomic %, respectively, as shown in Fig. 33. Following a flash to 800 K, the surface concentration of Au increases to 74 atomic % whereas Pd is reduced to 26 atomic % within one minute; subsequently the concentration of Au gradually increases with anneal time. The initial increase in Au and decrease in Pd surface concentration suggests the rapid Pd-Au inter-diffusion. After a 15 minute anneal at 800 K, the surface concentration of Au and Pd changes to 82 and 18 atomic %, respectively, and the surface concentration remains constant with further annealing. In the inverted system, 5ML Au/5ML Pd/Mo(110), the surface is 89 % Au and 11 % Pd after a flash to 800 K; the

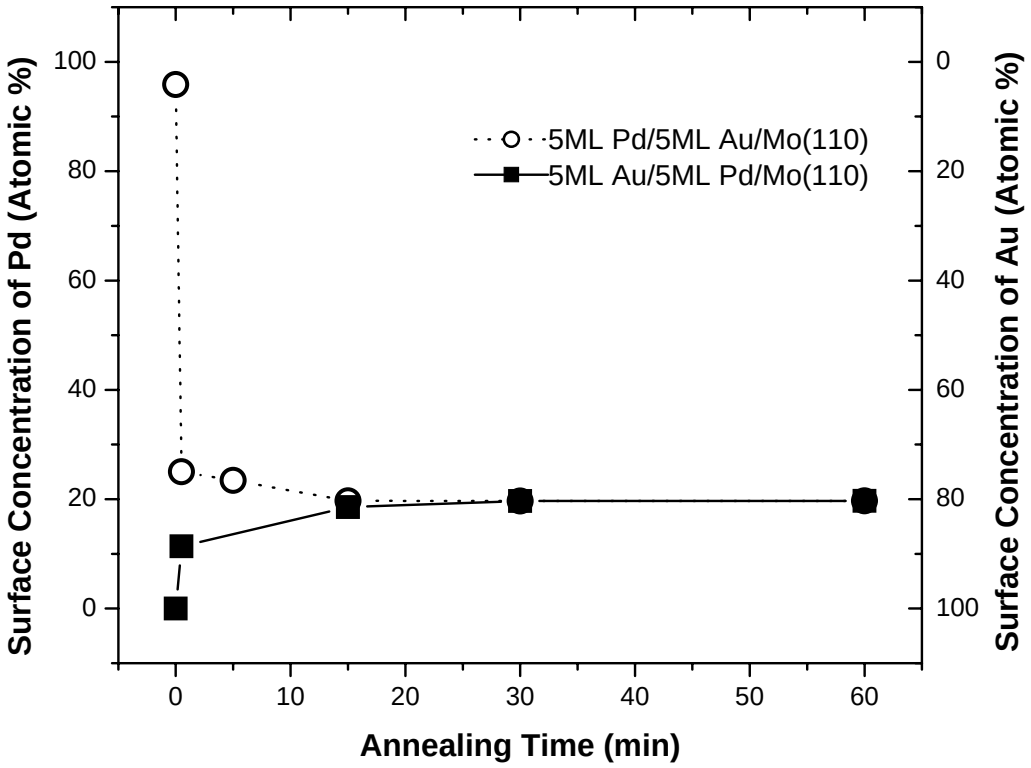

Fig. 34 Surface concentration of 5ML Pd/5ML Au/Mo(110) and 5ML Au/5ML Pd/ Mo(110) measured by LEISS as a function of annealing time at 800 K.

surface composition is constant at 82 % of Au and 18 % of Pd after a 15 minute anneal. The surface concentrations of Au and Pd for both systems converge after a 15 minutes anneal, in excellent agreement with the results of Fig. 32, and consistent with the formation of a stable surface alloy formation.

To further investigate the surface concentration of Pd-Au, LEISS experiments were carried out on different ratios of Pd-Au at a constant total thickness of 10 ML. In Fig. 35, the surface (filled circle and dashed line) versus bulk concentration (filled square and straight line) phase diagram is plotted as a function of the Pd/Au ratio. The Pd-Au mixtures were annealed at 800 K for 20 minutes, and the surface composition determined by LEISS at 300 K. The results show that the surface composition is quite different from the bulk. The surface concentrations of Au range from 40 % to 96 % while the Au bulk concentration varies from 10 % to 90 %. For a 1:1 Pd-Au bulk ratio, the surface consists of 82 % Au atoms. For a 1:3 Pd-Au mixture the surface content is 93.5 % Au, and for a 3:1 Pd-Au mixture, 65 % Au at 800 K. Swartzfager, *et al.*,[119] carried out $^{20}Ne^{+}$ LEISS experiments to investigate the surface concentration of Pd-Au alloys, prepared by melting high purity Au and Pd in a vacuum induction furnace. These authors observed preferential Au segregation following an anneal, and reported the surface compositions to greatly differ from the bulk. For example, a 2:3 and 3:2 Pd-Au mixture exhibited 85 and 70 % Au, respectively, at the surface. The surface compositions found in the present study are consistent with this previous study. This correlation confirms the efficacy of the thin-film methodology used in the current studies. These data also clearly show that the surface composition can be systematically

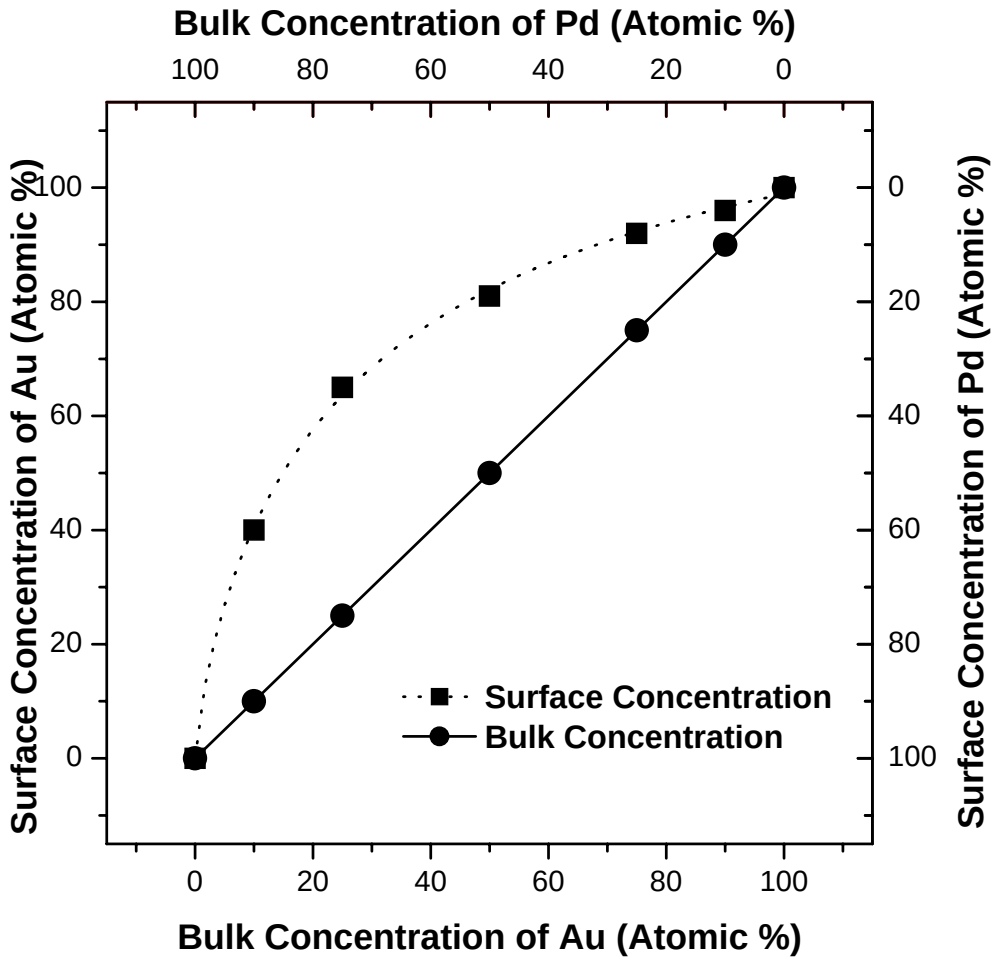

Fig. 35 Surface concentration of various Pd-Au alloys on Mo(110) measured by LEISS compared to the corresponding bulk concentration. The sample was annealed at 800 K for 20 minutes.

controlled by altering the bulk Pd-Au alloy concentration.

IRAS and TPD

IRAS was carried out with CO as a probe molecule in order to determine the structure of Pd-Au surface ensembles. The control experiments on monometallic Pd and Au films were first carried out in order to provide a reference for later Pd–Au alloy films studies. Because of the high surface free energy and dense packing, Mo(110) has been reported as a favorable substrate for a smooth layer by layer growth of fcc metal with (111) orientations.[30,31,104-106,120] Therefore, the vibrational spectra of CO adsorption on the thick Pd film should be comparable with that on Pd(111) single crystal. The coverage-dependent surface structures of CO overlayers on Pd(111) have been identified by different surface science techniques.[36,37,41,121,122] Vibrational spectroscopy, in particular the C–O stretching frequency, has been used for adsorption site assignments.[37,41] According to these studies, up to a CO coverage of 0.33 ML, the ($\sqrt{3} \times \sqrt{3}$)R30°-1CO structure is the dominant phase where CO resides primarily on 3-fold hollow sites. This structure yields a distinctly low C-O vibrational frequency of ~ 1850 cm^{-1}. Increasing the CO coverage to 0.50 ML results in a new overlayer phase, the c(4 × 2)-2CO structure, where CO populates either the bridging sites or 3-fold hollow sites.[122] This structure corresponds to a C-O stretching frequency of ~ 1920 cm^{-1}. Within the CO coverage of 0.5-0.75ML, various complex overlayer structures with CO mainly on bridging sites are reported, displaying a CO vibrational band near 1965 cm^{-1}. Finally, the CO overage reaches saturation at 0.75ML, the adsorbate structure transforms

to a (2×2)-3CO phase, with CO occupying both atop and 3-fold hollow sites corresponding to vibrational features at 2110 and 1895 cm^{-1}, respectively. A phase diagram showing the transition between these CO overlayer structures at various temperatures and pressures was obtained by Goodman *et al.* based on IRAS data.[39,123]

Fig. 36 shows an IRAS annealing series for a 10 ML Pd film on Mo(110) in a 5×10^{-8} Torr CO background pressure. The spectra are independent to the direction of the temperature variation, provided that the film is annealed in the CO background to 600K. At a sample temperature of 450 K, a broad peak appearing at about 1845 cm^{-1} is first observed, which can be attributed to CO bound primarily to 3-fold hollow sites. As the sample is cooled and the CO equilibrium coverage increases, this broad feature sharpens and shifts continuously to a higher frequency at about 1962 cm^{-1}, consistent with a more ordered adsorbate superstructure in which mainly the bridging sites are occupied. In conditions below 200 K a sudden change in the spectrum is apparent. Two sharp, new features grow up at 2109 and 1892 cm^{-1}, while the intensity of the bridging CO peak decreases slowly. This corresponds well with the transition of CO adsorption from bridging sites to a combination of atop and three-fold hollow sites. Besides these well-defined, intense bands, a weak feature at 2086 cm^{-1} is evident in the temperature range of 300 to 200 K without any frequency shift. An identical feature was observed previously in Pd(111) single crystal studies at both UHV and atmospherical conditions. Goodman *et. al.* and his coworkers assigned this feature as a small amount of CO adsorbed onto Pd atop sites, possibly due to a slight disorder in the CO overlayer or a mismatch between the compressed CO c(4×2) overlayer and the Pd(111) substrate that forces some CO onto

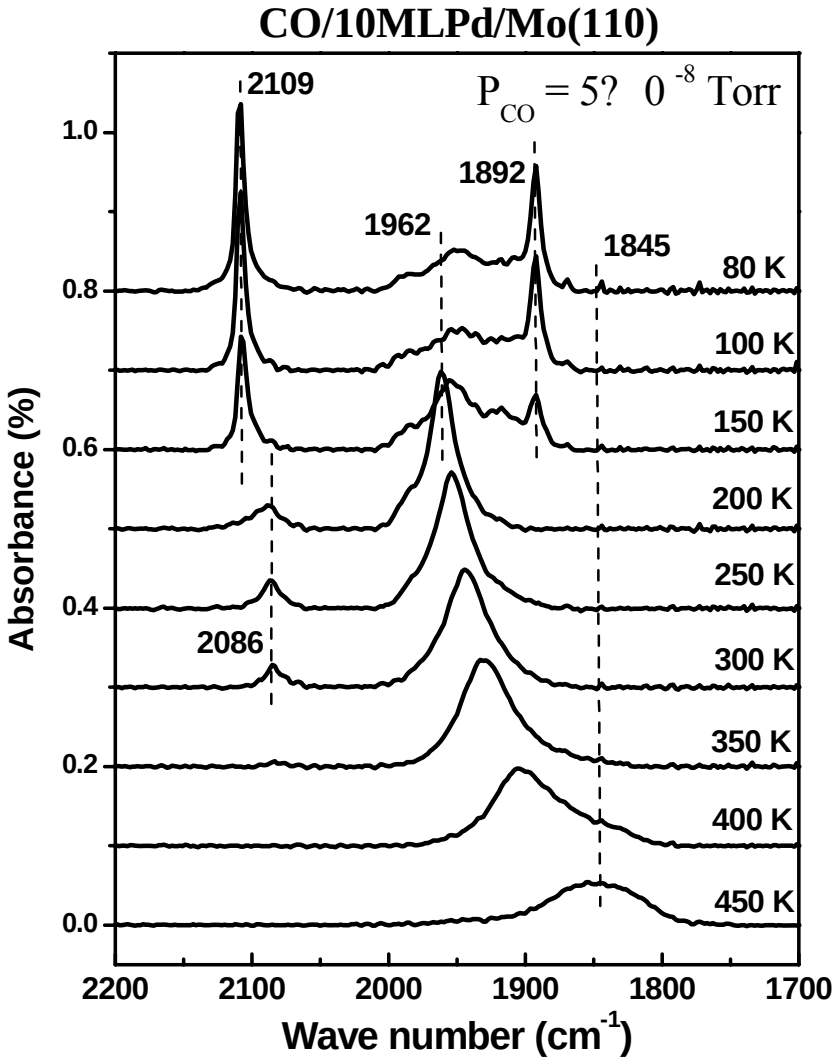

Fig. 36 IRAS spectra for CO adsorption on 10ML Pd/Mo(110) surface as a function of temperature**.**

atop sites.[39,43,123] Finally, it is noteworthy that weak features at ~1950 and ~1990 cm^{-1} still can be detected when CO saturates the surface at the liquid nitrogen (LN) temperature. Ideally CO only populates the Pd atop and 3-fold hollow sites at saturation coverage on a perfect Pd(111) surface.[39,43] However, similar features have been observed by Kuhn *et al.*[39] and Ozensoy *et al.*[123] in their CO ambient pressure studies on the Pd(111) single crystals. They interpreted these features as the CO adsorption on the Pd bridging sites due to a slight disorder in the (2×2)-3CO phase or the CO adsorption on the anti-phase domain boundaries.[123,124] It was also pointed out that the sample preparation conditions have a great impact on these features.[27,36,39,43] The less intensity in these features was detected when the sample surface was annealed in a higher CO background at a higher temperature.[125]

Except for this difference, the identical adsorption sites progression and frequencies in the studies of 10ML Pd film and Pd(111) single crystal clearly indicate that the 10 ML Pd film on Mo(110) mainly has the flat, (111) facets. More importantly, the same transition temperatures between the CO adsorption sites in these studies (specifically, 400K for 3-fold hollow sites to bridging sites and 150K for bridging sites to atop and 3-fold hollow sites) further assure us that the 10 ML Pd film has Pd bulk like properties. Very different CO adsorption properties have been reported by Xu and Goodman on the pseudomorphic Pd monolayer surface on Mo(110).[126] It was claimed that the CO binding energy on monolayer Pd film is reduced by 12 kcal/mol relative to Pd(111) surface, and in completely contrast to the Pd(111) surface, the atop sites have a higher CO binding energy compared to the bridging sites. These were attributed to a substantial

modification of electronic structure for the Pd monolayer by the Mo(110) substrate. Therefore, the similar CO adsorption behaviors on the 10 ML Pd film and the Pd(111) single crystal surface guarantee the 10 ML film is thick enough to eliminate the influence of Mo substrate.

The adsorption behavior of CO on the Au surface is relatively simple compared to the Pd surface mainly because of the weak interaction between Au and CO. Christmann and his coworkers estimated a maximum CO coverage of 0.3 ML at the LN temperature by their TPD experiments on a Au(110)-(1×2) surface.[35] The vibrational studies from a variety of Au systems at both UHV and ambient conditions showed only one CO stretching feature at around 2110~2120 cm^{-1}, and it was assigned to CO adsorption on Au atop sites.[38,42,127-129] But different with the Pd system, this feature red-shifts by increasing the CO surface coverage. This abnormal shift has been found valid for all the Group IB metals and becomes a characteristic for the Au surfaces.

Fig. 37 displays a series of IRAS spectra for CO adsorption on 10 ML Au film on Mo(110) surface at the indicated exposures and temperatures. At the low coverage limit, the CO absorbance is a single feature at 2116 cm^{-1}. As the exposure is increased, this feature red-shifts continuously to 2108 cm^{-1} at saturation, in close agreement with early IRAS results on Au(110)-(1×2) and 8ML Au film/Mo(112) surfaces.[127,128] The warming-up experiments show that the CO desorbs completely from the surface between 170 and 190 K, also in line with Christmann's TPD on Au(110) surface.[35] Again, these bulk Au-like CO adsorption behavior on 10 ML Au film/Mo(110) suggests we can use this system as a benchmark for the bulk Au(111) surface.

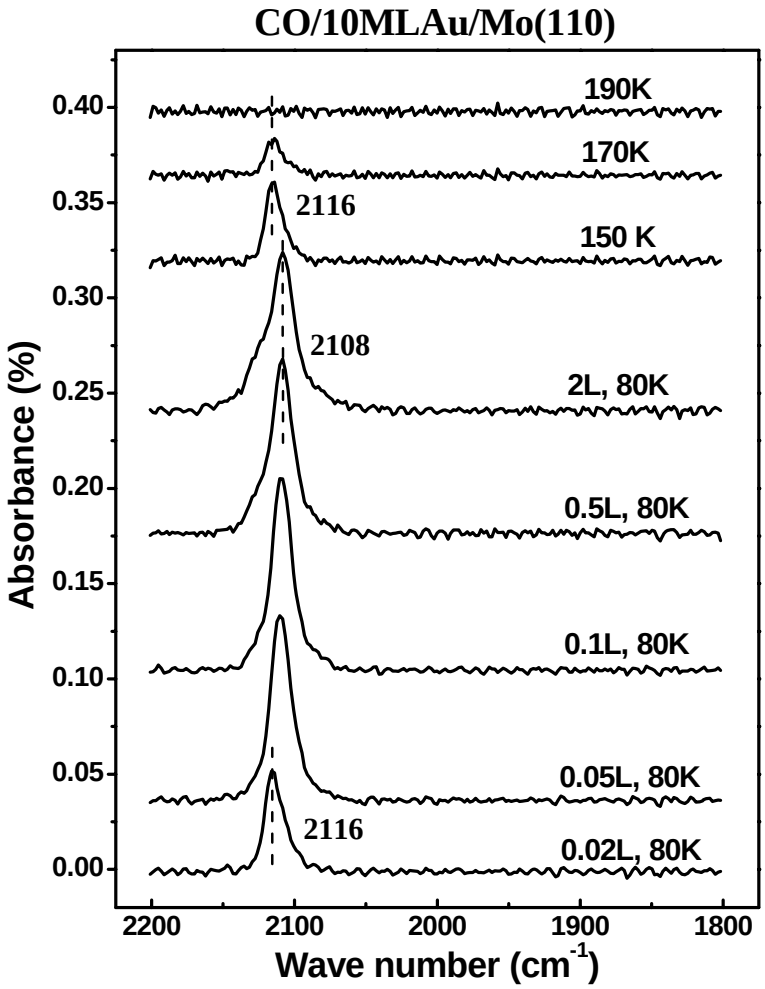

Fig. 37 IRAS spectra for CO adsorption on 10ML Au/Mo(110) surface at the indicated exposures and temperatures.

Fig. 38 and Fig. 39 illustrate the coverage (a) and temperature (b) dependent CO-IRAS spectra for the 5ML Pd/5ML Au/Mo(110) alloy system (Au deposited first) annealed at different temperatures. Note that the coverage dependent spectra were acquired by increasing the CO exposure at a sample temperature of 80 K and the temperature dependent spectra were collected by warming up the sample to the indicated temperature in the vacuum. In Fig. 38, the alloy film was first annealed at 600 K for 30 minutes prior to the CO adsorption. Within the low CO dosage regime (< 0.1 L), three apparent features, at about 2103, 2078 and 1940 cm^{-1}, intensify simultaneously (Fig. 38a). All these bands show no frequency shift with further CO exposure. When CO saturates the surface, the IRAS spectrum is dominated by the peak at 2078 cm^{-1} and the shoulder at 2103 cm^{-1}. These frequencies are typical for linearly bound CO on metal surfaces. According to the temperature dependent spectra (Fig. 38b), the shoulder at 2103cm^{-1} disappears at a lower temperature (between 150 and 200 K), indicating a weaker CO adsorbate species. Hence, this shoulder can be attributed to CO residence on Au atop sites. It is noteworthy that the Au-related feature is already visible in these spectra, because Au was covered by 5ML Pd during the film preparation. This may imply that the Pd and Au already intermix extensively after 600 K annealing. The consistent conclusion has been achieved by Shih HD *et al.* for the same system using AES and LEED techniques.[117] They claimed the surface alloying between Pd and Au occurs at room temperature and massive alloying sets in at 550 K. A broad band at 1940 cm^{-1} is also evident at CO saturation coverage. This band can be assigned to CO

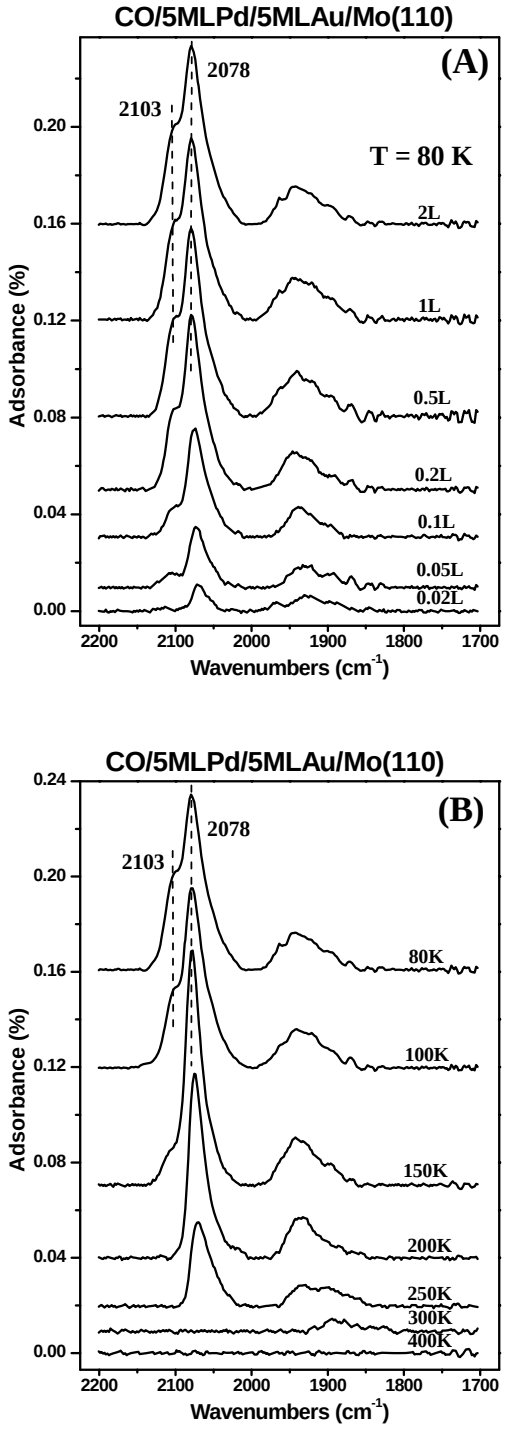

Fig. 38 Coverage (a) and temperature (b) dependent IRAS spectra for CO adsorption on 5ML Pd/5ML Au/Mo(110) system. The alloy film was annealed at 600 K for 30 minutes.

population on the Pd 2-fold bridge and 3-fold hollow sites. Both the Pd related features (atop feature at 2078 cm^{-1} and many-fold feature at 1940 cm^{-1}) are found to be much broader than those in the corresponding Pd single crystal system, suggesting the CO adsorption sites on this alloy surface are not well ordered. The absolute IR intensities in these spectra are also largely attenuated in comparison with the single crystal cases, implying many CO molecules may adsorb on this alloy surface with different tilt angles. Furthermore, both the asymmetrical peak shape (a low frequency tail) and the simultaneous growth of three features at the low CO coverage denote the limited CO mobility on this surface.[37] All these observations possibly lead to the conclusion that the alloy surface is still quite rough at this stage after 600 K annealing.

The same alloy film was further annealed at 800 K for 45 minutes to obtain the IRAS measurements shown in Fig. 39. Some substantial changes were found in the spectra. The broad peak observed at 1940 cm^{-1} in the previous experiment completely disappears at any CO coverage, and only a single feature at 2088 cm^{-1} appears following a low CO exposure (Fig. 39a). With the additional CO dosage, the second peak emerges at 2112 cm^{-1}, which can be assigned to CO adsorption on Au atop sites based on the thermal behavior of this peak (Fig. 39b). Also, this feature is well-resolved from the 2088 cm^{-1} peak. In fact, the full width at half maximum (FWHM) of the Pd atop feature at 2088 cm^{-1} is determined to be 7 cm^{-1}, comparable with that from a perfect Pd single crystal surface. Moreover, the IR intensities are greatly enhanced. It may be inferred that the alloy surface is smoothed and well ordered after 800 K annealing. The thermal annealing induced alloy surface morphology change has been reported in numerous early

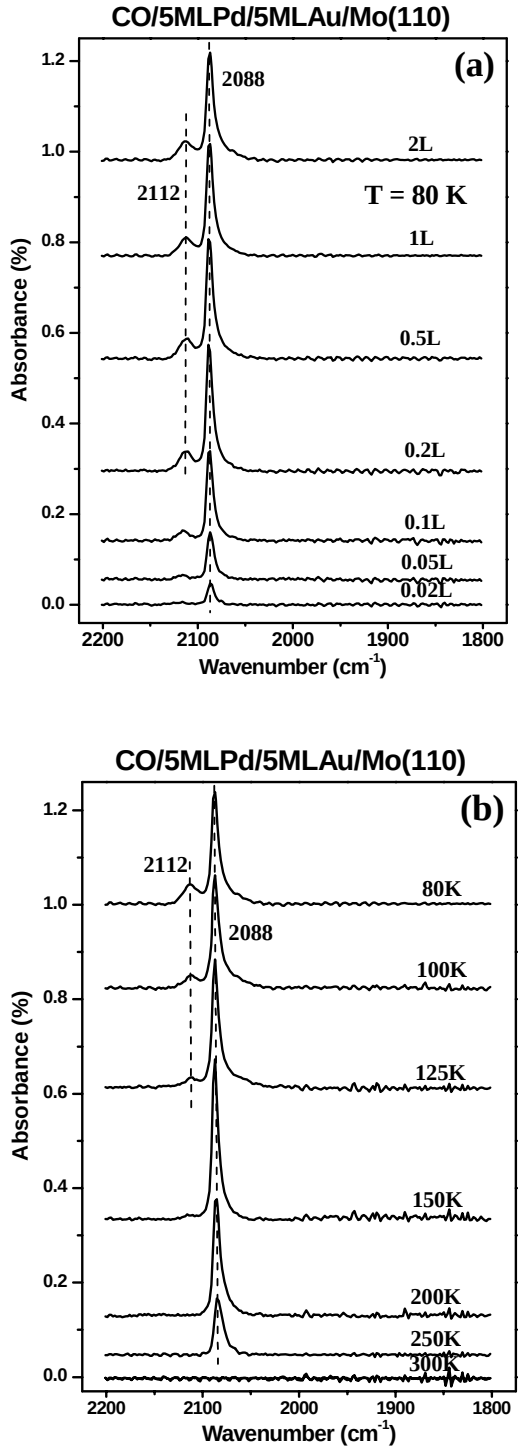

Fig. 39 Coverage (a) and temperature (b) dependent IRAS spectra for CO adsorption on 5ML Pd/5ML Au/Mo(110) system. The alloy film was annealed at 800 K for 45 minutes.

studies. For instance, Behm and his co-workers carried out a scanning tunneling microscopy (STM) study on the Au/Pd(111) alloy system, and it was found that a flat step-terrace alloy surface with no islands on the terraces can only be obtained after a 925 K annealing.[24] Lambert's group studied the reverse system (Pd/Au(111)) also using STM and observed that the 550 K annealing restores the roughened, concurrently grown, Pd overlayer to an atomically flat alloy surface.[22] The similar trend has also been observed in the Pd-Cu alloy systems.[130,131] Therefore, the substantial differences in our IR spectra upon different annealing temperatures can be well rationalized by the morphology changes in this process. It is interesting to note that the alloying (intermixing) process actually occurs at a lower temperature than the surface flattening.

It should be also mentioned that our CO vibrational frequency assignments are consistent with the previous high resolution electron energy loss spectroscopy (HREELS) studies. Sellidj A and Koel BE investigated the Pd/Au(111) alloy system and reported two energy losses at 1910 and 2090 cm^{-1} at saturation CO coverage, which were attributed to CO residence on the Pd two-fold bridge and atop sites.[116] Behm's group studied the inverted system (Au/Pd(111)) and observed the energy losses at 237-240, 258 and 263 meV (1920-1944, 2090 and 2130 cm^{-1}). They assigned these losses to CO adsorption on the small Pd patches, Au-coordinated Pd atoms, and Au atop sites.[24,26] However, due to the relatively low resolution of HREELS, it is difficult to differentiate the features among the Au atop sites, Pd atop sites, and Au-coordinated Pd sites. Thus, a systematic investigation of the frequency shift induced by the ligand (electronic) effect has not been made so far.

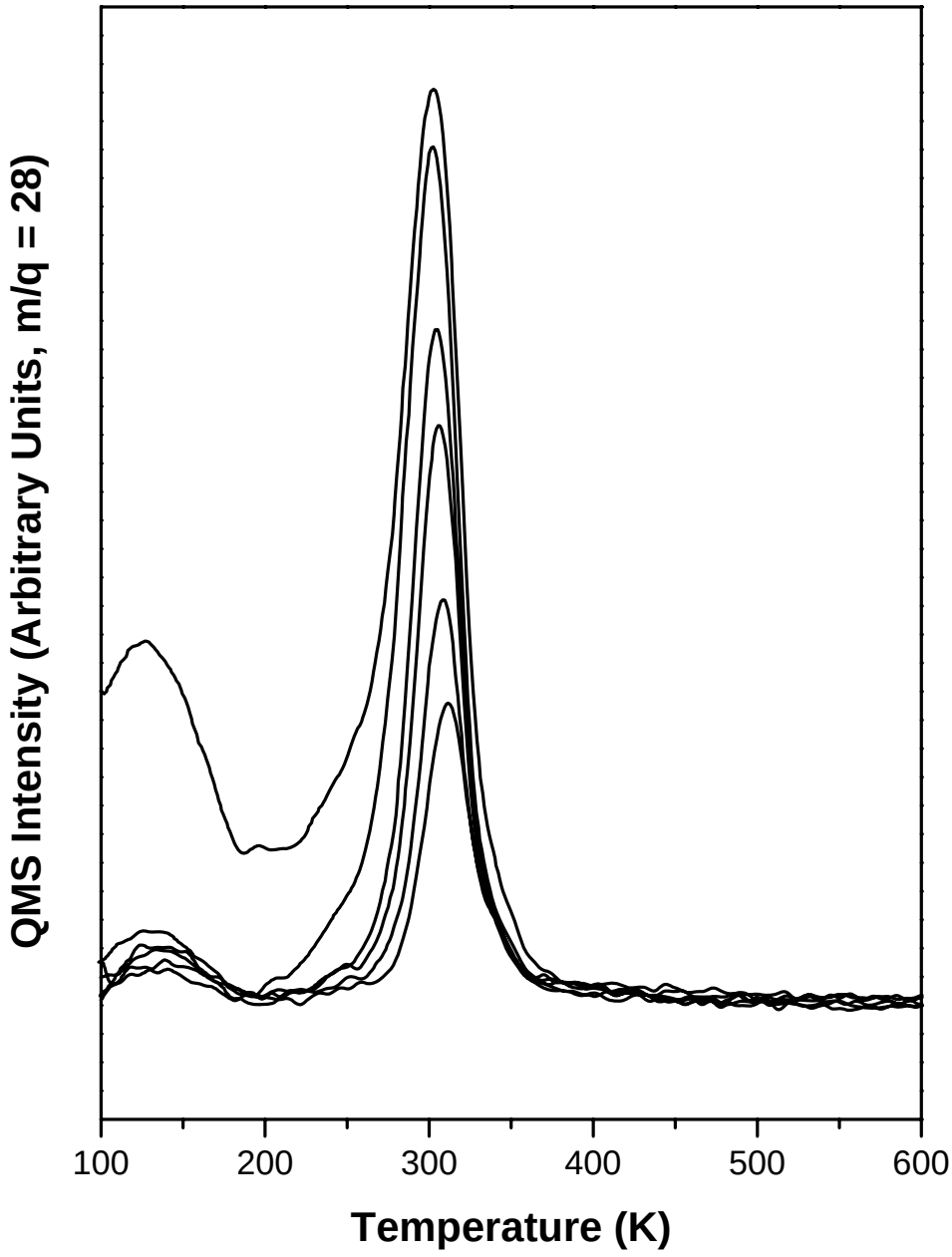

Fig. 40 TPD of CO on 5ML Pd/5ML Au/Mo(110) annealed at 800 K for 20 minutes (0.01~ 0.5 L of CO).

The combination of CO TPD and IRAS allow characterization of the available chemisorption sites and an estimation of their variation with surface concentration. Fig. 40 shows a series of CO TPD from 5ML Pd/5ML Au alloy system, annealed at 800 K for 20 minutes, and then exposed to CO at 90 K. From the LEISS analysis, the surface concentration of this surface is 18 and 82 atomic percent of Pd and Au, respectively. With a small amount of CO (< 0.20 L), the main desorption feature appears at ~ 300 K. With further CO exposure (0.50 L), this desorption feature is saturated and shifts to 295 K, and a new feature appears at 125 K. These two desorption features at 125 and 295 K are assigned to CO desorption from Au and Pd a-top sites, respectively. For Pd(111), the peak desorption temperature maximum for CO is ~450 K and is assigned to the desorption of multi-fold CO.[36] Our TPD results show no desorption feature of CO above 350 K. These TPD results clearly show that there are no multi-fold adsorption sites for CO and that CO occupies atop Pd and Au sites. These TPD results are consistent with our IRAS data which show no multi-fold CO vibrational feature. Previously, Baddeley *et al.*[132] reported a 2100 cm^{-1} loss and a 300 K TPD feature, assigned to CO on Pd singleton sites, and a 1930 cm^{-1} feature and a 445 K TPD feature, associated with 3-fold sites for annealed Au/Pd(111). Therefore, we conclude that the 125 K TPD feature and the 2112 cm^{-1} IR peak can be reasonably assigned to linearly bound CO on Au sites, and the 295 K peak and 2087 cm^{-1} feature, to linearly bound CO on singleton Pd sites surrounded by six gold atoms.

Ensemble and Ligand Effects

The term 'alloying effect' refers to the promotion of the catalytic properties when adding a second metal component to a single metal catalyst, and it is often explained on the basis of ensemble (geometric) and ligand (electronic) effects. The ensemble effect is normally used to describe the formation of a special arrangement of several reactive metal atoms, which makes the desired chemisorption bonds more likely. The ligand effect usually corresponds to the electronic modifications resulting from the heteronuclear metal-metal bonds, which affect the chemisorption bonding between the reactive metal atom and an adsorbate in the needed way. IRAS using CO as a probe molecule has been illustrated to be an effective technique for investigating the alloying effects.[32,34] In particular, the appearances (disappearances) of the characteristic CO stretches can be used to monitor the available adsorption sites on the surface, potentially providing the insight of the ensemble effect. The CO vibrational frequency shift can be used to identify the changes in the interactions between the substrate and CO molecules, which will reflect the electronic modifications of the substrate surface induced by the second metal (the ligand effect).

In Fig. 41, IRAS spectra for 10 ML Pd film, 5 ML Pd/5ML Au alloy film (annealed at 800K) and 10 ML Au film at saturation CO coverage of 80 K are compared. It is apparent that the Pd many-fold features (two-fold bridge and three-fold hollow features) are completely missing on the alloy surface, suggesting the Pd atop sites are the only accessible adsorption sites on the 5ML Pd/5ML Au alloy surface. As the stronger

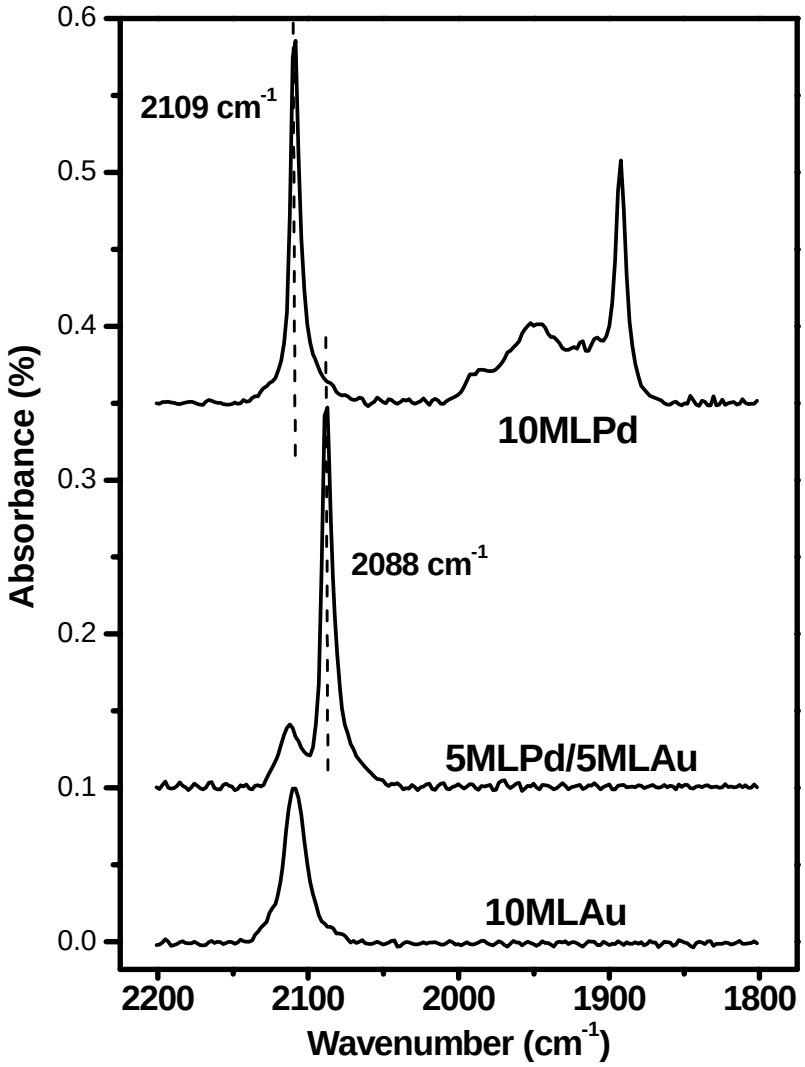

Fig. 41 Comparison of IRAS spectra for CO adsorption on 10 ML Pd film, 5ML Pd/5ML Au alloy film and 10 ML Au film on Mo(110) at saturation CO coverage. The alloy film was annealed at 800 K for 45 minutes, and the spectra were acquired at 80 K.

bonding sites, the Pd many fold features have been observed in any type of Pd single crystal and oxide-supported Pd cluster surface.[37,41] Hence, their disappearances must indicate the absence of connected Pd atoms on the surface. In other words, the surface Pd atoms must be isolated from each other to form a singleton species. This result can be well-explained and understood by combining with some early studies. Sadigh *et al.* obtained the atomic STM images for Pd-Au monolayer film on Ru(0001), and demonstrated the presence of pronounced chemical short range order (SRO) in the Pd-Au surface alloy (i.e., a preference for different metal atoms as their nearest neighbors).[28] The ISS studies for the 5ML Pd/5ML Au/Mo(110) alloy system showed the surface Pd concentration is only 18 % upon the annealing at 800 K for 20 minutes. Therefore, both the preferential surface segregation of Au and the chemical SRO make the density of larger Pd ensembles (e.g., Pd dimers, Pd trimers and Pd patches, etc.) very low on the alloy surface. Consequently, the most probable surface ensemble becomes the Pd monomer surrounded by Au atoms. Behm RJ and his co-workers recently reported the formation of similar Pd ensembles on the Pd/Au(111) surface synthesized using electrochemical methods.[32] Based on their IR and STM data, the critical surface ensemble for CO adsorption was identified as the Pd monomer. At the low surface Pd concentration (7 and 15 %), only an IR feature associated with linearly bound CO on the Pd monomer was observed. This feature increased in intensity up to 22 % surface Pd, while the bridge-bound CO features started to emerge.

Another difference to be easily noticed in Fig. 41 is the CO-IR intensity for the Au atop feature drops dramatically on the alloy surface. This is interesting if we recall from

our ISS study that the 5ML Pd/5ML Au alloy system has 82 % Au on the surface upon 800 K annealing. If we assume the same saturation CO coverage on Au surface in pure Au and alloy system, we should expect the IR intensity reduced only by about 20 %. However, a decrease of more than two-thirds is observed, which indicates the probability of CO adsorption on Au decreases substantially on the alloy surface. The preference of CO adsorption on one metal sites over the other in bimetal alloy systems has been observed before.[133-135] For instance, Varga's group studied the PtCo alloy system with STM, where CO was found to adsorb exclusively on top of Pt sites and never on Co.[134] Also, the IRAS study from Rutten *et al.* suggests that CO adsorption at atop rhodium sites was preferred over platinum atop sites on a $Pt_{0.25}Rh_{0.75}$ single crystal surface, even though the CO adsorption heats for Pt(111) and Rh(111) surfaces are very close. It is reasonable to assume that the similar situation could also occur in the PdAu alloy system. Namely, the possibility of CO adsorption on the isolated Pd sites is primarily enhanced while that on the rest Au surface is diminished.[135]

The last difference remains to be explained in Fig. 41 is the CO frequency shift for the atop Pd feature, which moves from 2109 cm^{-1} on the pure Pd film to 2088 cm^{-1} on the alloy surface. This shift has been ascribed to the influence of the ligand effect.[34] Since the frequency shift is largely affected by the chemical interaction between the substrate and CO (mainly the backdonation of electrons from the metal d band to CO $2\pi^*$ antibonding orbital), the addition of Au to Pd surface alters the width and center of Pd d band, and thus shifts the CO internal frequency.[37] Qualitatively, a linear relationship between CO stretching frequency and $2\pi^*$ occupation was considered to be

applicable for the case of CO on Pd.[37] Consequently, a continuous shift of the CO stretching frequency would be expected when the surface Pd concentration was varied by changing the bulk Pd to Au ratios. However, no frequency shift is observed in the corresponding experiments, suggesting this conclusion may be implausible (see Page 108-(A)). Most likely, the other frequency shift determining factor, the vibrational coupling (or the dipole-dipole coupling), plays a more important role in this case. As mentioned earlier, a weak feature at 2086 cm^{-1} has been observed on both 10 ML Pd film and Pd(111) single crystal surfaces. The frequency of this feature closely resembles that of the isolated Pd sites, which possibly implies they stem from similar chemical environments (see Fig. 42). If this is true, the frequency shift on pure Pd surfaces to 2109 cm^{-1} at saturation CO coverage could be easily explained by the coverage dependent frequency shift. At the low CO coverage on Pd(111) facets, three-fold hollow and two-fold bridge sites are the more energy favorable adsorption sites; the minor feature for Pd atop sites appears only because of the surface disorder. At this stage, the CO intermolecular distance is relatively large, so the repulsive interaction between CO molecules is neglectable (see Fig. 42). However, when CO coverage increases to higher than 0.5 ML, the condensed but ordered (2×2) structure forms. The CO molecules become so close to each other that the repulsion force becomes dominant and shifts the frequencies of both the three-fold hollow and atop features to higher values (see Fig. 42). Both these shifts are made in one step (from 2086 to 2109 cm^{-1} for Pd atop sites, from 1845 to 1892 cm^{-1} for Pd three-fold hollow sites, see Fig. 42 and Fig. 36), paralleling closely with the CO overlayer structure change, and no intermedium frequency has been

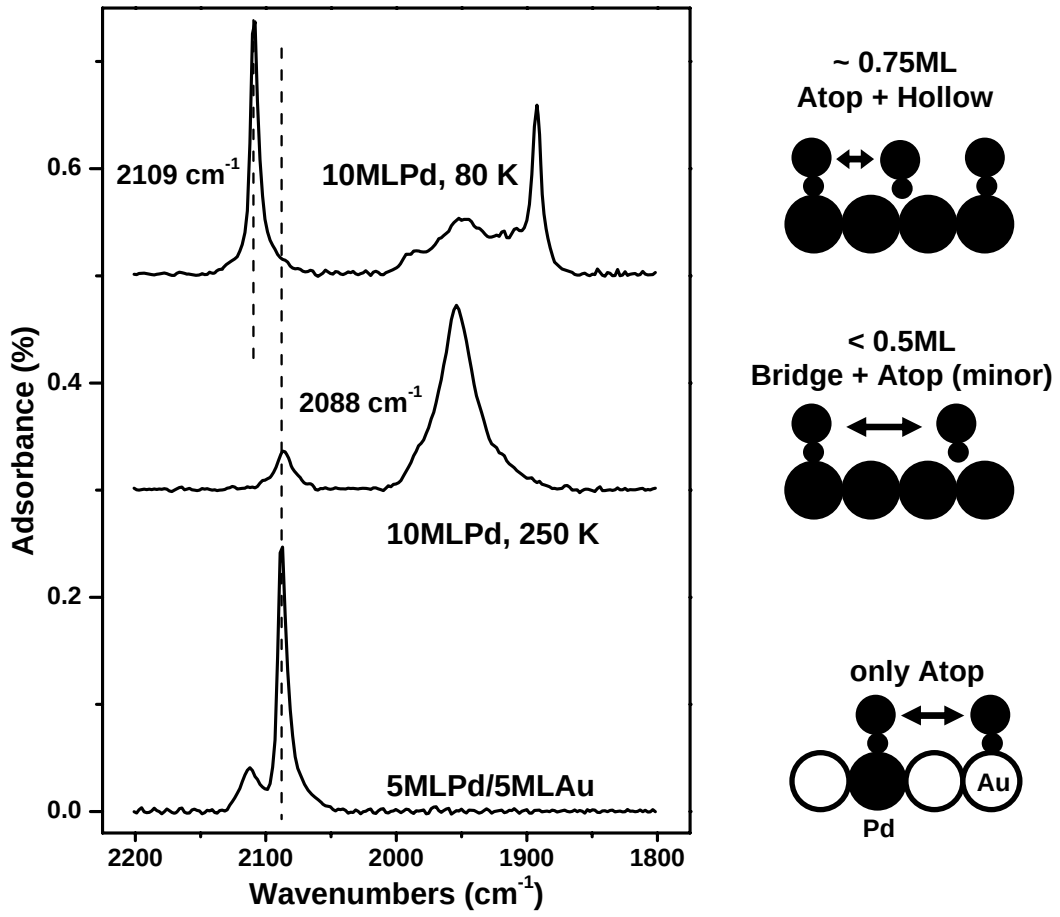

Fig. 42 IRAS spectra for CO adsorption on 10ML Pd film and 5ML Pd/5ML Au alloy film on Mo(110). The top and middle spectra were collected in 5×10^{-8} Torr CO background at the indicated temperatures. The bottom spectrum corresponds to the saturation CO coverage at 80 K. The right hand schematics represent the side views of CO adsorption models on the respective surfaces.

observed. All these further support our argument that the frequency shift is caused primarily by the dipole-dipole coupling, not by the chemical interaction through the substrate. As mentioned above, the CO adsorption probability on Au is greatly reduced on the alloy surface. Most probably, the Au atoms, which surround the isolated Pd sites, are not likely to adsorb any CO. Therefore, the dipole-dipole coupling effect may not be so significant on the alloy surface either. Hence, the frequency of the isolated Pd feature is not blue-shifted. An interesting question to be asked then is why the CO frequency for atop sites is so insensitive to the chemical interaction between substrate and CO. One reason might be that the cross-section between CO $2\pi^*$ orbital and the metal d band is too small for the linear configuration. But further experimental and theoretical work is certainly needed to obtain a better overview of this issue, which will be tremendously important for understanding the metal selectivity in catalytic reactions.

Alloy Film as a Model Catalyst System

The lattice matched alloy films grown on a refractory metal substrate can be used as a model alloy system for further surface science and catalytic studies. The characterization results for total 10 ML thick Pd-Au alloy films on Mo(110) have been shown to closely resemble the previous study on the polycrystalline bulk Pd-Au alloys. In order to complement this work and further confirm the efficiency of this thin film methodology, CO-IRAS experiments for the Pd-Au alloy films annealed to the different temperatures and with different Pd to Au ratios have been carried out.

Fig. 43 displays CO-IRAS spectra for (a) 7.5 ML Pd/2.5 ML Au and (b) 2.5 ML

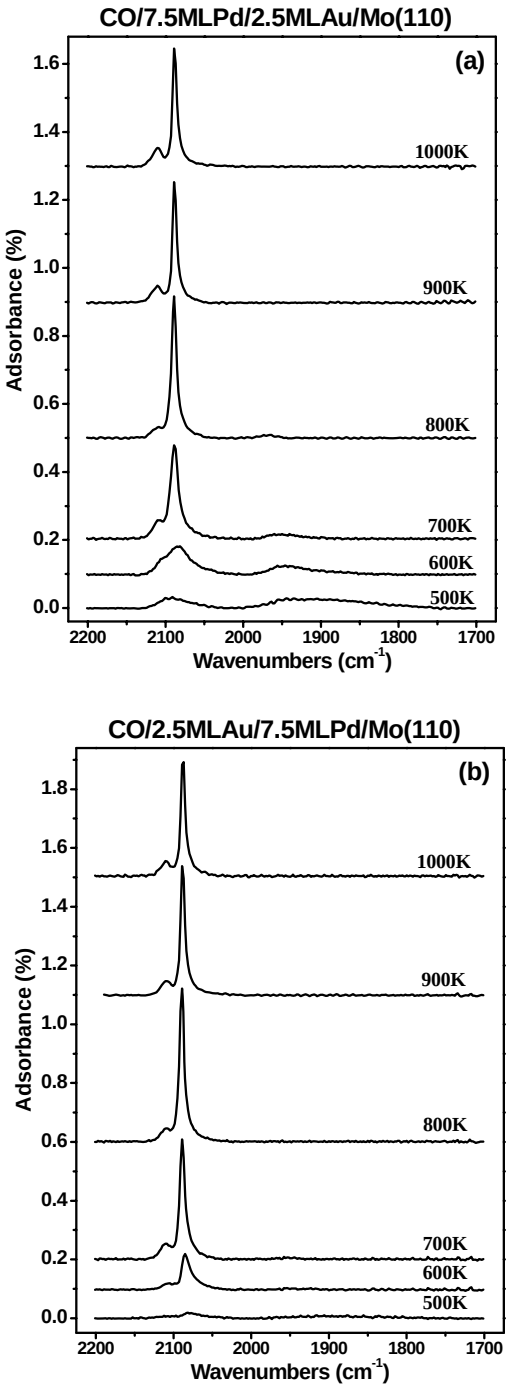

Fig. 43 IRAS spectra for saturation CO on (a) 7.5ML Pd/2.5ML Au/Mo(110) and (b) 2.5ML Au/7.5ML Pd/Mo(110) alloy films as a function of the sample annealing temperature. The sample was annealed for 20 minutes at each temperature, and the spectra were acquired at 80 K.

Au/7.5ML Pd alloy films on Mo(110) with different annealing temperatures. The alloy films were annealed at each temperature for 20 minutes, and all the spectra were acquired at 80 K with saturation CO coverage. This data presents us with a good overview of IR spectra variations as a function of annealing temperature for the same alloy composition but with different deposition orders. In both cases, small IR intensities and broad IR features have been observed after low temperature annealing (500 K and 600 K), similar with what we have discussed in the above section for 5ML Pd/5ML Au case. But clear differences can be seen between them, with IR spectra mainly showing the characteristic features from the second-deposited metal. After 700 K annealing, the IR intensity starts to pick up and the isolated Pd peak becomes the most dominant feature. The IR intensity saturates after 800 K annealing, but the IR features are not well resolved until an even higher annealing temperature (900 K and 1000 K). Apparently, the same stable alloy films are formed between 800 and 1000 K annealing regardless of the different deposition sequences. ISS results showed that the surface compositions of 5 ML Au/5 ML Pd alloy films on Mo(110) remain constant as $Au_{0.8}Pd_{0.2}$ between 700 and 1000 K annealing independent of the metal deposition order. Therefore, based on these ISS and IRAS experiments, it is evident that a thermodynamic equilibrium can be reached after annealing the PdAu alloy films to high enough temperature. Once reaching the equilibrium, ISS results suggest Au preferentially enriches the alloy surface, and IRAS data indicate a well-ordered surface morphology (most likely flat) with the most common adsorption sites as the isolated Pd.

As shown above, LEISS is a preferred technique for accessing the surface composition, but this technique is relatively insensitive to the surface morphology. On the other hand, IRAS using CO as a probe molecule provides the detailed information about the surface morphology and adsorption sites, but its application in quantitative analysis is limited. So, in literature, there has been a long-time exploitation of using IRAS of CO adsorption to 'titrate' the binary alloy surface composition. For instance, Varga's group compared the alloy surface concentrations obtained from ISS and HREELS of CO adsorption results for the $Pt_{25}Ni_{75}(111)$ single crystal system. They found HREELS is not generally appropriate for determining the surface composition to high accuracy. Though under some favorable conditions (well annealed over 1000 K, with comparably small number of surface defects) the results from both methods were nicely within the corresponding error bars.[136-139] We can also examine this possibility in PdAu alloy system by combining our IRAS of CO adsorption and ISS results. Fig. 44 (A) summarizes CO-IRAS spectra for different Pd to Au bulk ratios, provided all the alloy films were annealed at 800 K for 30 minutes prior to the saturation CO adsorption at 80 K. The corresponding surface Pd concentration from ISS results is listed along with the bulk ratio for each spectrum (a-d) in the figure. Clearly, 800 K is not high enough for the 9 ML Pd/1 ML Au alloy film (d) to obtain an ordered morphology. The isolated Pd feature on this surface is so broad that the Au atop peak cannot be resolved from it. Also the Pd many fold features are observed as ISS shows the Pd is rich on this surface (60%). However, for 1:3, 1:1, and 3:1 Pd-Au mixtures (a-c), 800 K annealing does result in well-ordered surfaces with the isolated Pd as the main

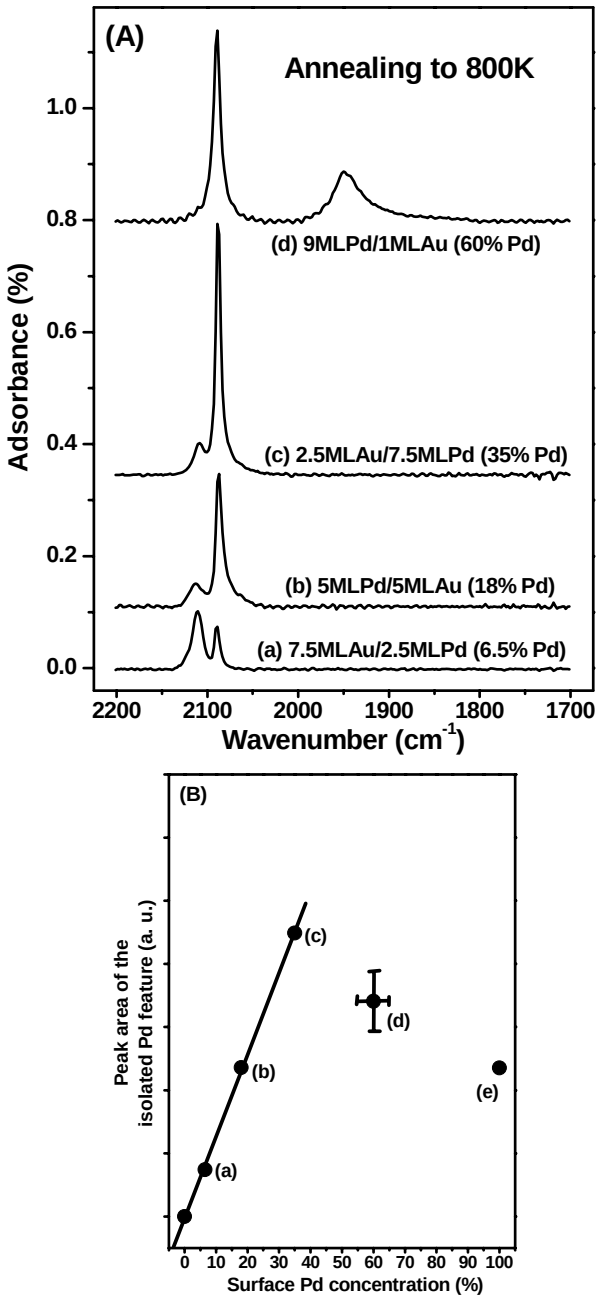

Fig. 44 (A) CO-IRAS spectra for alloy films with different Pd to Au ratios. All the alloy films were annealed at 800K for 30 minutes, and the spectra were acquired at 80 K with saturation CO coverage. (B) The peak area for the isolated Pd feature as a function of the surface Pd concentration obtained from Ref. 103. Point (e) corresponds to the peak area of the CO Pd atop feature on 10ML Pd film.

adsorption sites. The intensity of the isolated Pd feature grows as the Pd bulk content increases, indicating the concentration of the isolated Pd atoms can be systematically controlled by altering the bulk Pd to Au ratios. In fig. 44 (B), the peak areas of the isolated Pd feature were plotted as a function of the surface Pd concentration obtained from ISS results. (Point (e) refers to the peak area of the CO Pd atop feature for 10 ML Pd film.) Apparently, an excellent linear relationship is exhibited for the low surface Pd concentration up to 35 % (a-c), demonstrating that CO-IRAS can be used to estimate the isolated Pd concentration accurately within the low Pd concentration regime. As the most important adsorption sites on the alloy surface, the isolated Pd might play critical roles in many catalytic reactions. The success in using CO-IRAS to titrate the isolated Pd could be pivotal for building up the structure-reactivity relationships. The IR intensity falls off the linearity when Pd is rich on the surface (d-e), probably because the vibrational coupling effect attenuates IR intensity at high surface CO coverage. Pfnur H *et al.* reported that a linear relationship between coverage and integrated absorption intensity exists only below θ_{CO} = 0.33 ML for CO adsorption on Ru(001) surface. IR intensity drops, thereafter, with the result that at the saturation coverage the adsorption per adsorbed molecule is only 35-40 % of the adsorption at θ_{CO} = 0.33 ML. They ascribed this effect to the strong lateral interaction in the CO adlayer.[140] The excellent correlation here possibly is another proof that CO molecules are not adsorbed on the Au atoms which surround the isolated Pd. Hence, the dipole-dipole coupling effect can be overlooked in this case as previously discussed. It should be mentioned that this linear relationship could be applicable for other bimetal alloy systems, as long as the

requirements of well-ordered morphology and the absence of vibrational coupling are fulfilled.

In conclusion, the composition, electronic properties, and structure of Pd-Au alloy surfaces were determined by LEISS, XPS, IRAS and TPD. Preferential surface segregation of Au in Pd-Au mixtures on Mo(110) was observed subsequent to an anneal. Au and Pd films on Mo(110) form stable surface alloys which have fixed surface compositions within the temperature range 700–1000 K. Upon annealing at 800 K, 1:1 Pd-Au alloy mixtures form a stable alloy with a composition of $Pd_{0.2}Au_{0.8}$, independent of the metal deposition sequence. From LEISS results for various Pd-Au mixtures on Mo(110), the surface versus bulk phase diagram shows significant enrichment of the surface in Au compared to the bulk. Alloying effects, including geometric ensemble effect and electronic ligand effect, have been addressed by comparing IR spectra with corresponding single component systems. A unique CO vibrational feature at 2088 cm^{-1} was identified as the CO adsorption on isolated Pd sites, indicating the presence of ensemble effect. On the other hand, no conclusive indications of electronic ligand effect were found in the CO stretching frequency. The surface concentration of this isolated Pd site can be controlled systematically by altering the bulk Pd-Au alloy composition, which allows the further studies of the properties of this isolated Pd site in catalytic reactions.

Pd–Au/SiO_2/Mo(110)*

The study of planar Pd–Au bimetallic alloy surfaces was extended to silica–supported Pd–Au bimetallic clusters in order to better represent the industrial technical catalysts. In literature, several aspects about oxide–supported Pd–Au catalysts have been addressed. The structural properties of silica supported Au-Pd catalysts prepared from colloid precursors were studied using X-ray diffraction (XRD), extended X-ray absorption fine structure (EXAFS), and X-ray absorption near–edge spectroscopy (XANES).[141-143] Davis, et al., concluded that Pd atoms decorate a core of Au atoms using EXAFS.[141] Utilizing similar techniques, Lamb, et al., also concluded that a partial monolayer of Pd atoms decorates a Au-rich core.[143] On the other hand, Kaszkur, et al.,[142] used XRD to show that a Pd-decorated surface induced by oxygen adsorption can be transformed to a Au-decorated surface with a pulse of H_2. Related infrared studies from our laboratories of CO adsorption on alumina supported Au-Pd and Cu-Pd clusters suggested that a geometrical rather than a ligand effect was dominant.[27] In this study, the cluster surface composition and structure are investigated systematically by LEIS, IRAS, and TPD with CO as a probe molecule.

---

* Reproduced in part with permission from: Luo, K.; Wei, T.; Yi, C.W.; Axnanda, S.; Goodman, D.W. *Journal of Physical Chemistry B* **2005**, 109, 23517, Copyright 2005 American Chemical Society.

Growth of Pd–Au Alloy Clusters

The growth and characterization of nano-sized clusters of Au and Pd on SiO_2 surfaces have been discussed in the literature.[94,144-147] In general, Pd clusters are more highly dispersed for a given coverage and are more sinter-resistant compared to Au.[145-147] In the present study, amorphous SiO_2 films were used to support Au-Pd clusters. The details of the SiO_2 films preparation have been described previously.[144] The SiO_2 films were characterized with AES and XPS, with the results showing that the SiO_2 films were fully oxidized (Fig. 45). The thickness of the SiO_2 films was estimated to be 2–5 nm using the attenuation of the Mo substrate signals and the known mean free paths of the Auger electrons. To synthesize the clusters, 1.0 ML Pd was first deposited on SiO_2 and then annealed to 800 K for 10 minutes. Subsequently, Au was deposited at 300 K, and annealed to 800 K for 10 minutes. LEIS was used to characterize the surface composition and morphology for each deposition condition with all spectra being collected with a substrate temperature of 300 K. The LEIS spectrum in Fig. 46 (a) is that following the deposition of 1.0 ML Pd on the SiO_2 film and a subsequent 800 K anneal. Three LEIS features with kinetic energy (KE) at 0.45, 0.70, and 0.97 keV are assigned to O, Si, and Pd, respectively. A Mo feature at 0.94 keV was not present, consistent with the Mo substrate being fully covered by the SiO_2 thin film. Upon deposition of 1.0 ML Au at 300 K, the intensity of the Pd feature dramatically decreases by ~ 65 %. Concomitantly, a large Au scattering feature appears at 1.03 keV. The significant decrease of the Pd feature upon deposition of Au indicates that a significant amount of the deposited Au decorates the Pd clusters. Upon annealing 1.0ML Au/1.0ML Pd/SiO_2

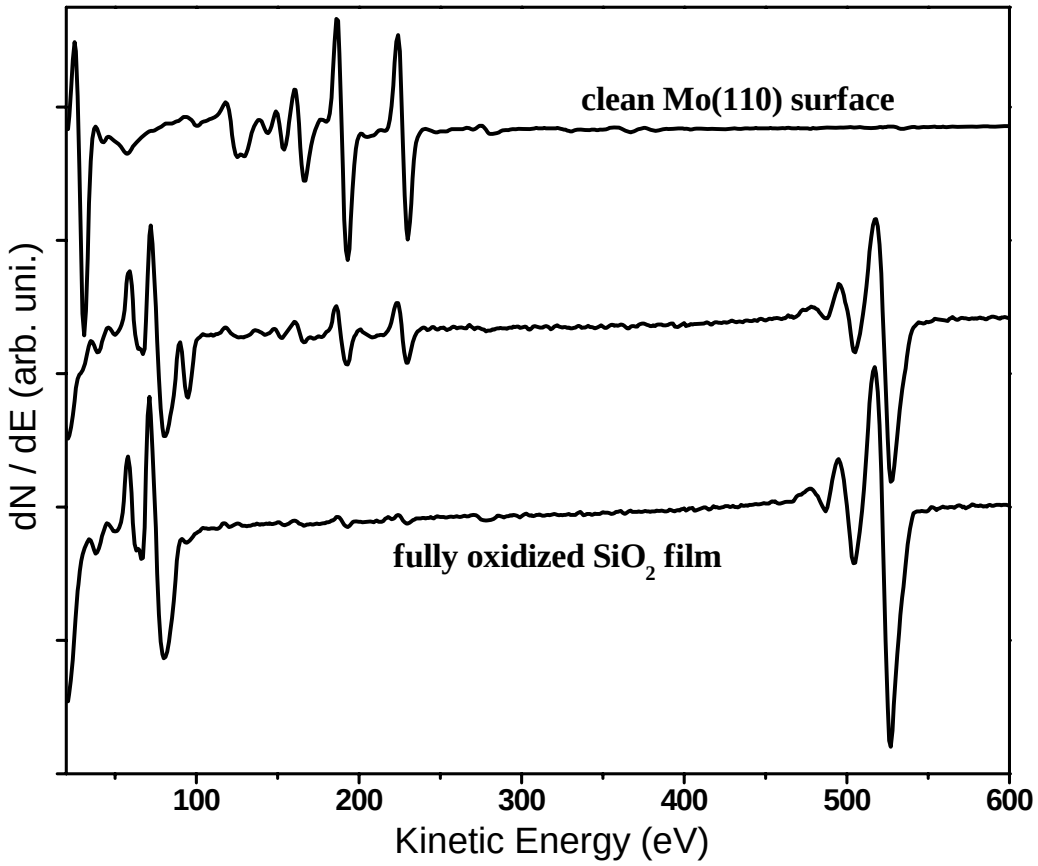

Fig. 45 AES spectra for clean Mo(110), partially, and fully oxidized SiO_2 surfaces.

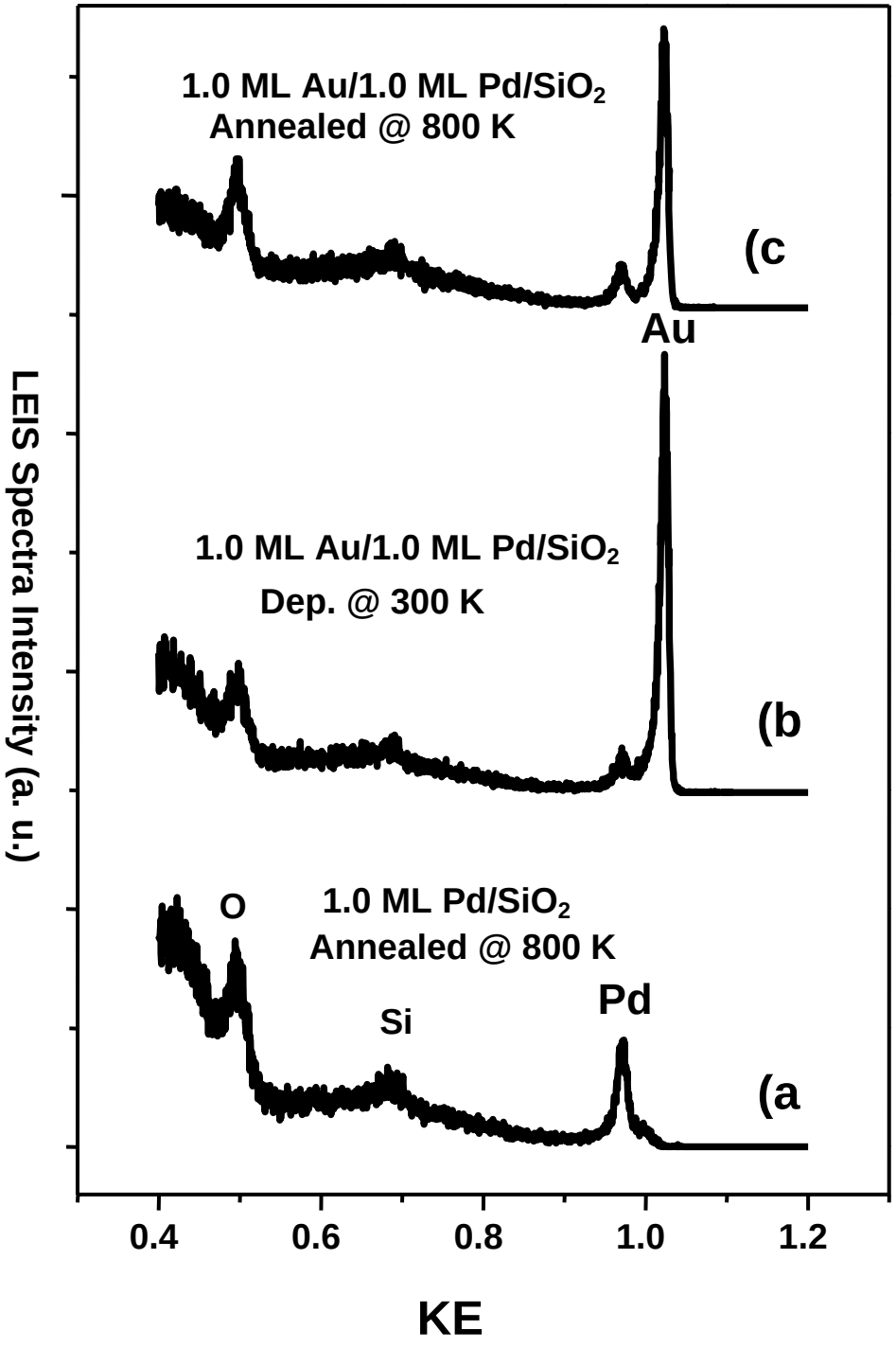

Fig. 46 LEIS spectra of (a) 1.0ML Pd/SiO_2 after an 800 K anneal; (b) after deposition of 1.0 ML Au deposition 300 K on 800 K pre-annealed 1.0ML Pd/SiO_2; and (c) 1.0ML Au/ 1.0ML Pd/SiO_2 annealed to 800 K. All spectra were collected at 300 K.

to 800 K, the Pd feature intensity remained essentially constant; however, the Au intensity decreased by ~ 30 %, likely due to alloying of the Au with Pd and/or sintering of Au-only clusters. Similar LEIS measurements were carried out by reversing the deposition sequence, i.e. 1.0ML Pd/1.0ML Au/SiO_2 (Au deposited first) (not shown here). The Au scattering intensity was unchanged following Pd deposition, likely because only a small fraction of the added Pd nucleates on the Au clusters with the remainder forming Pd-only clusters.[146,147] Based on data above, the deposition of Pd first is clearly preferable for the synthesis of more uniform Au-Pd alloy clusters.

LEIS Au-Pd scattering data for Au-Pd silica supported clusters, i.e., 1.0ML Au/1.0ML Pd/SiO_2, and a planar Au-Pd surface, i. e., 5.0ML Au/5.0ML Pd/Mo(110), are shown in Fig.47 as solid and dashed lines, respectively. Note that each of these was annealed to 800 K prior to acquisition of the LEIS spectrum at 300 K. The planar 5.0ML Au/5.0ML Pd/Mo(110) surface consists of ~ 20 % Pd and ~ 80 % Au. For 1.0ML Au/1.0ML Pd/SiO_2, the LEIS data show Pd to have a similar relative intensity compared to the extended Au-Pd surface spectrum. The Au LEIS spectral intensity for the Au-Pd clusters, however, is significantly less in Figure 47 compared to the Au LEIS signal for the extended Au-Pd surface, implying that the Au-Pd cluster surfaces are more Pd-rich compared to the corresponding Au-Pd extended surface. Normalization of the Pd LEIS intensity suggests that the cluster surface concentration consists of ~ 33 % Pd and ~ 67 % Au. We note also that XPS of supported Pd clusters on the silica films here after annealing to temperatures as high as 800 K indicated no silicide formation as previously reported for Pd growth on monolayer SiO_2.[145,146]

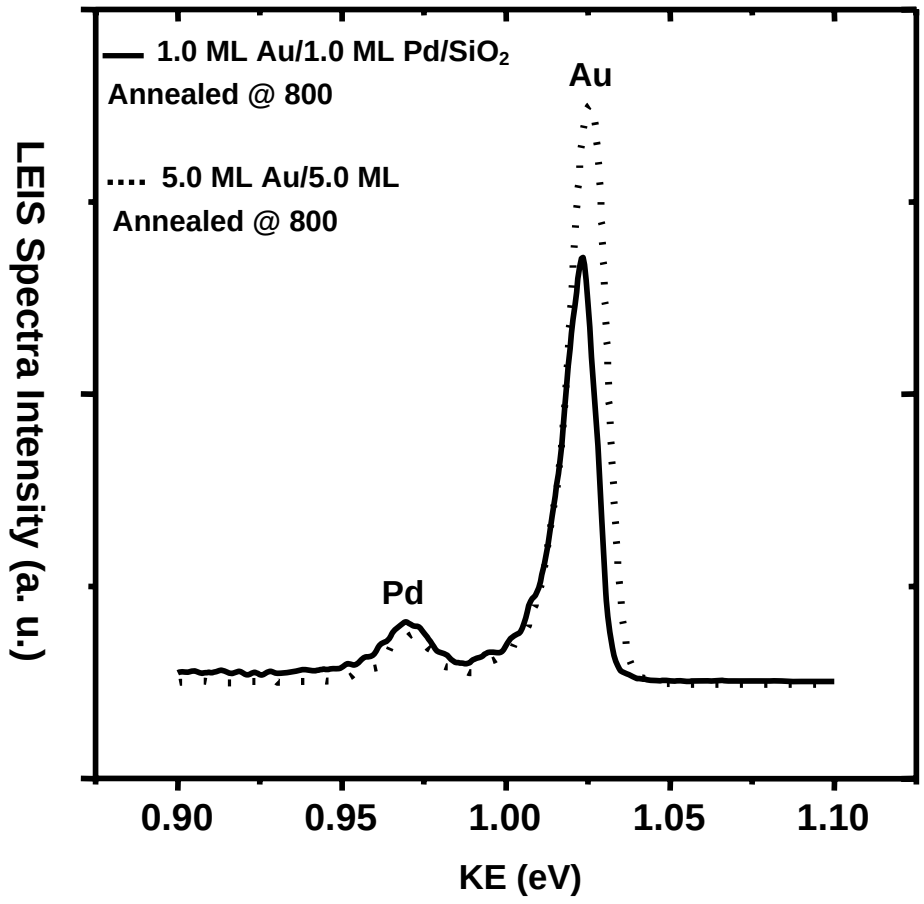

Fig. 47 LEIS data for 1.0ML Au/1.0ML Pd/SiO_2 after 800 K annealing (solid line) and 5.0 ML Au/5.0ML Pd/Mo(110) after 800 K annealing (dashed line). All spectra were collected at 300 K.

In studies of Au-Pd surface alloys on Mo(110) surface, CO TPD was used to distinguish isolated Pd sites from Pd bridging/three fold hollow sites. This same methodology was used now to study the silica supported Au-Pd clusters. TPD from a saturated coverage of CO (1.0 Langmuir, L) was carried out for the bare SiO_2 and SiO_2-supported Au-Pd clusters, each annealed to 800 K. In Fig. 48, CO TPD spectra for the bare SiO_2 surface, 1.0ML Pd/SiO_2, and 1.0ML Au/SiO_2 are shown in Fig. 48(a), 48(b), and 48(c), respectively. In Fig. 48(a) for CO on bare SiO_2, a single broad low temperature feature centered at 135 K was observed from CO adsorbed on the SiO_2 support. In spectrum 48(b) for CO/1.0ML Pd/SiO_2, additional features centered at 465, 320, and 250 K were observed. Based on previous studies of CO TPD on Pd low index single crystal surfaces and oxide supported clusters,[36,43,148-150] the 465 K feature is assigned to CO adsorbed on Pd three-fold hollow sites. The features at 250 and 320 K are likely due to CO adsorbed on a-top Pd sites at various Pd facets, e.g. Pd(100), Pd(111), corners/edges, etc. The desorption features between 320 and 465 K are assigned to CO on Pd bridging sites, in agreement with the studies of Carlsson, et al., of CO adsorption on Pd/Al_2O_3 surfaces.[148] Fig. 48(c) shows CO TPD from 1.0ML Au/SiO_2, with no strong desorption features apparent above 200 K, indicating weak CO bonding as reported previously.[147,151] In Fig. 48(d) and 48(e), CO TPD from 1.0ML Pd/1.0ML Au/SiO_2 and 1.0ML Au/1.0ML Pd/SiO_2 are shown, respectively. In Fig. 48(d), a slight decrease of CO desorption is apparent for all the features above 200 K, compared to Fig. 48(b) of CO/1.0 ML Pd/SiO_2. In comparison to spectrum 48(a), (b), and (c), an increase in intensity for the low temperature feature at 135 K was observed due to the additional

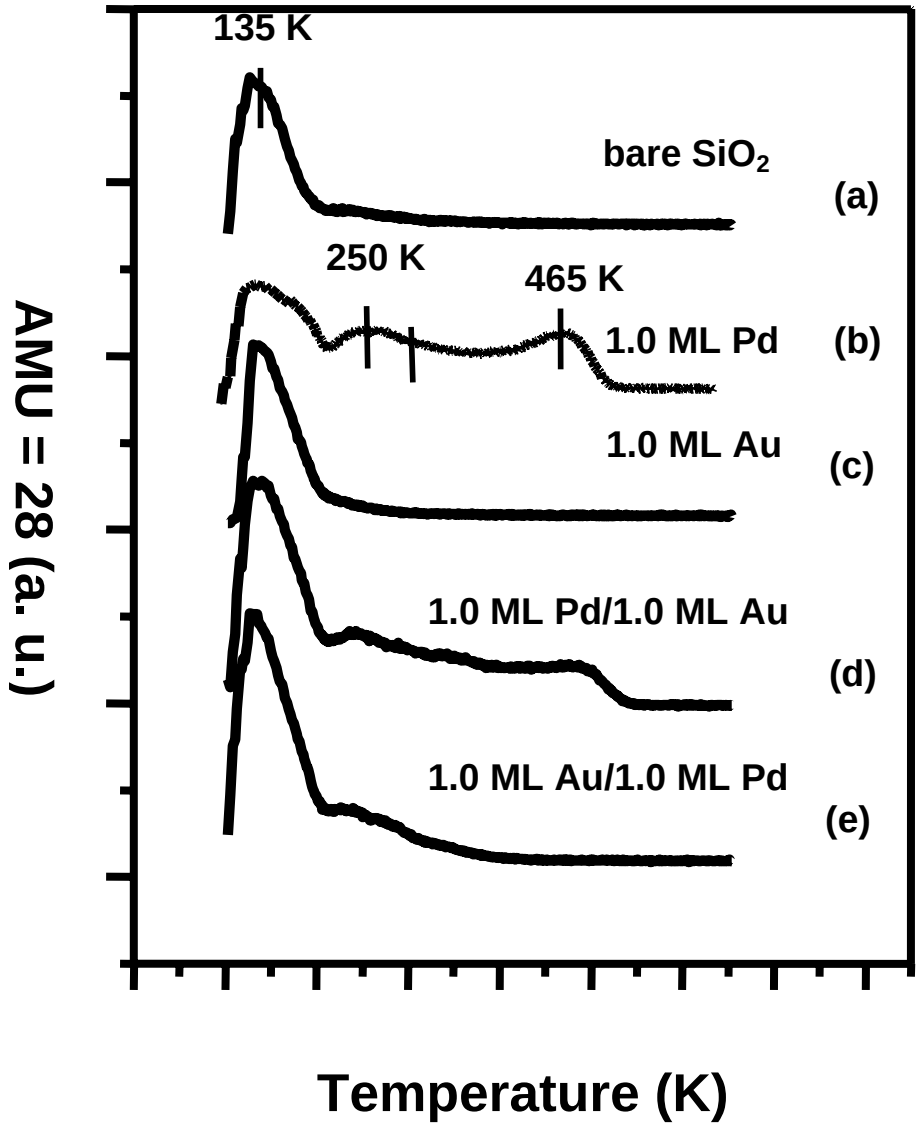

Fig. 48 TPD spectra of CO: (a) with 1.0 L CO exposure at 90 K on bare SiO_2; (b) 1.0ML Pd/ SiO_2; (c) 1.0ML Au/SiO_2 ; (d) 1.0ML Pd/1.0 MLAu/SiO_2; and (e) 1.0ML Au/1.0 ML Pd/SiO_2.

weakly bonded CO on Au. In this deposition sequence, the surface exhibits the primary CO desorption features associated with pure Pd clusters, i.e. 1.0ML Pd/SiO_2, and is consistent with the primary nucleation of Pd-only, rather than Au-Pd clusters. However, in spectrum 48(e), both the high temperature feature at 465 K and the features between 320 and 465 K completely disappear for 1.0ML Au/1.0ML Pd/SiO_2. The intensity of the a-top Pd sites at 250 and 320 K remains with ~ 30 % attenuation. These results are significantly different from those of Fig. 48(b), implying considerable alloying with Au deposition onto pre-deposited Pd clusters and a subsequent anneal.

Surface Adsorption Sites

LEIS, CO-TPD, and CO-IRAS were combined to characterize the compositional and structural properties of the Au-Pd alloy clusters. First, LEIS experiments of various Au coverages (0.1-1.0 ML) on 1.0ML Pd/SiO_2 were carried out. Note that the surface was annealed to 800 K for 10 minutes after each Au deposition and all LEIS spectra were collected at 300 K. Using the same method used to acquire the data of Fig. 46 and 47, the surface concentration of Pd on Au-Pd alloy clusters was measured with various Au coverages and plotted as a function of the Au/Pd atomic ratio in the filled square data of Fig. 49. The dashed line is the calculated Pd concentration assuming that the surface composition reflects the bulk composition. The concentration of Pd at the cluster surface decreases more rapidly than does the dashed line data, indicating that the cluster surfaces are Au-rich compared to the bulk. For comparison, the surface concentration of Pd for Au–Pd/Mo(110) planar surfaces as a function of the Au/Pd atomic ratio has been

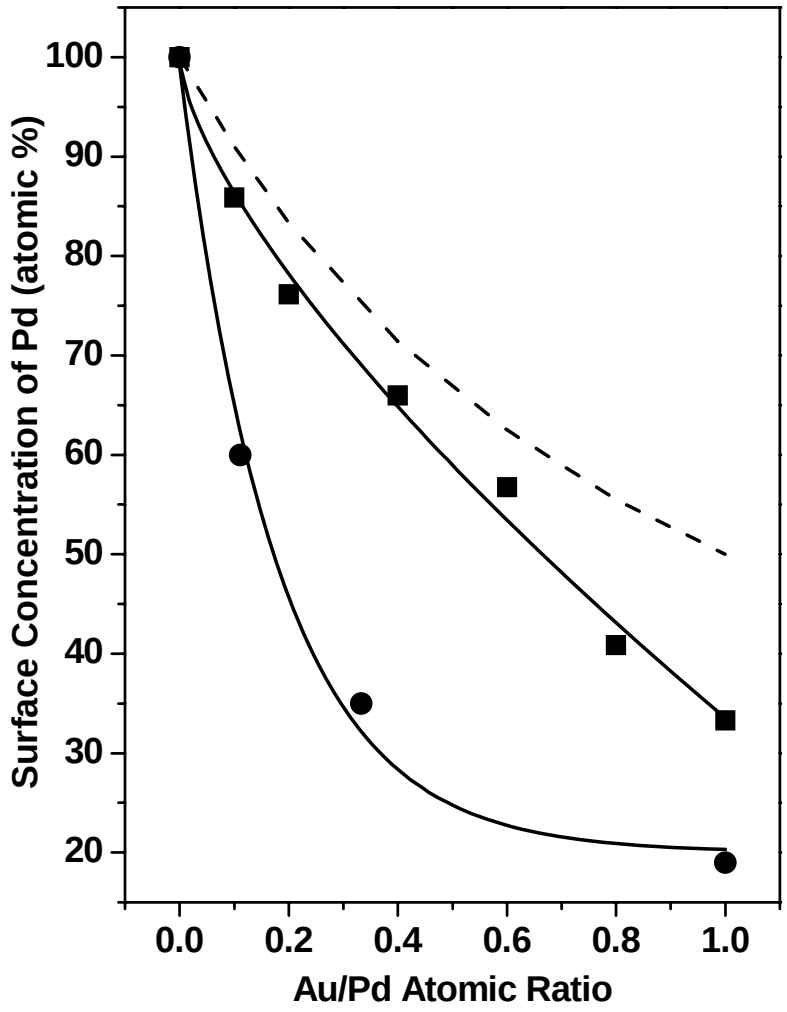

Fig. 49 Surface concentration of Pd as a function of Au/Pd atomic ratio for various Au coverage (0.1-1.0 ML) on 1.0ML Pd/SiO_2 after 800 K annealing (■); for Au–Pd/ Mo(110) after 800 K annealing (●).

plotted in Fig. 49 as the filled circle data. For Au-Pd planar surfaces, segregation of Au to the surface as a function of the Au/Pd ratio is much more significant. For example, for a Au/Pd ratio atomic ratio of ~ 0.11, only ~ 60 % Pd is observed at the surface, whereas for a Au/Pd ratio of 1:1, the surface is only ~ 20 % Pd. In any case, for Au-Pd clusters and extended surfaces, the outermost surface layer is enriched significantly in Au, with the surface concentration of Pd on Au-Pd clusters being greater than that for planar surfaces with an identical Au/Pd bulk composition.

To further characterize the surface composition, CO TPD experiments were carried out to probe the surface structure and absorption sites on 0.1-1.0 ML Au/1.0ML Pd/SiO_2. Note that each surface was annealed to 800 K for 10 minutes, and then cooled to 90 K prior to CO adsorption and TPD. In Figure 50, CO TPD spectra are shown as a function of Au coverage. As discussed earlier, spectrum 50(a) exhibits multiple CO adsorption features on Pd: a-top, bridging, three fold hollow sites, and support-related sites for 1.0ML Pd/SiO_2. With a very small amount of Au deposition, e.g. 0.1ML, an obvious signal reduction was detected for the three-fold hollow sites at 465 K in 50(b), and a slight intensity increase for the a-top site features at 250 and 320 K. Simultaneously, an increase in the low temperature desorption feature at 135 K was observed due to the addition of Au. Considering the relatively large density of Pd clusters,[145,146] higher sticking coefficients of Au on Pd versus Au on silica, and the low Au coverage of 0.1ML, we assume that all Au atoms nucleate on Pd clusters to form alloy clusters after annealing. Alloying leads to the following: (a) the formation of 85 % Pd versus 15 % Au on the alloy cluster surfaces (from the LEIS data in Figure 49 with a Au/Pd ratio of

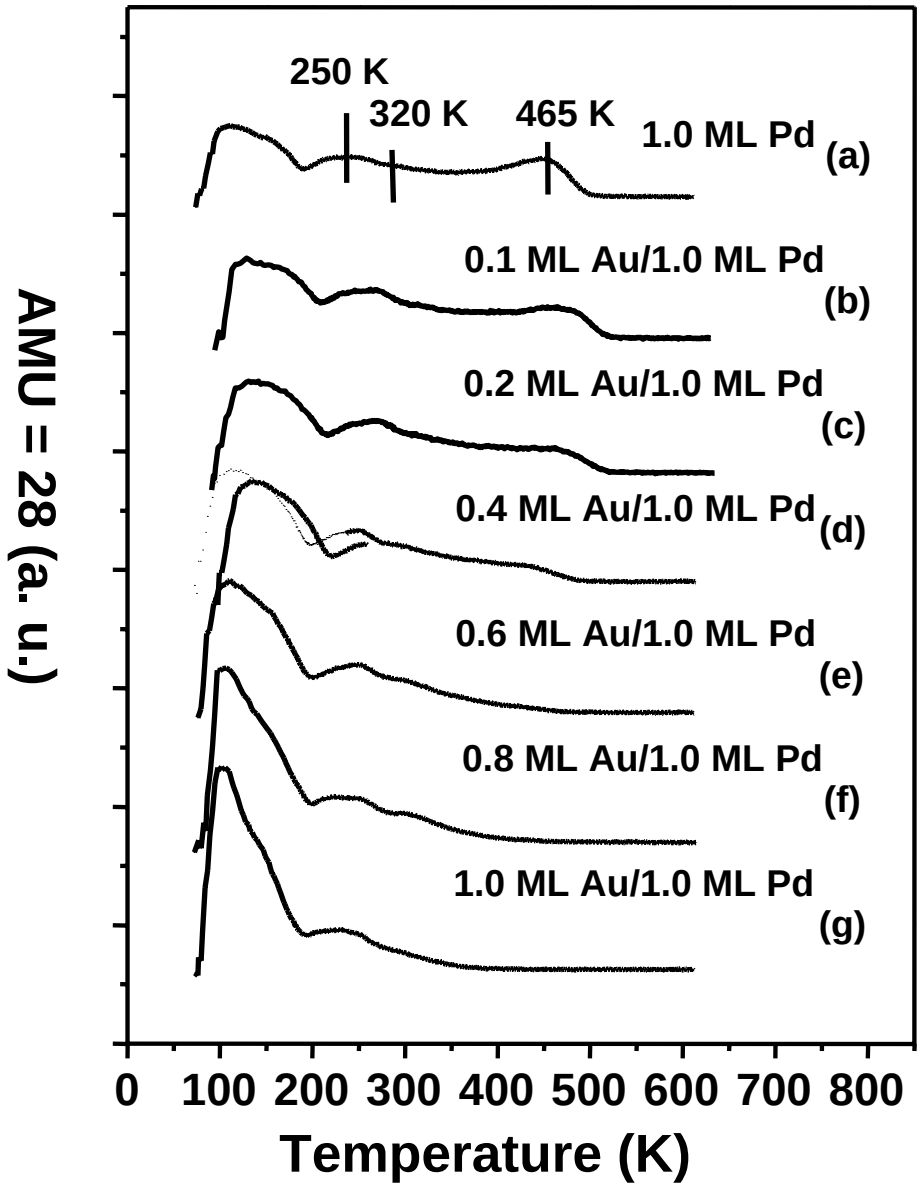

Fig. 50 CO TPD with 1.0 L CO exposure at 90 K of different Au coverage (0.1 - 1.0 ML) on 1.0 ML Pd/SiO_2.

0.1); (b) diminution of the Pd three-fold hollow site density; and (c) an increase in the density of the Pd a-top sites. As the Au coverage increases from spectrum 50(b) to 50(d), the density of the Pd three-fold hollow features progressively decreases. These features completely vanish at a Au coverage of 0.6 ML in spectrum 50(e). In this transition, the signal intensity of the feature between 320 and 465 K, assigned to Pd bridging sites, also gradually decreases at 0.6 ML Au coverage. However, the Pd a-top features at 250 and 320 K remain unchanged up to 0.6 ML Au. With increasing Au coverage to 1.0ML, the bridging sites completely disappear and the intensity of the a-top feature decreases ~ 30 %. As a result, the loss of Pd bridging/three fold hollow sites and the prevalence of a-top sites are apparent on the Au-Pd alloy cluster surfaces.

IRAS studies addressing the surface morphology of the Au-Pd clusters were first carried out by adsorbing CO on 1.0ML Au/SiO_2/Mo(110). The spectra as a function of temperature are shown in Figure 51. Only a single, sharp feature at 2109 cm^{-1} is evident at 80 K, and is assigned to CO on Au a-top sites.[27,151] The intensity of this feature decreases with an increase temperature and its position blue-shifts to 2129 cm^{-1} at 175 K; at 200 K the intensity of this feature vanishes. This behavior parallels closely the TPD results of Figure 48(c), where no CO desorption was detected above 200 K. The blue-shift for the Au clusters is decidedly different from the red-shift for CO adsorption on Pd clusters.[27] The blue-shift is characteristic of CO on Au clusters and, accordingly can be used to identify Au-only clusters. In Figure 52, IRAS spectra of CO adsorption on 1.0ML Pd/SiO_2 are shown as a function of temperature. A relatively narrow feature at ~ 2105 cm^{-1} and a broad feature extending from 2000 to 1875 cm^{-1} are apparent at 80 K.

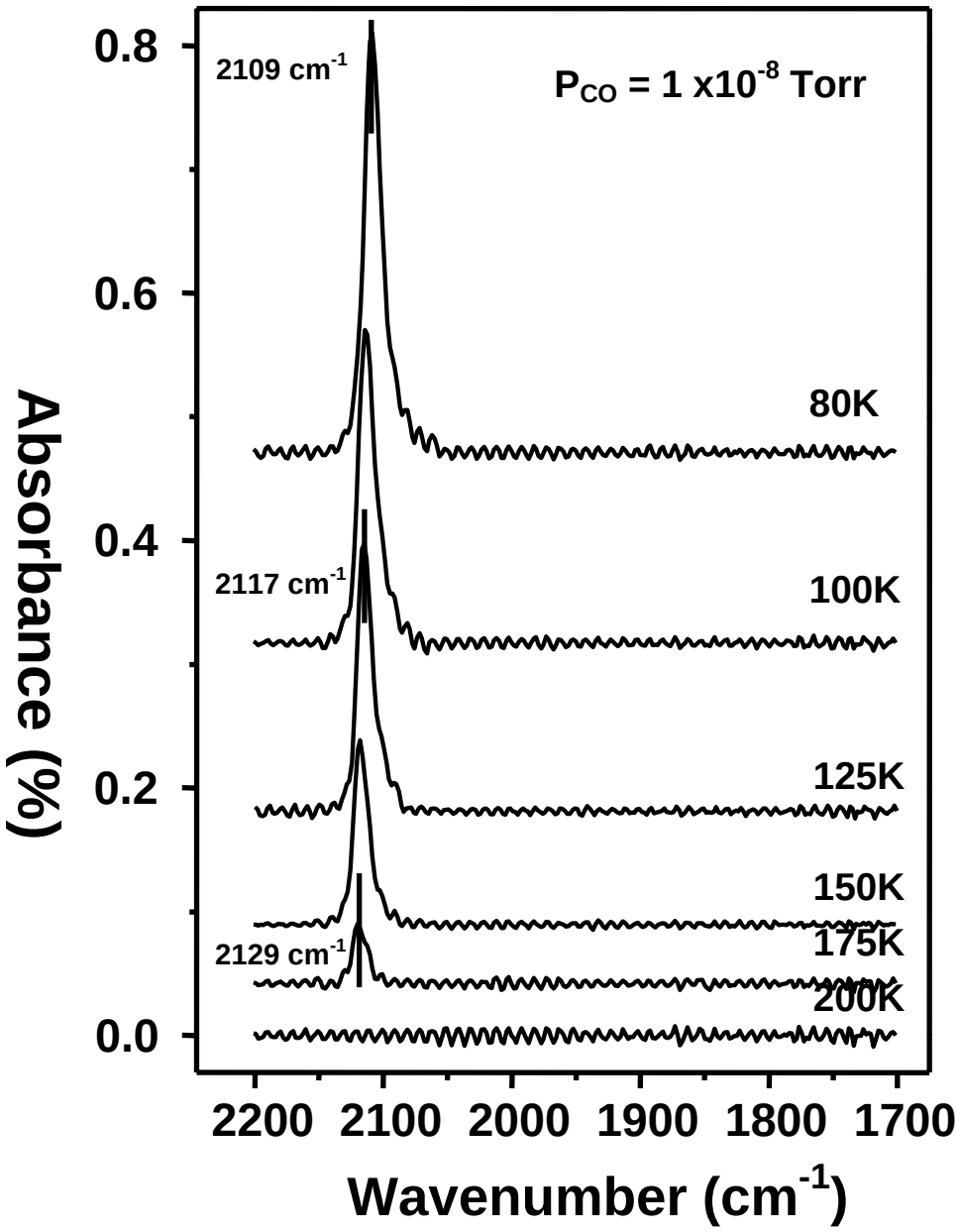

Fig. 51 IRAS spectra of CO adsorption on 1.0ML $Au/SiO_2/Mo(110)$ as a function of temperature**.**

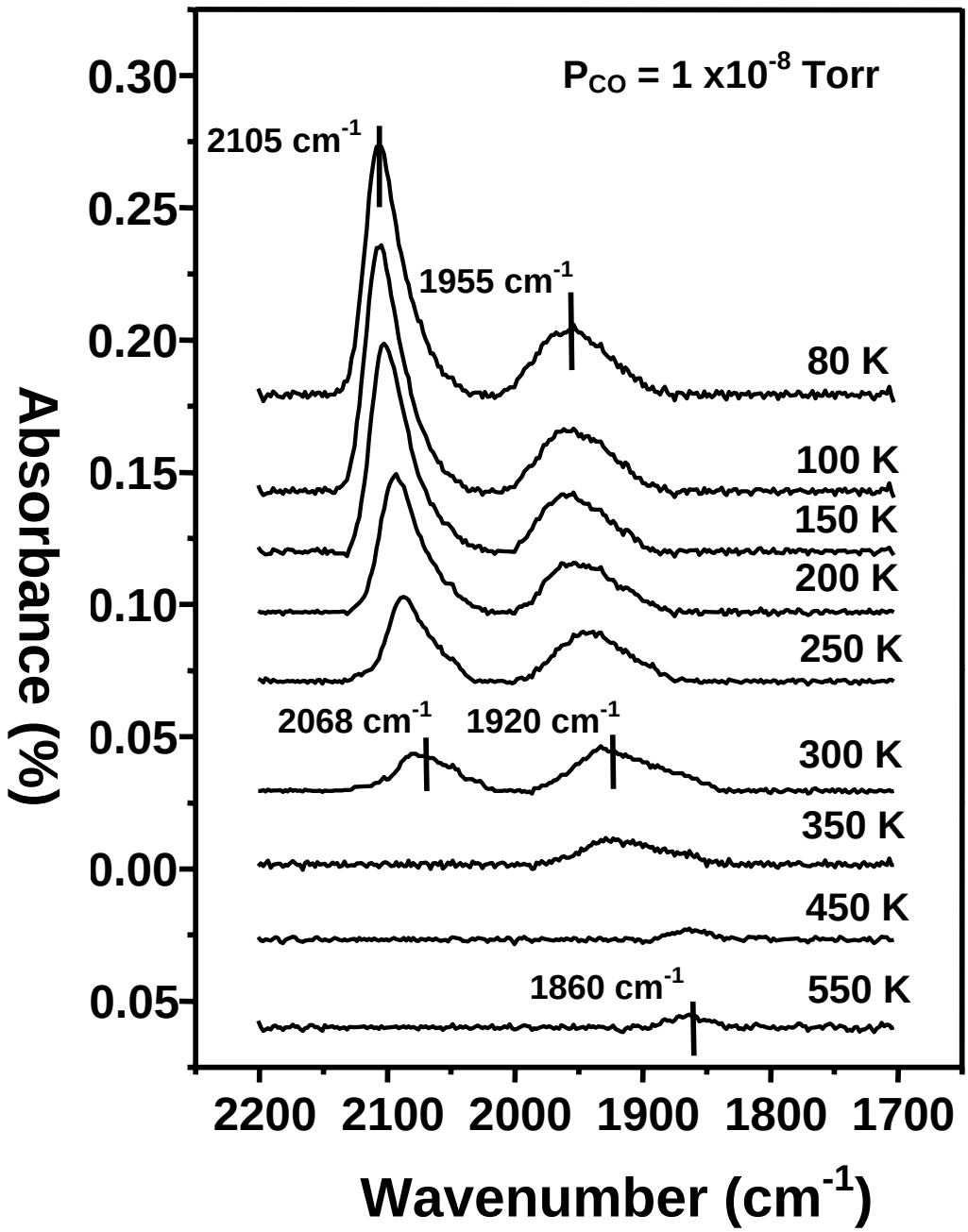

Fig. 52 IRAS spectra of CO adsorption on 1.0ML Pd/SiO_2/Mo(110) as a function of temperature**.**

Extensive studies have been carried out with IRAS of CO adsorption on Pd(111), Pd(100), and oxide supported nano-size Pd particles.[27,43,94,149,150,152] From studies on Pd(111) and Pd(100), three CO adsorption sites, a-top, bridging, and three-fold hollow sites are observed with CO stretching frequency ranging from 2090–2120 cm^{-1}, 1895-2000 cm^{-1}, and 1830-1920 cm^{-1}, respectively. For alumina- or silica-supported Pd clusters,[27,43,94,149,150,152] the CO adsorption sites and their corresponding frequencies are in agreement with previous work on Pd(100) and Pd(111). Accordingly, the high frequency feature at ~ 2105 cm^{-1} is assigned to CO on Pd a-top sites and the broad band at 2000 cm^{-1}-1875 cm^{-1}, to CO on bridging and three fold hollow sites.[27,43,94,149,150,152] With increasing temperature, the a-top feature red-shifts to 2068 cm^{-1} at 300 K; the signal intensity gradually decreases and completely vanishes at 350 K. Concomitantly, the intensity of CO on bridging/three fold hollow sites also decreases. The peak position red-shifts to ~ 1860 cm^{-1} before the signals completely disappears above 550 K. These data closely agree with the previously reported IRAS data for small Pd particles grown on SiO_2 and Al_2O_3.[27,43,94,149,150,152] The CO adsorption sites and the corresponding desorption temperatures agree with the CO TPD results discussed above.

In Figure 53, the IRAS spectra of CO absorbed on 1.0ML Au/1.0ML $Pd/SiO_2/Mo(110)$ are presented as a function of temperature. At 80 K, a sharp feature at 2112 cm^{-1} with a small shoulder at lower frequency side is apparent with no features corresponding to CO adsorbed on Pd in bridging or three fold hollow sites. As the temperature is increased, the primary feature blue-shifts to 2122 cm^{-1} at 200 K and completely vanishes at 250 K. According to the distinctive blue-shift exhibited by CO

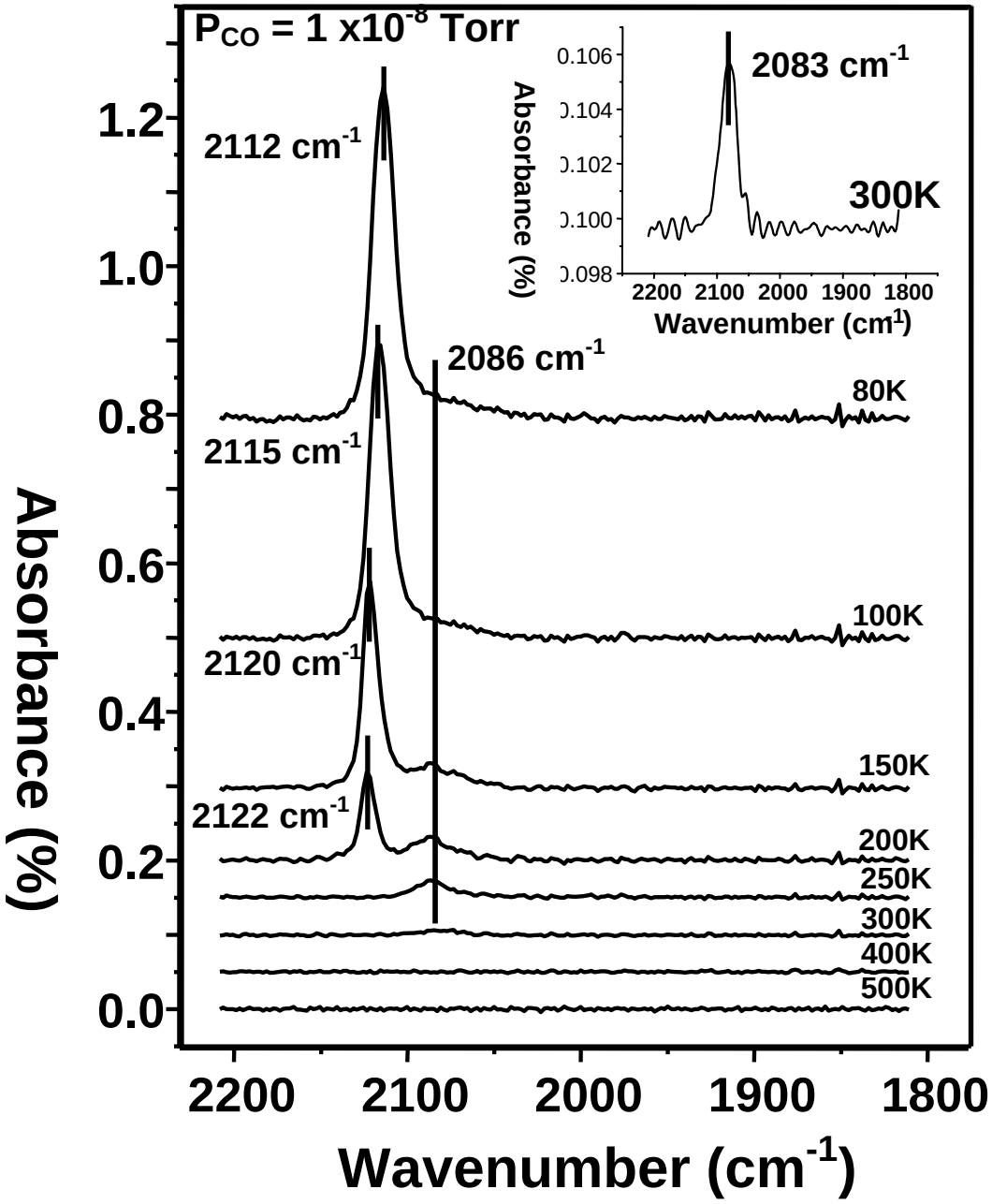

Fig. 53 IRAS spectra of CO adsorption on 1.0ML Au/1.0ML Pd/SiO_2/Mo(110) as a function of temperature**.**

stretching frequency on Au clusters upon annealing in Figure 51 and the complete loss of signal intensity at 250 K, we conclude that the feature at 2112 cm^{-1} is from CO adsorbed on Au a-top sites. The shoulder observed on the low frequency side of the 2112 cm^{-1} peak at 80 K is clearly evident at 150 K with a stretching frequency at 2086 cm^{-1} and distinctly resolved from the Au a-top sites at 200 K. Furthermore, it is the only CO feature present at 250 K. In the inset of Figure 53, this feature can still be seen at 2083 cm^{-1} at 300 K. This unique feature, with a frequency of ~ 20 cm^{-1} lower than CO adsorbed on regular Pd a-top sites on Pd single crystal substrates and oxides supported clusters,[27,43,94,103,149,150] is characteristic of a Au-Pd alloy cluster surface, and has been observed for Au-Pd planar alloy surfaces and for alumina supported Au-Pd clusters.[27] No significant frequency shift was observed over the entire temperature range investigated. With consideration of enhanced surface segregation of Au and the characteristic a-top Pd sites observed by CO TPD, the Pd atoms are believed to be surrounded by Au atoms, forming isolated Pd sites on the alloy clusters of 1.0ML Au/1.0ML Pd/SiO_2. The red-shift can be due either to stronger bonding of CO to the isolated Pd or to reduced lateral destabilization of CO on the surrounding Au atoms. The apparent stabilization of the CO/Au feature in the IRAS data of Figure 53 compared with the CO/Au-only feature of Figure 51 may be a consequence of a small electronic effect of Pd on the surrounding Au atoms.

IRAS experiments for CO adsorption on silica supported Pd–Au clusters with different compositions and deposition orders were further carried out. Figures 54 and 55 display temperature dependent spectra for 1ML Au/3ML Pd/SiO_2 and 1ML Au/5ML

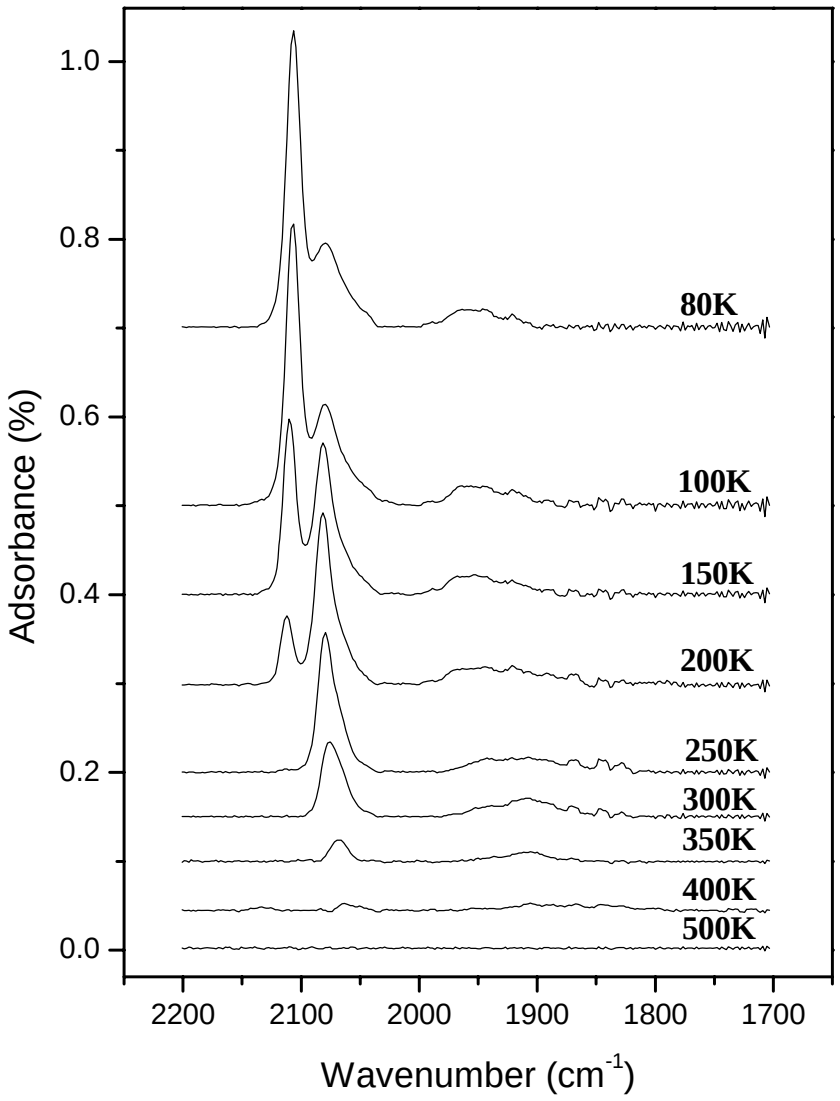

Fig. 54 IRAS spectra of CO adsorption on 1.0 ML Au / 3.0 ML Pd / SiO_2 / Mo(110) as a function of temperature.

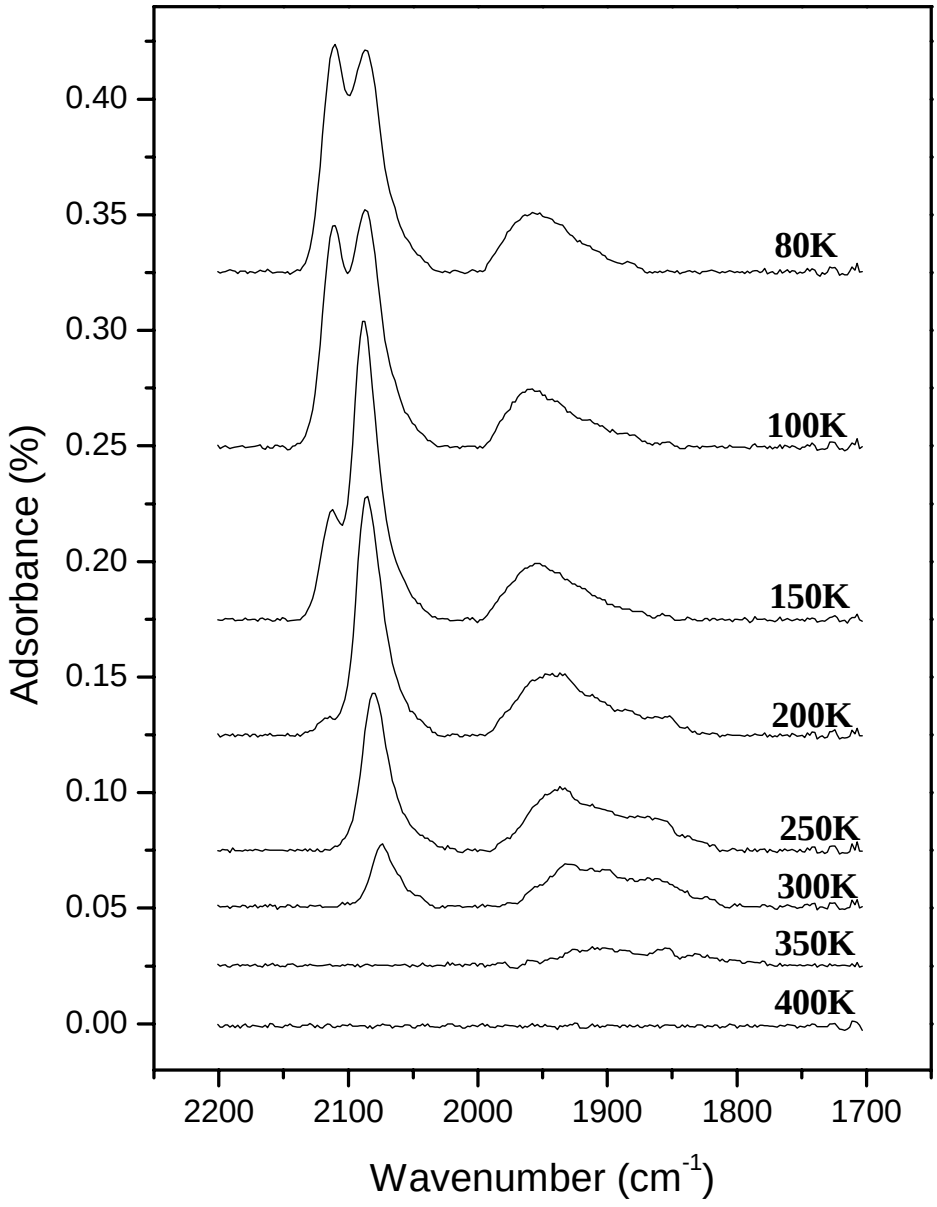

Fig. 55 IRAS spectra of CO adsorption on 1.0 ML Au / 5.0 ML Pd / SiO_2 / Mo(110) as a function of temperature.

Pd/SiO_2 systems in a CO background pressure of 1×10^{-7} Torr. In both cases, Pd particles were first deposited on the silica substrate followed by an anneal at 800 K for 20 minutes. Then Au was vaporized on the surface, and a final anneal at 800 K for another 20 minutes was performed prior to CO exposure. Most of the spectral features in Fig. 53, 54, and 55 are similar. The only difference is the increasing in intensity of Pd related features as the bulk Pd concentration increases. But even for 1ML Au/3ML Pd/SiO_2 system (Figure 54), the Pd multifold sites peak is still hardly observed, and the Pd atop sites feature is also smaller than Au atop feature. This may indicate that Au still enriches on the surface for this composition. It should also be noted that the CO Au atop feature desorbs from the surface higher than 200 K for 1ML Au/3ML Pd/SiO_2 system, showing the CO–Au bonding is more stabilized than that on pure Au surface. However, once the Pd concentration increases to 5 ML (Fig. 55), the CO-Au-IR feature disappears below or around 200 K, behaving more like pure Au surface. This trend clearly shows that the interaction of CO and Au becomes stronger when a small amount of Pd is present on the surface. However, the underlying reason for this observation still

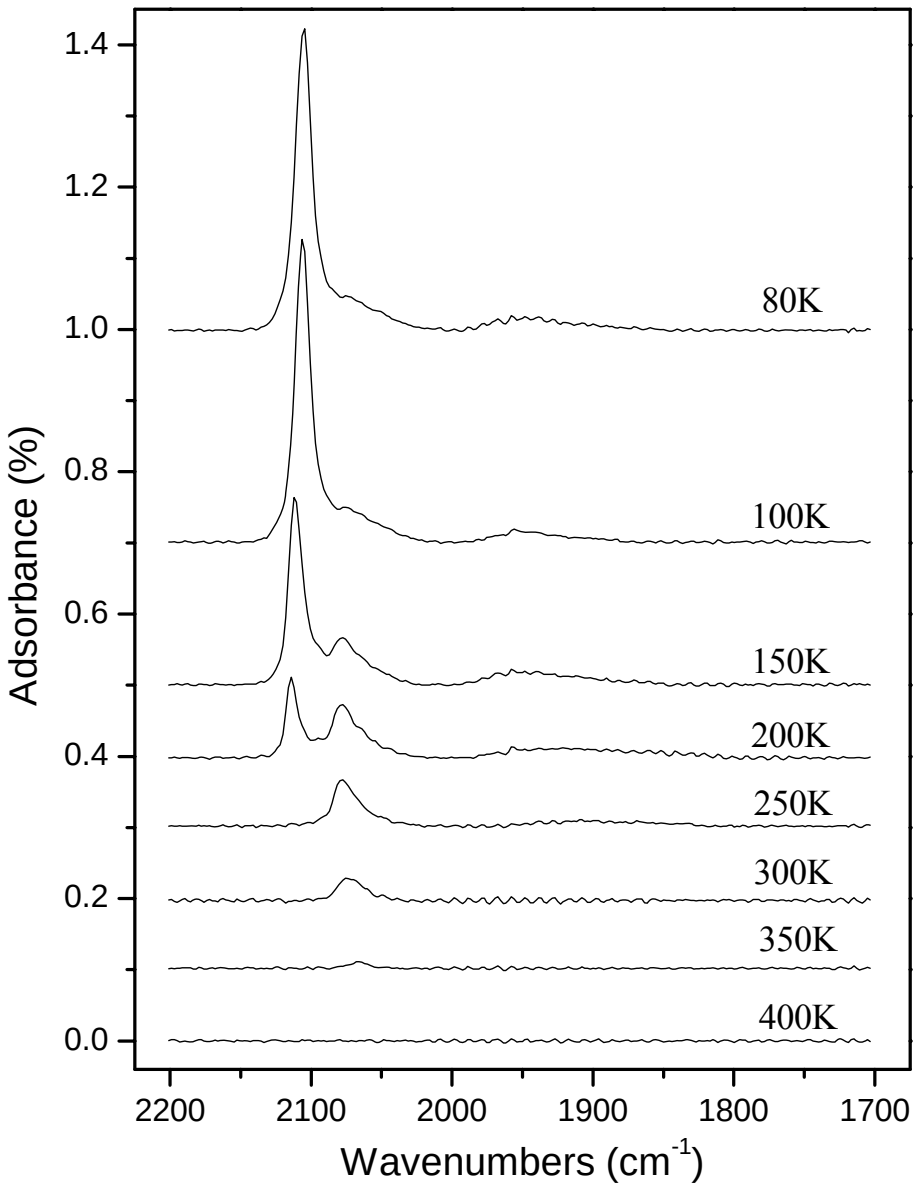

Fig. 56 IRAS spectra of CO adsorption on 1.0 ML Pd / 1.0 ML Au / SiO_2 / Mo(110) as a function of temperature.

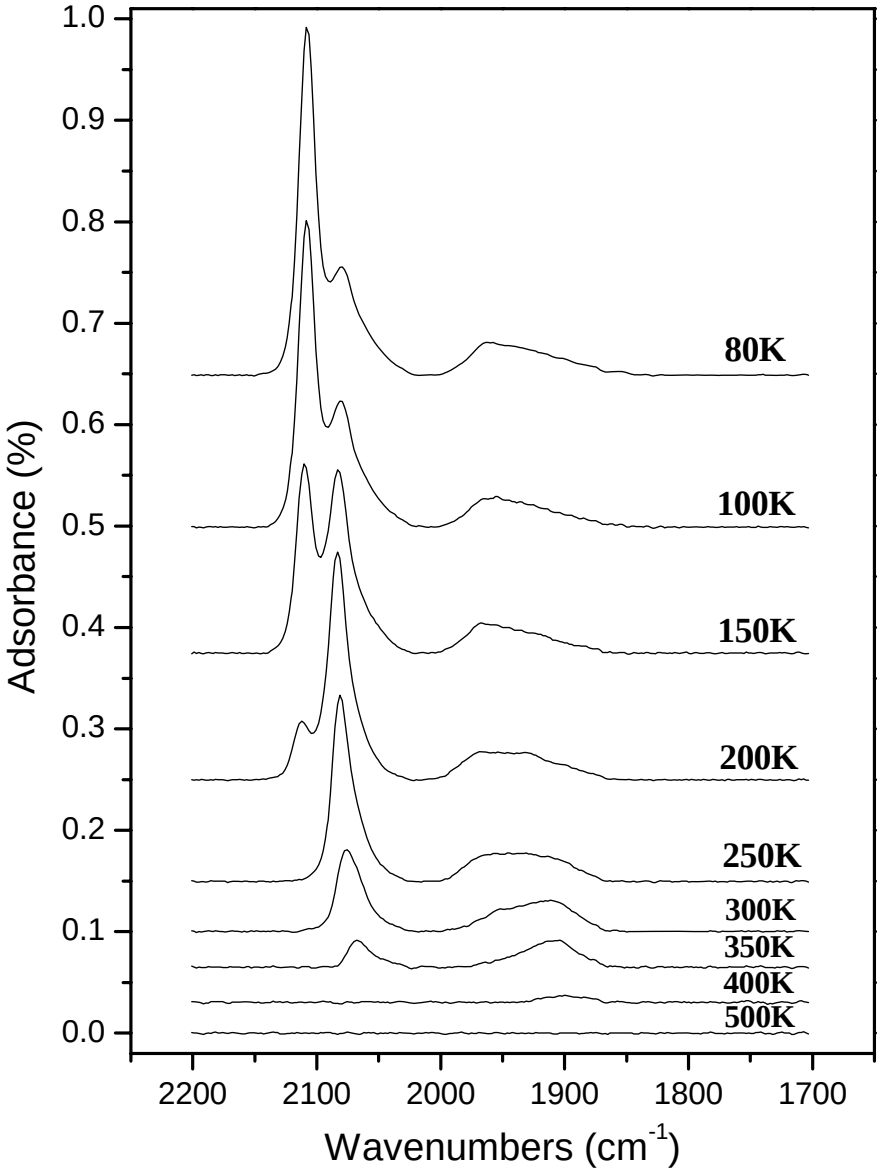

Fig. 57 IRAS spectra of CO adsorption on 3.0 ML Pd/1.0 ML Au/SiO_2/Mo(110) as a function of temperature**.**

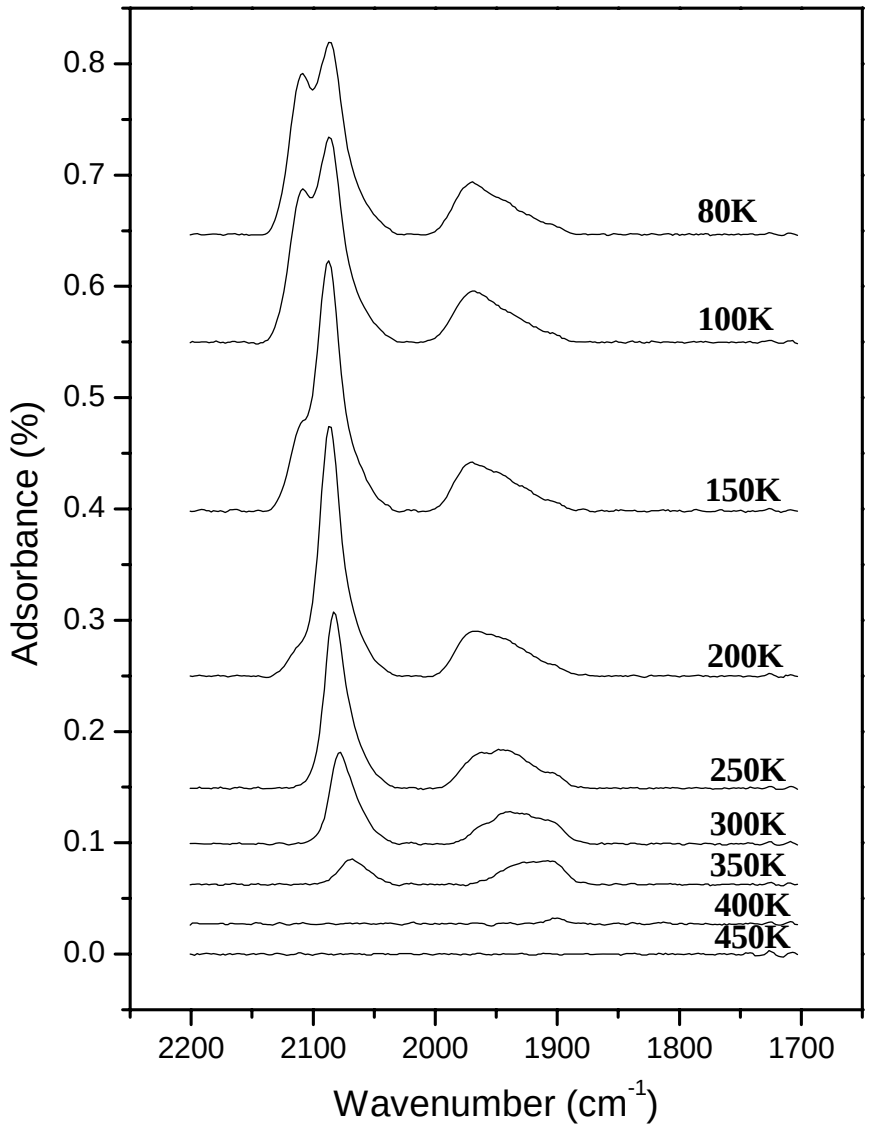

Fig. 58 IRAS spectra of CO adsorption on 5.0 ML Pd/1.0 ML Au/SiO_2/Mo(110) as a function of temperature**.**

demands more investigations. In Figure 56, 57, and 58, CO IRAS spectra from alloy clusters with same metal composition like Fig. 53, 54, and 55, but different deposition order were displayed. As can be clearly seen, the IR features, frequencies, and relative intensity ratios from these two sets of data are essentially the same, indicating a thermodynamically stable alloy systems can be prepared after annealing regardless of the opposite deposition order.

To summarize, the growth of Au-Pd alloy clusters via a sequential deposition and annealing on amorphous ultra-thin SiO_2 films has been characterized using LEIS and CO TPD. The surface composition of the Au-Pd clusters is shown to be Au-rich compared to the bulk of the cluster as observed previously for extended Au-Pd surfaces. However, the extent of Au enrichment is less for the Au-Pd clusters compared to the extended surfaces. CO adsorption on the Au-Pd alloy cluster surfaces was studied by TPD and IRAS and isolated Pd sites were identified as a unique surface ensemble. A thermodynamically stable alloy systems can be prepared after annealing regardless of the opposite deposition order.

Pd–Sn/Rh(100)

Using alloys to further optimize the catalytic performance requires a thorough understanding of the reaction mechanism at the atomic level. Hence, model surface science approaches on well-defined surfaces are needed. In this regard, previous studies on Pt-Sn alloy systems provided a fine example. The preparation of ordered Pt–Sn surface alloys was first demonstrated by depositing Sn on Pt(111) (or Pt(100)) and annealing the Sn/Pt(111) system at elevated temperatures.[153-156] Then these well-characterized surface templates were used for extensive catalytic reaction studies.[157-162] Together with theoretical calculations, the origin of the altered chemistry observed on these ordered surface alloy structures, such as the relative importance of ensemble and ligand effects, has been better understood.

However, a very limited number of model studies on Pd–Sn bimetallic system have been performed despite the importance of Pd based catalysts in the industry.[163-166] Lee *et al.* and Hamm *et al.* have described the formation of two ordered Pd–Sn surface alloys by flashing the vapor deposited Sn films on a Pd(111) single crystal. Depending on the preparation condition, two surface periodicities, p(2×2) and (√3×√3)R30°, were observed with the surface stoichiometry Pd_3Sn and Pd_2Sn, respectively.[163,164] On Pd(110) single crystal, two ordered structures, c(2×2) and (3×1), were also reported corresponding to 0.5 monolayer (ML) and 0.75 ML of surface Sn coverage.[166] In both these cases, a strong chemical interaction between Sn and Pd was deduced by the core level binding energy shift (CLBES), and a reduced CO adsorption energy was indicated by the temperature programmed desorption (TPD) results.[164,166] But to our knowledge,

no detailed investigation about Pd–Sn alloy formation with (100) orientation is available in the literature.[165]

In this work, the preparation and characterization of Pd–Sn alloy films supported on a Rh(100) substrate have been studied. Particularly, the surface composition, the extent of alloying, and the electronic properties have been investigated by X-ray photoelectron spectroscopy (XPS) and low-energy ion scattering spectroscopy (LEISS). The surface structure and the variation of chemical properties have been elucidated by low energy electron diffraction (LEED), infrared reflection adsorption spectroscopy (IRAS), and TPD using CO as a probe molecule. This work provides necessary information for further catalytic reaction studies on the (100) surface of Pd–Sn alloys, and it is also an extension of our studies on disordered Pd–Au model alloy systems.[167-169] In Pd–Au systems, most of the surface Pd atoms were found to be isolated from each other by Au, and this type of Pd monomers has been proposed to play an important role in determining the catalytic reactivity for several reactions.[167-169] The Pd–Sn system offers a possibility to form ordered surface alloys with only isolated Pd sites. Therefore, the electronic and chemical properties of the isolated Pd sites can be better studied, and the variation of these properties between two systems will greatly help us to address the structure-reactivity relationships.

LEED, LEISS and XPS

LEED and LEISS were combined to elucidate the surface composition and structural properties of Pd–Sn alloy films. In Figure 59, Ne^+ scattering LEIS spectra for 1ML Sn/4ML Pd/Rh(100) surface were displayed as a function of annealing temperature. The alloy surface was annealed at each indicated temperature for 1 minute, and all spectra were collected at 300 K. As expected, a single scattering feature from 4ML Pd/Rh(100) surface was observed with KE of *ca.* 0.47 keV. After depositing 1.0 ML Sn, the Pd scattering peak was attenuated and a new scattering feature, ascribed to Sn, emerged at 0.49 keV. The Pd scattering intensity did not drop to zero at the 1.0 ML Sn coverage, although the Pd peak was much smaller and overlapped with the Sn feature. This may be due to the Sn-Pd interdiffusion at 300 K and the contribution of LEIS signals from the second Pd layer atoms on the open fcc (100) surface.[170] As the annealing temperature was increased, the Pd peak intensity increased while the Sn peak intensity decreased. This change in Pd and Sn intensity was considered as a signpost for the interdiffusion of Sn-Pd.

To analyze the surface composition, the surface concentrations of Sn and Pd were calculated using equation (1) in combination with the LEIS data in Figure 59. The influence of annealing temperature on surface concentration was graphically presented in Figure 60. A decrease in Sn surface concentration (▲) and an increase of Pd surface concentration (■) were observed as the annealing temperature first increases up to 700 K. At 700 K, the surface concentrations of Sn and Pd were *ca.* 47 % and 53 %, respectively. As the temperature rose above 700 K, the diffusion of Sn into the Pd film stopped and

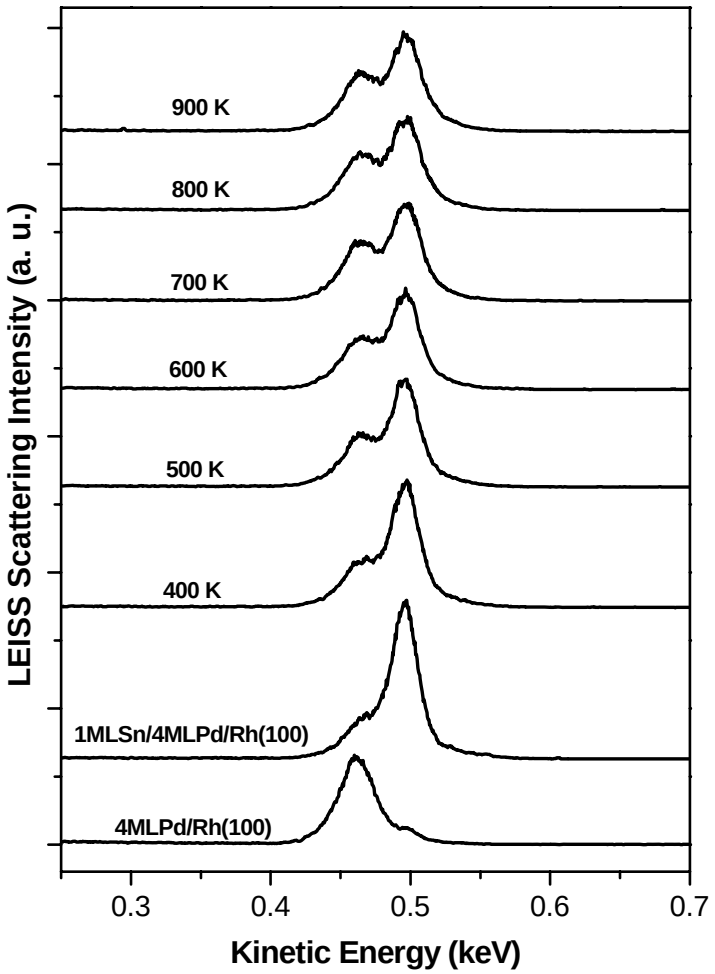

Fig. 59 Ne^{+} scattering LEIS spectra for 1ML Sn/4ML Pd/Rh(100) system as a function of annealing temperature.

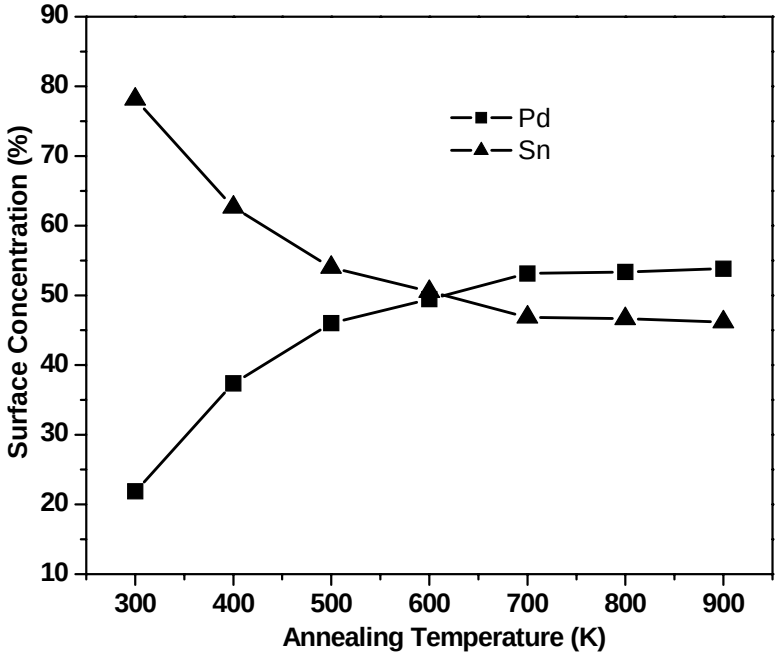

Fig. 60 Surface concentration of Sn and Pd for 1ML Sn/4ML Pd/Rh(100) as a function of annealing temperature.

the surface concentration became constant, indicating a stable surface alloy with Sn to Pd surface ratio as 1:1 was formed after annealing at 700 K.

LEED was used to further characterize alloy surface structures. Fig. 61 displays the LEED pictures from (a) the clean Rh(100) substrate, (b) the 4ML Pd/Rh(100) surface, and (c) the 1ML Sn/4ML Pd/Rh(100) surface. Both the Pd film and the Pd-Sn alloy film were annealed at 700 K for 1 minute before taking the picture. As shown, the 4ML Pd film exhibited a clear (1×1) LEED pattern (Fig. 61(b)), indicating the Pd film adopts a substrate–like (100) orientation. Since the lattice difference between Pd and Rh is quite small, it is not surprising that the Pd film grows pseudomorphic overlayers. Relatively diffused spots and higher backgrounds compared with clean Rh(100) surface (Fig. 61(a)) suggested the Pd film is not as ordered as substrate Rh(100) surface. After deposition of 1ML Sn on this Pd film and annealing the sample surface to 700 K, a new LEED pattern, c(2×2), was clearly observed (Fig. 61(c)). From the above LEISS results, it was known that the surface concentration of Pd and Sn are close to 50 % after annealing the sample surface to 700 K. Therefore, an ordered Pd–Sn alloy structure like those depicted in the bottom of Fig. 61 can be derived. It should be pointed out that similar ordered structure was also observed in Pt–Sn alloy systems with (100) oritenstion.[155]

In order to probe the proper preparation conditions for ordered Pd–Sn alloy surface, LEISS experiments with deposition of different amounts of Sn on 4ML Pd film were carried out. The changes of surface Pd and Sn concentrations for this process are calculated and shown in Fig. 62. It should be noted that each of these alloy surface

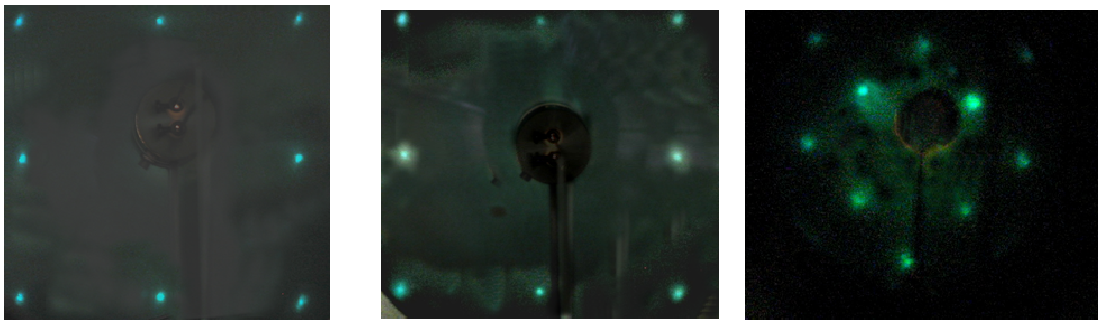

a. Clean Rh(100) @ 83 eV **b. 4 ML Pd/Rh(100) @ 80 eV** **c. 1 ML Sn/4 ML Pd/Rh(100) annealed at 700K for 1 min @ 77 eV**

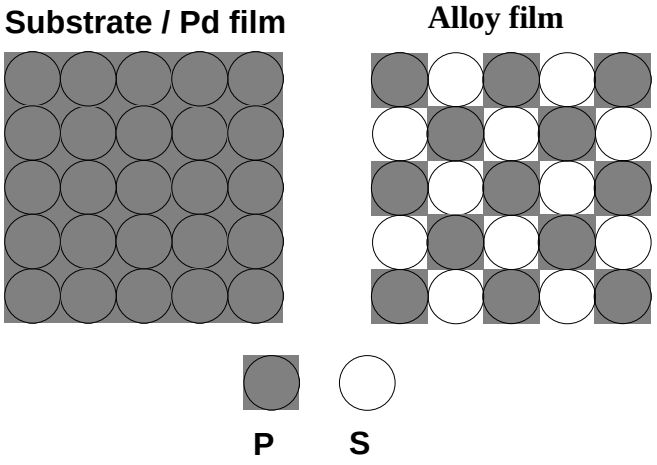

Fig. 61 Top: LEED pictures for (a) the clean Rh(100) substrate, (1×1); (b) the 4ML Pd/Rh(100) surface, (1×1); and (c) the 1ML Sn/4ML Pd/Rh(100) surface, c(2×2). Both the Pd film and the Pd–Sn alloy film were annealed at 700 K for 1 minute before checking the LEED. The photos were taken at 300 K, and the incident electron beam energies were shown along with the pictures. Bottom: Ball-structure representations of pure Pd and ordered alloy films.

was annealed at 700 K for 1 minute prior to the LEISS experiment. Ideally, 0.5ML Sn is needed to form a c(2×2) ordered Pd–Sn alloy surface if the diffusion of Sn into bulk Pd film is limited. Our results indeed show the surface concentration of 0.5ML Sn/4ML Pd/Rh(100) alloy system is 40 % Sn and 60 % Pd, close to the Sn:Pd 1:1 ratio. This observation is actually expected because of the fact that the surface free energy of Sn is much smaller than that of Pd. Therefore, the diffusion of Sn into bulk Pd film is thermodynamically unfavorable. However, when more than 0.5ML Sn was vaporized onto the surface, the final surface concentrations after annealing for these systems were also close to 50 %. Most probably, the extra Sn in these cases diffuses into the second layer in order to form the c(2×2) ordered structure at the outmost surface layer.

XPS was used to study the electronic structures of Sn–Pd alloys. In Figure 63, Sn 3d core level spectra were shown as a function of annealing temperature for 1ML Sn/4ML Pd/Rh(100) system. No strong peak intensity or CLBE variation occurred as the annealing temperature was scaled to 700 K. A large decrease in intensity and a slight lower binding energy shift were detected after annealing at 700 K. The Pd 3d core level peaks were also followed and shown in Figure 64. The CLBE values for Pd 3d features did not change significantly following Sn deposition and annealing at different temperatures, but the intensities of these peaks were attenuated after annealing the alloy film higher than 800 K. Probably, the inter-diffusion of Pd into Rh substrate is responsible for this observation.

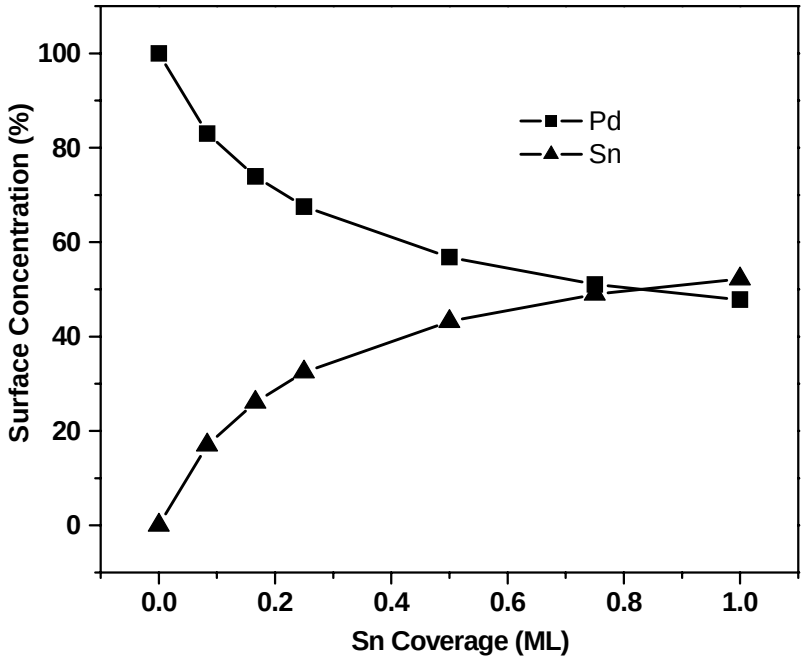

Fig. 62 Surface concentration of Sn and Pd for different amount of Sn deposited on 4ML Pd/ Rh(100) surface. Each alloy surface was annealed at 700 K for 1 minute before performing LEISS experiment.

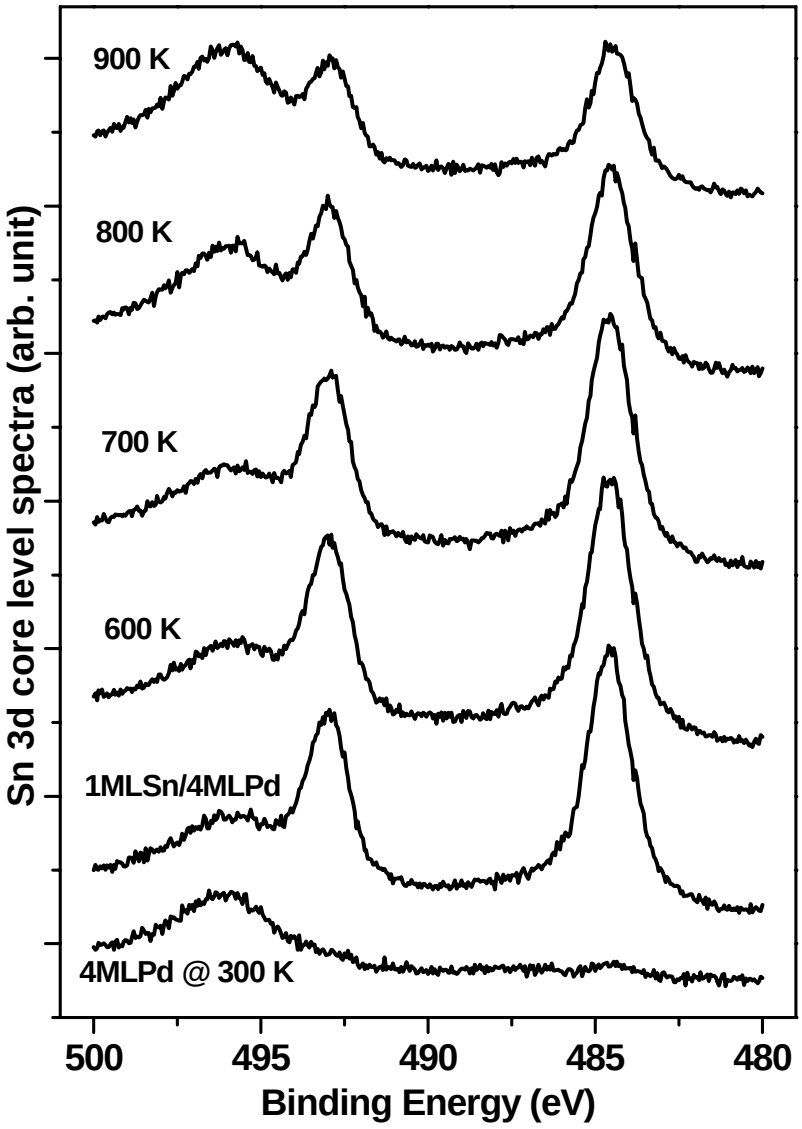

Fig. 63 XPS Sn 3d core level spectra of 1ML Sn/4ML Pd/Rh(100) as a function of annealing temperature**.**

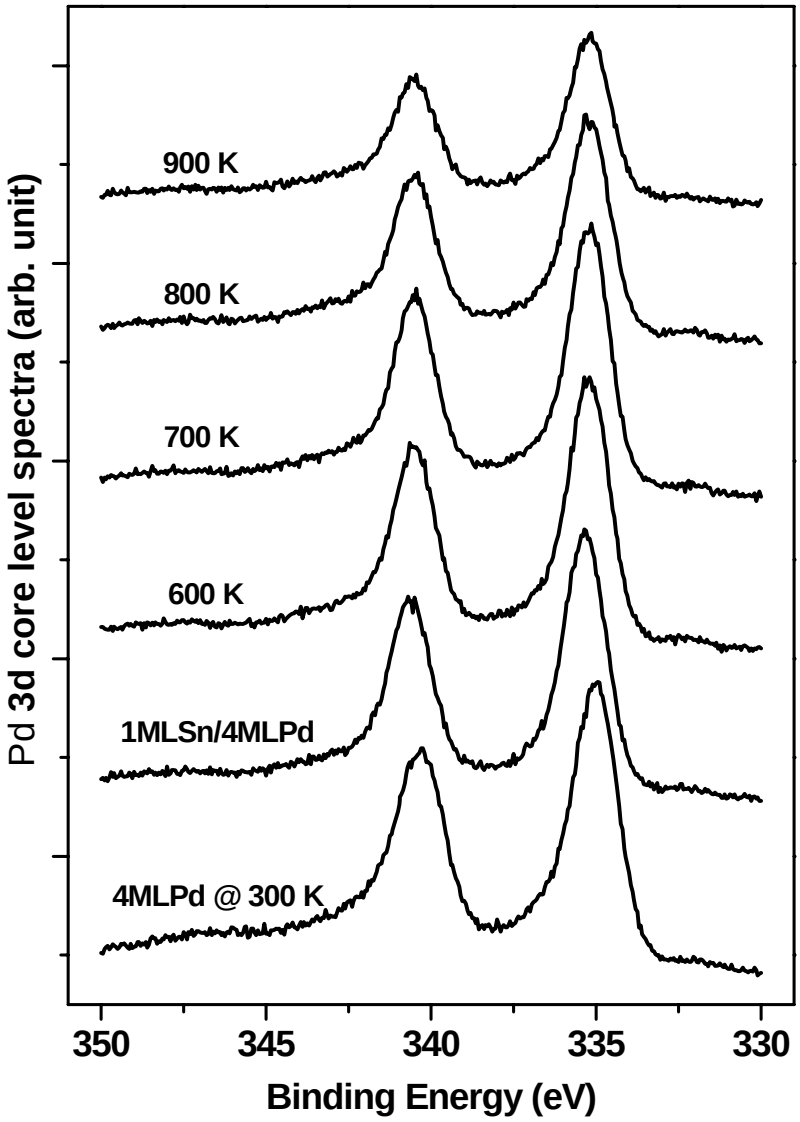

Fig. 64 XPS Pd 3d core level spectra of 1ML Sn/4ML Pd/Rh(100) as a function of annealing temperature**.**

IRAS and TPD

IRAS and TPD experiments using CO as a probe molecule were combined to address the information about the surface adsorption sites and morphology. The control experiments on 4ML Pd film were first carried out. Fig. 65 displays a series of IRAS spectra on this surface acquired in 1×10^{-7} Torr CO background as a function of sample temperature. Only one feature was observed in this series of spectra. This feature appears as broad peak around 1908 cm^{-1} at 500 K, then gradually blue shifts to 1985cm^{-1} when the sample temperature drops to 250 K. At CO saturation coverage, this feature reaches 2001 cm^{-1} and becomes much sharper. Recalling the CO–IRAS spectra performed on a Pd(100) single crystal in a similar condition,[171] both spectral feature and temperature dependent frequency shift are essentially identical in these two cases. This clearly indicates that the 4ML Pd film supported on a Rh(100) single crystal adopts a (100)–like orientation, which correlates very well with the above LEED results. Based on the TPD and LEED studies performed on Pd(100) single crystal surface,[172] this CO–IR feature has been assigned to CO adsorption on two–fold bridging Pd sites.

IRAS spectra for CO adsorption on 1ML Sn/4ML Pd/Rh(100) surface as a function of sample temperature were displayed in Fig. 66, provided that the alloy surface was annealed at 700 K for 1 minute and all the spectra were collected in 1×10^{-7} Torr CO background. Only a single IR feature around 2094 cm^{-1} is apparent in this series of spectra. Comparing with the single feature observed on 4ML Pd film surface at 2001 cm^{-1}, this IR result clearly shows that totally different adsorption sites are formed on Pd

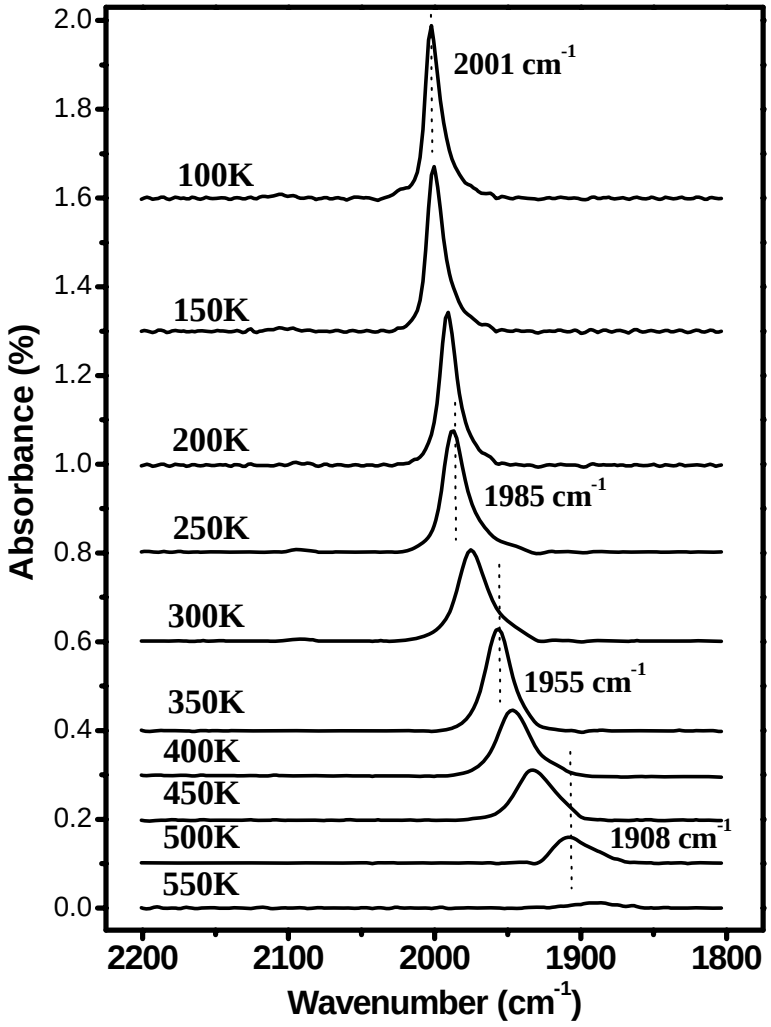

Fig. 65 IRAS spectra for CO adsorption on 4ML Pd/Rh(100) surface as a function of sample temperature**.**

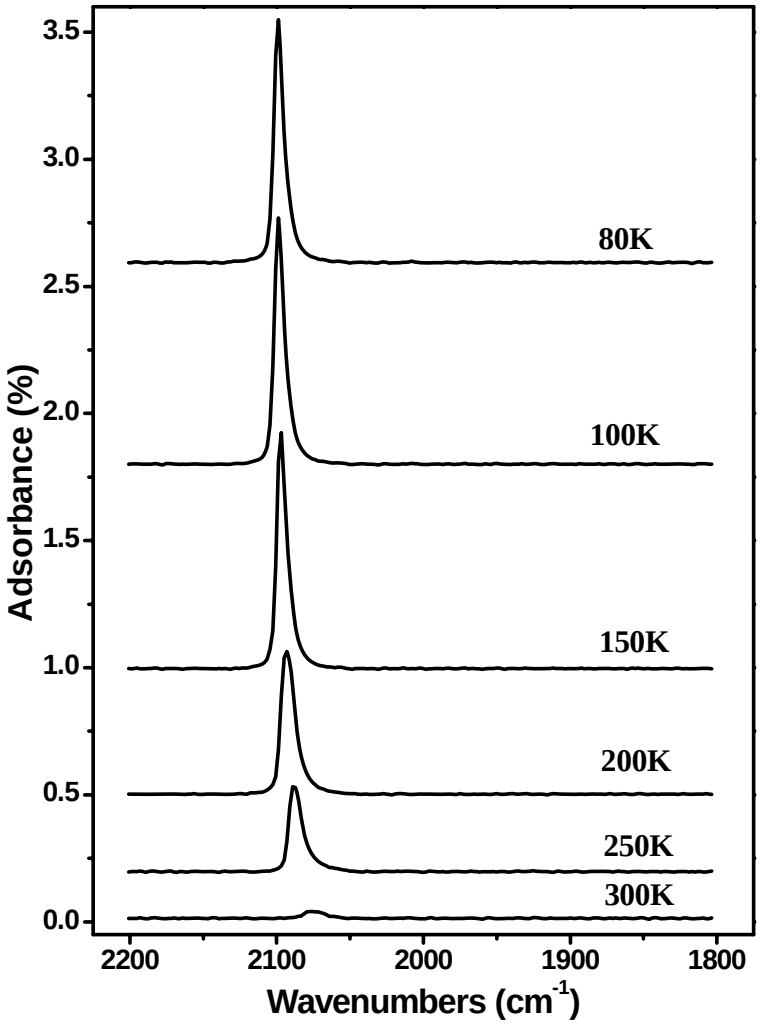

Fig. 66 IRAS spectra for CO adsorption on 1ML Sn / 4ML Pd / Rh(100) surface as a function of sample temperature. The alloys surface was annealed at 700 K for 1 minute.

–Sn alloy surface. According to this frequency, this feature falls into the range of CO adsorption on atop Pd sites. Moreover, this IR feature starts to attenuate between 150 and 200 K, and completely disappears below 300 K. On 4ML Pd film surface, CO–IRAS feature can be seen up to 500 K. This difference also supports that CO adsorbs differently on the Pd–Sn alloy surface. The lower desorption temperature normally indicates the weaker CO–substrate bonding. This parallels very well with IR frequency assignment that CO adsorb on atop Pd sties. It is also worth mentioning that the IR frequency for isolated Pd sites on Pd–Au alloy surface is 2088 cm^{-1}, and this isolated Pd IR feature in the Pd–Au system vanishes around 300 K. The similarities in both IR frequency and CO desorption temperature in these two systems may suggest that CO shares the identical adsorption sites in both these systems (i.e. CO also adsorbs on the isolated Pd sites on Pd–Sn alloy surface).

The direct comparison of saturation CO–IRAS spectra from 4ML Pd film, 4ML Sn film, and 1ML Sn/4ML Pd alloy film further supports the above speculation. As can be seen in Fig. 67, no IR feature is observed on 4ML Sn film surface at 80 K. This is mainly due to the extremely weak interaction between Sn and CO. However, this also proves that CO has to adsorb on Pd related adsorption sites. And based on the above LEISS and LEED results, 1ML Sn/4ML Pd alloy film annealed at 700 K forms a well–ordered c(2×2) alloy structure. Therefore, it is reasonable to conclude that the IR feature observed on Pd–Sn alloy surface arises from CO adsorption on the isolated Pd sites. With the sensitivity of IRAS, it is surprising that only the isolated Pd IR feature is observed on Pd–Sn alloy surfaces. This means that most of the Pd atoms on

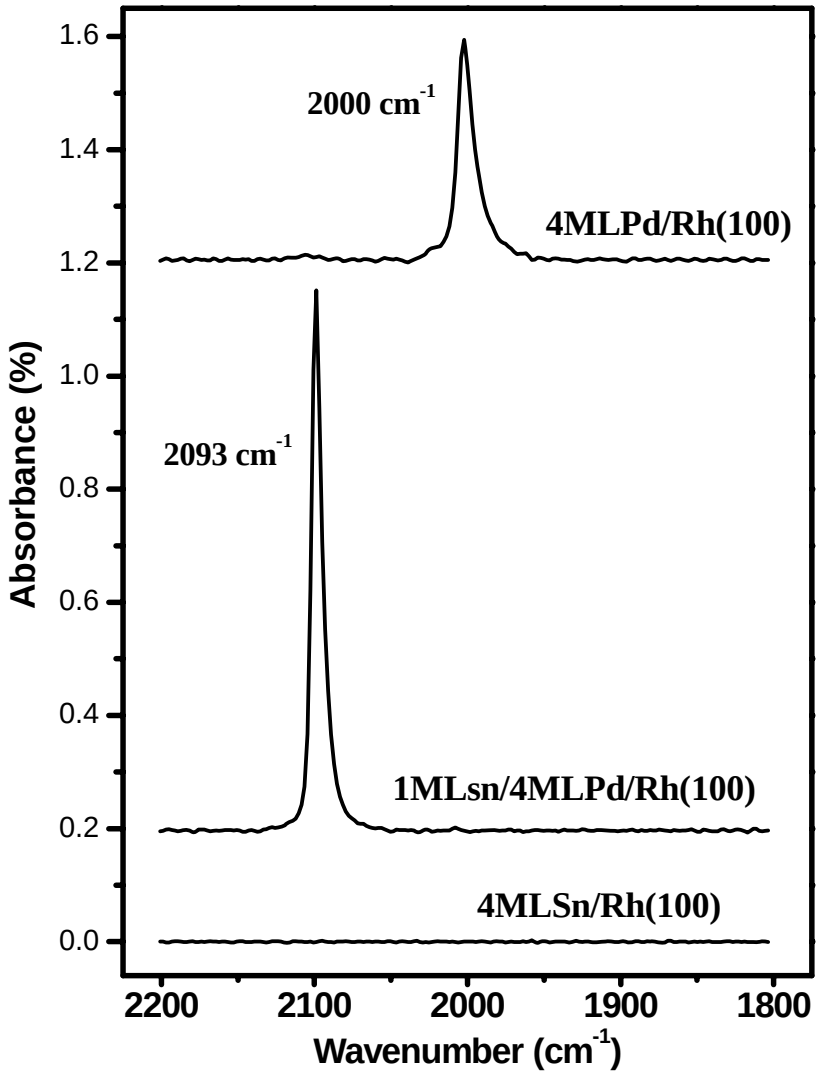

Fig. 67 Comparison of IRAS spectra for CO adsorption on 4ML Pd film, 1ML Sn/4ML Pd alloy film and 4ML Sn film on Rh(100) at saturation CO coverage. The alloy film was annealed at 700 K for 1 minute, and the spectra were acquired at 80 K.

Pd–Sn alloy surfaces are isolated with each other. In other words, a perfectly ordered alloy surface must be formed.

It should be also noted that the IR frequency for the isolated Pd sites in Pd–Sn alloy systems is slightly higher than that in Pd–Au systems (2094 cm^{-1} to 2088 cm^{-1}). This may be due to the difference in the surface orientation (Pd–Sn (100) to Pd–Au (111)). Also any electronic effect, like charge transfers between Pd and Sn or Au, may also contribute to this difference. Further investigations about this issue are definitely needed. Moreover, a blue shift is observed in Fig. 66 when the surface CO coverage is increased on the Pd–Sn alloy surface. In the Pd–Au alloy system, the IR frequency for the isolated Pd sites is not shifted with the change of the surface CO coverage. This may be caused by the fact that the saturation CO coverage on the Pd–Sn alloy surface is higher than that of the Pd–Au surface. Therefore, dipole–dipole interactions from neighboring CO molecules induce this shift to higher frequencies, but further experiments are also demanded to confirm this explanation.

CO TPD was also used to further study the CO adsorption behavior on Pd–Sn alloy surface. In particular, the CO adsorption/desorption properties of the c(2x2) ordered Pd–Sn alloy surface were examined and compared with that of clean Rh(100) substrate, 4ML Pd, and 4ML Sn films. In Fig. 68, the saturation CO TPD spectra for all these surfaces were presented. The clean Rh(100) substrate gives a broad desorption feature ranging from 250 K to 500 K. Once 4ML Pd was deposited on Rh(100), this broad peak was completely quenched and replaced by a feature from 300 K to 450 K, indicating the 4ML Pd film wets the surface effectively. In terms of desorption temperature and

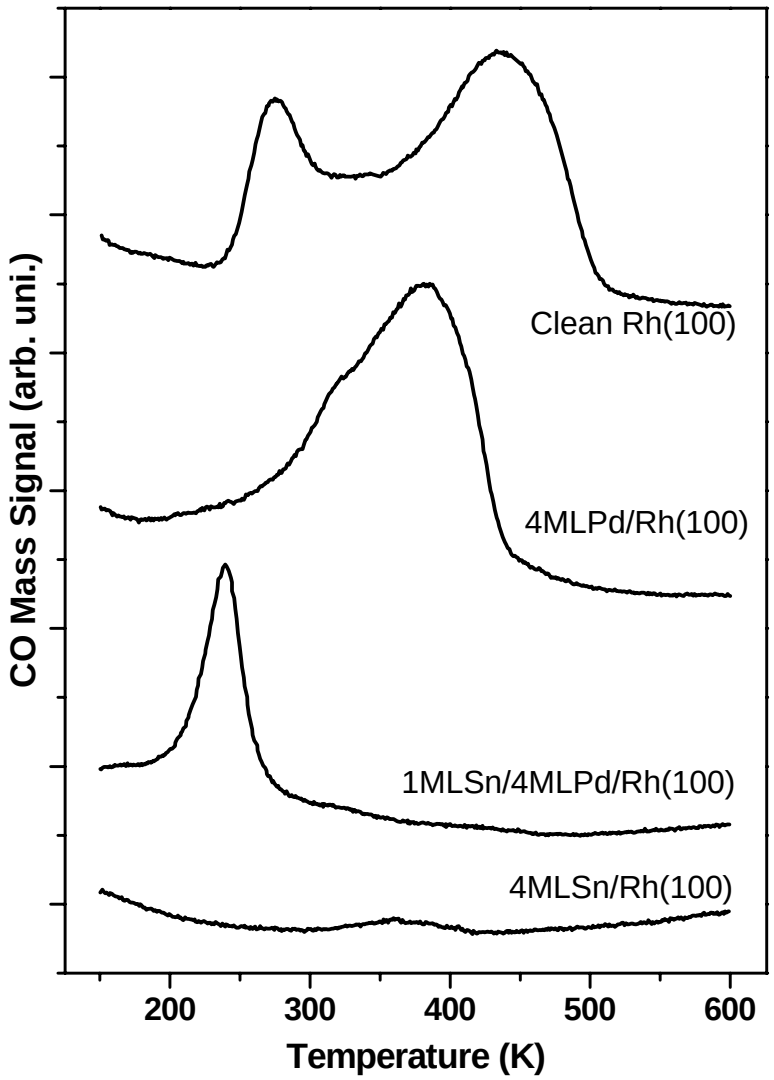

Fig. 68 Comparison of CO-TPD spectra for clean Rh(100), 4ML Pd film, 1ML Sn/4ML Pd alloy film, and 4ML Sn film on Rh(100). The alloy film was annealed at 700 K for 1 minute, and all the spectra represent saturation coverage.

feature shape, the CO TPD spectrum from 4ML Pd film is almost identical with that from Pd(100) single crystal.[39,171,172] This corresponds very well with the above LEED and CO-IRAS results, showing that the 4ML Pd film has a (100)-like surface orientation. As was pointed out in earlier discussions of CO-IRAS and TPD studies on different facets of Pd single crystal surfaces,[39,171,172] this feature can be assigned to the CO adsorption on Pd bridging sites. For the 1ML Sn/4ML Pd/Rh(100) alloy film annealed at 700 K, a sharp and symmetrical CO desorption feature at around 250 K is observed. This desorption temperature agrees very well with the above temperature dependent IRAS spectra (Fig. 66), indicating a much weaker CO adsorption site is formed on Pd–Sn alloy surfaces, i.e. the isolated Pd sites. The fact that this feature is so sharp and almost symmetrical is also in line with the formation of ordered Pd–Sn alloy structure. In addition, no significant CO desorption feature is observed for 4ML Sn film surfaces. The tiny peak noticed at around 350 K on this surface may arise from diffused surface Rh atoms, since it is well known that Sn can easily form alloys with Rh.

Acetylene Trimerization to Benzene

The cyclotrimerization of acetylene to benzene is a well-studied reaction on the low-index single-crystal Pd surfaces, which has received considerable attention since its discovery by Tysoe *et al.* and Sesselmann *et al.*[173-175] The reactivity of this reaction can be easily measured by just integrating the peak area of benzene TPD desorption features after adsorbing saturation acetylene on the surface at low temperature. In literature, this reaction has been shown to be a structure sensitive reaction with the Pd(111) facet being

the most active.[176,177] In the benzene TPD on Pd(111) surface, mainly two features at around 250 K and 500 K are observed. An additional intermediate feature is present for the Pd(100) surface just below 400 K. It is generally agreed that the high-temperature desorption feature (500 K) arises from benzene lying flat on the surface, while the low-temperature desorption feature (250 K) results from reactively formed benzene on an initially crowded surface that forces the benzene molecules into a weaker binding configuration with the molecular plane tilted with respect to the surface. The origin of the intermediate desorption feature at around 400 K has alternately been explained as desorption from a close–packed flat-bonded layer of benzene or from adsorption sites at defect sites.[178,179]

Even though the mechanism of benzene formation is not completely understood, it is generally believed that a critical ensemble size is required for acetylene trimerization to benzene. This possibility has been addressed by using Au/Pd(111) and Pd/Au(111) surface alloys and Au/Pd colloid particles.[132,180,181] In this series of work, it has been argued that an ensemble of seven Pd atoms or six Pd atoms with a central Au atom is required for benzene formation. Additionally, it was also concluded that a Pd ensemble involving a Au atom is more effective than a pure Pd ensemble, possibly by reducing decomposition as opposed to desorption of the reactively formed benzene.[182]

Therefore, it is interesting to examine the reactivity of the isolated Pd site for the acetylene trimerization reaction by utilizing our Pd–Au and Pd–Sn model alloy systems. The fact that both Sn and Au are essentially inert for this reaction even better serves the purpose of addressing the importance of certain Pd ensembles to the benzene formation.

Fig. 69 presents the benzene TPD spectra from acetylene adsorbed on 10ML Pd/Mo(110) film and Pd–Au/Mo(110) alloy films with different compositions. On 10ML Pd/Mo(110) film surfaces, two major desorption features resemble closely the literature-reported results, indicating once again the Pd film supported on Mo(110) adopts a mainly (111)-like orientation. The small shoulder appearing at around 400 K may arise from the desorption of small amounts of surface imperfection (i.e. some Pd (100) facets). The slight intensity at around 300 K stems mainly from the substrate Mo(110) desorption. Once Pd–Au alloy surfaces are formed, the two major desorption features on Pd film at 200 and 500 K are completely quenched. Instead, an intermediate peak centered at 350 K appears and grows in intensity by increasing the bulk Pd concentration. This clearly suggests that a totally different benzene formation mechanism occurs on the Pd–Au alloy surfaces.

In Fig. 70, the benzene TPD spectra from acetylene adsorbed on a clean Rh(100) surface, 4ML Pd/Rh(100) film, and Pd–Sn/Rh(100) alloy film with different compositions are displayed. Similarly, 4ML Pd/Rh(100) film surfaces resemble Pd(100) single crystal surfaces closely with three major benzene desorption features at around 200, 400, and 500 K observed. A small hump at around 300 K in this spectrum may arise from the benzene desorption of the substrate Rh(100) surface. Once the Pd–Sn alloy surfaces are formed, all these features from the Pd film surface are again completely suppressed and only one feature centered at 300 K is apparent. The intensity of this feature grows gradually as the Sn coverage increases and saturates when the Sn

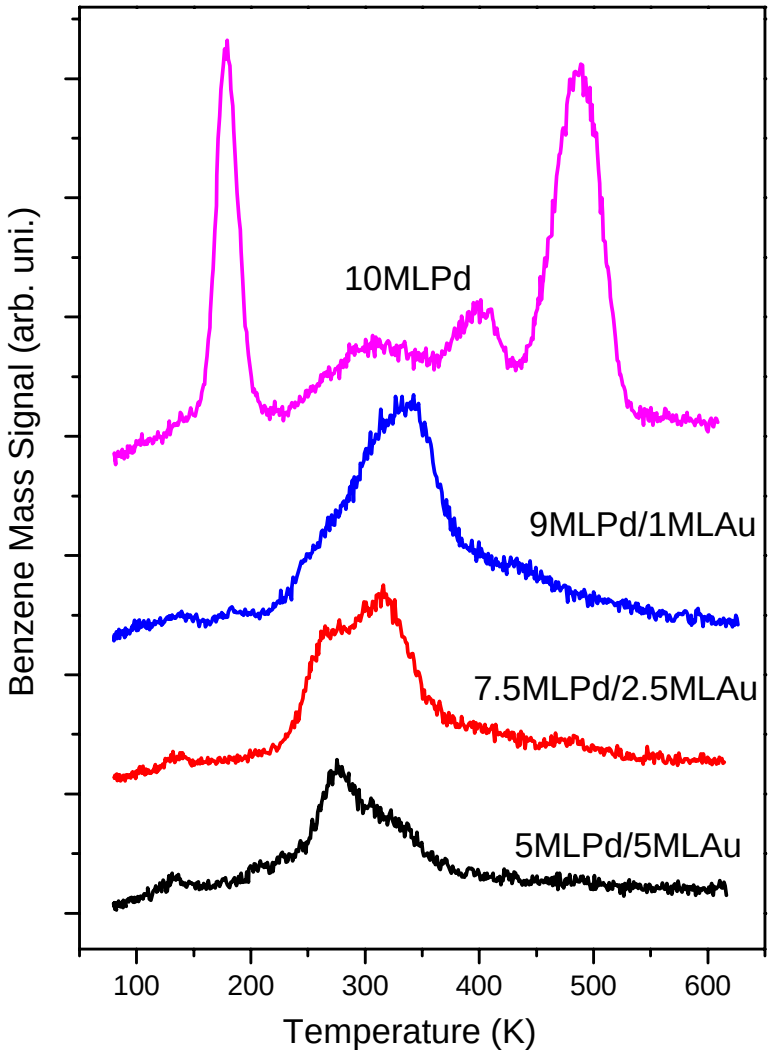

Fig. 69 TPD of benzene from acetylene adsorbed on 10ML Pd/Mo(110) film and Pd–Au/ Mo(110) alloy films with different compositions. Acetylene was exposed at 80 K, and 10 L was used in order to obtain saturation results. Each alloy surface was annealed at 800 K for 20 minutes prior to acetylene dosage.

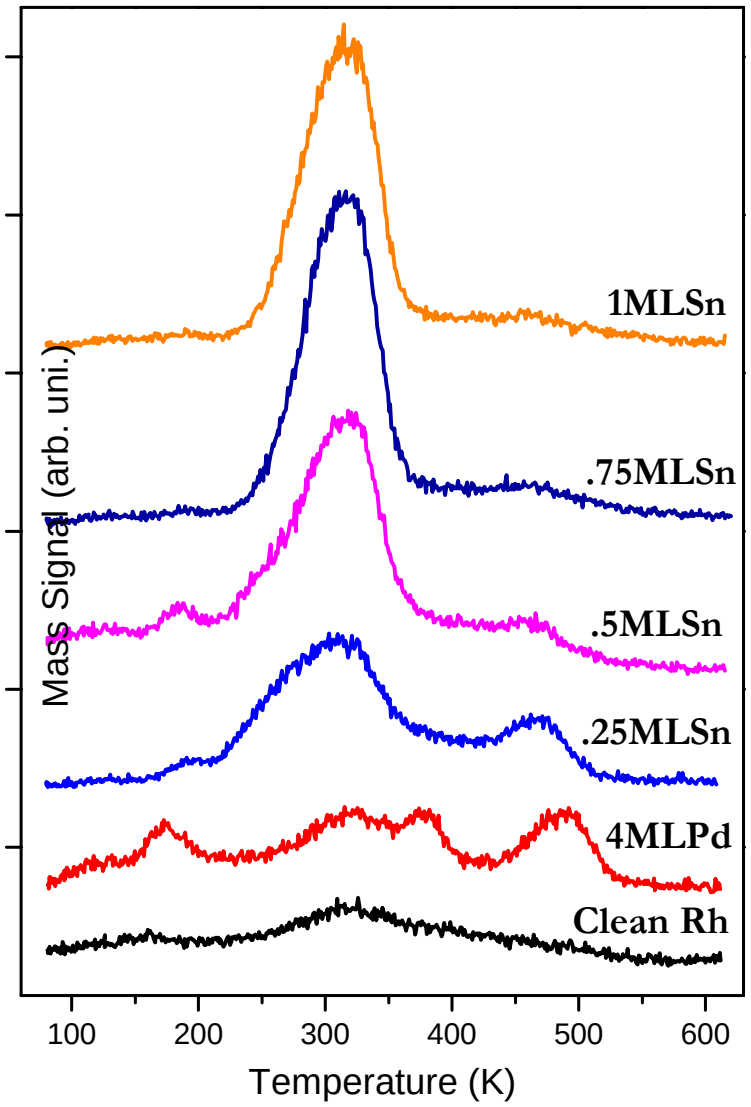

Fig. 70 TPD of benzene from acetylene adsorbed on clean Rh(100), 4ML Pd/Rh(100) film, and Pd–Sn/Rh(100) alloy films with different compositions. Acetylene was exposed at 80 K, and 10 L was used in order to obtain saturation results. Each alloy surface was annealed at 700 K for 1 minute prior to acetylene dosage.

coverage reaches between 0.5 to 0.75 ML. This corresponds with the above LEISS and LEED results very well in the way that at least 0.5 ML Sn is needed to form an ordered c(2×2) alloy structure. It is also interesting to notice that the benzene yield for the Pd–Sn alloy surface is increased significantly compared with the pure Pd film with (100) orientation. Given the fact that only about 50 % of surface atoms are Pd in an ordered c(2×2) Pd–Sn alloy surface, the reactivity of the isolated Pd sites (per Pd atom base) may be roughly a magnitude higher than that from Pd(100) surface. This clearly indicates that the isolated Pd site itself can do this reaction, and no certain Pd ensembles are needed.

In order to quantitatively compare the TPD results from these two sets of data, the different signal scales and sensitivity factors of mass spectrometer are considered and adjusted. The modified TPD spectra are summarized in a same scale and displayed in Fig. 71. As can be seen, the reactivity of Pd(111) surfaces is much higher than that of Pd(100) surfaces, which agrees with the previously reported literature-results that this reaction is structure–sensitive. Moreover, the TPD spectral features from 1ML Sn/4ML Pd/Rh(100) and 1ML Au/9ML Pd/Mo(110) alloy systems are quite close to each other in terms of the peak shape and intensity. It may be implied that similar benzene formation mechanism is shared on these two surfaces. Because both Sn and Au are essentially inert for the benzene formation and the surface orientation on these two surfaces are totally different, it is likely that only Pd atoms, more specifically the isolated Pd sites, are involved in the reaction. The desorption temperature of this single feature on alloy surfaces shifts to a higher value from Pd–Sn to Pd–Au alloy systems. Recalling the CO

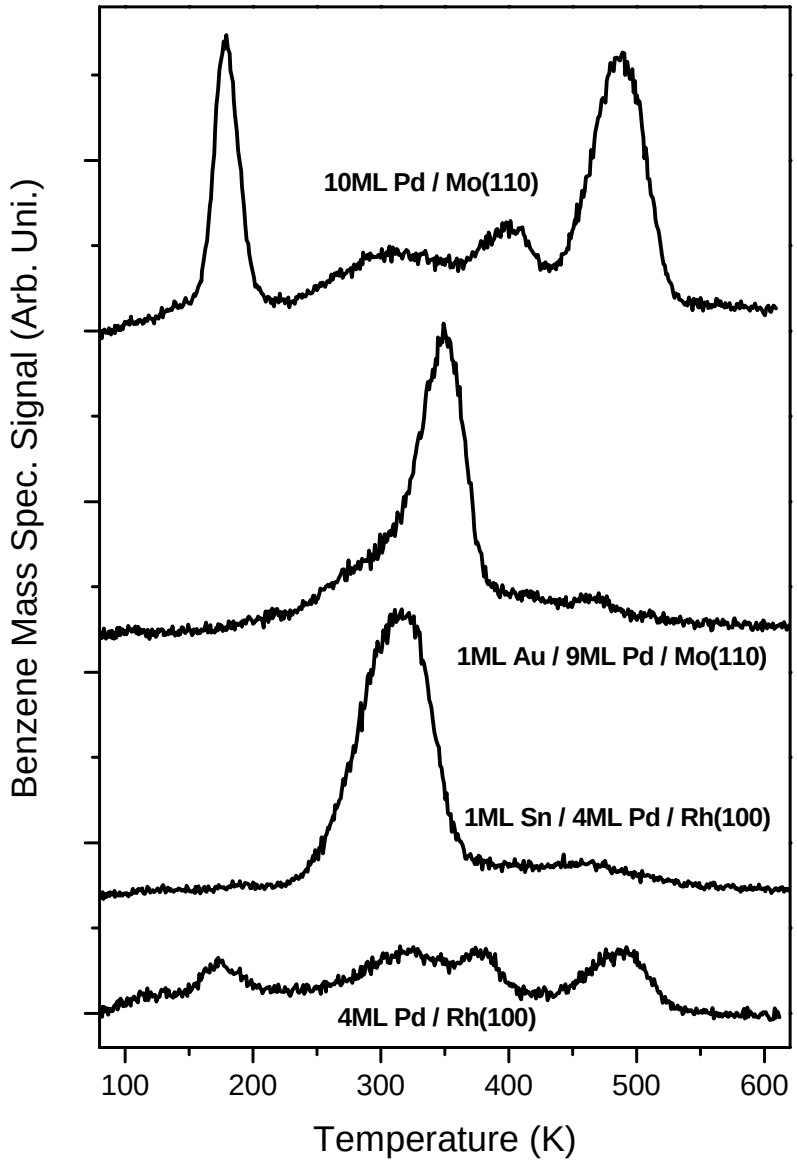

Fig. 71 Comparison of benzene TPD spectra from acetylene adsorbed on 10ML Pd/Mo(110) film, 4ML Pd/Rh(100) film, 1ML Sn/4ML Pd/Rh(100), and 1ML Au/9ML Pd/ Mo(110) alloy films. Acetylene was exposed at 80 K, and 10 L was used in order to obtain saturation results.

TPD experiments on Pd–Sn and Pd–Au surfaces, a higher temperature shift for the CO desorption feature was also observed from Pd–Sn to Pd–Au systems. This similarity in the changing trend of CO and benzene desorption temperatures probably indicates that these two molecules adsorb on the surface in a similar way. It is already known that the isolated Pd sites are responsible for the CO adsorption. Therefore, this may be another proof that the isolated Pd sites are the only critical reaction ensembles for the acetylene trimerization to benzene on the Pd–Sn and Pd–Au alloy surfaces.

In conclusion, the Pd–Sn bimetallic model catalysts were prepared as alloy films on a Rh(100) substrate via physical vapor deposition. The surface composition, structure, and chemi-adsorption properties were studied by low energy ion scattering spectroscopy (LEISS), low energy electron diffraction (LEED), X-ray photoelectron spectroscopy (XPS), infrared reflection adsorption spectroscopy (IRAS), and temperature programmed desorption (TPD). The formation of c(2×2) ordered surface alloy structure was observed after annealing the Pd–Sn mixtures to 700 K. LEIS results proved the surface Pd concentration at this stage is close to 50 %. With CO as a probe molecule, IRAS and TPD studies identified that all the Pd atoms on the surface are isolated by Sn. The TPD studies of acetylene to benzene reaction reveal that the isolated Pd sites are active to the benzene formation.

CONCLUSIONS

Extensive surface characterizations of SiO_2/Mo(112), Ag/SiO_2/Mo(112), Pd–Au/Mo(110), Pd–Au/SiO_2/Mo(110), and Pd–Sn/Rh(100) model catalyst systems have been carried out using a combination of metastable impact electron spectroscopy (MIES), ultraviolet photoelectron spectroscopy (UPS), low energy ion scattering spectroscopy (LEISS), X–ray photoelectron spectroscopy (XPS), low energy electron diffraction (LEED), infrared reflection absorption spectroscopy (IRAS), and temperature programmed desorption (TPD).

Particularly, MIES and UPS studies showed the electronic properties of SiO_2/Mo(112) thin films with the thickness of 0.7 – 0.8 nm are identical to those of bulk SiO_2. Additional energy states for various defect sites on SiO_2 surfaces were observed by MIES within the band gap region, whereas UPS showed only minor features that can be related to the presence of defect sites. Hence, low densities of defect sites on oxide surfaces, not detectable by other surface science techniques, can be measured with MIES. Extended defects were also identified by the broadening of the O(2p) band in MIES and UPS spectra. Moreover, MIES for adsorbed Xe (MAX) was shown to be useful for the identification and further quantification of defect sites.

The interaction between deposited Ag clusters and various types of defects on SiO_2 has also been investigated. MIES/UPS data for low and high defective SiO_2 surfaces acquired as a function of Ag exposure are consistent with 2-D Ag growth at low coverage and 3-D growth at higher Ag coverages. With increasing defect density on the

SiO_2 surfaces, no significant change was observed in the behavior of the work function with respect to the Ag coverage, suggesting that the interaction between Ag and SiO_2 is not influenced markedly by the presence of defects. This result is consistent with the recent theoretical calculations that indicate a strong covalent bond between an overlayer metal and defect sites of SiO_2.

Additionally, planar Pd-Au bimetallic model catalyst systems have been synthesized via physical vapor deposition on a Mo(110) substrate. The surface concentration, morphology, and chemical properties of these Pd-Au alloy films were determined by LEISS, CO-IRAS, and CO-TPD. Pd-Au mixtures can form a stable alloy between 700 and 1000 K with substantial enrichment in Au compared to the bulk composition. Annealing a 1:1 Pd-Au mixture at 800 K led to the formation of a surface alloy with a composition $Au_{0.8}Pd_{0.2}$ where Pd is predominantly surrounded by Au. Alloying effects, including geometric ensemble effect and electronic ligand effect, were addressed by examining the differences in the corresponding CO-IRAS spectra. A unique CO vibrational feature at 2088 cm^{-1} was identified as the CO adsorption on the isolated Pd sites, indicating the presence of an ensemble effect. On the other hand, no conclusive indications of the electronic ligand effect were found in the CO stretching frequency. The surface concentration of this isolated Pd site can be controlled systematically by altering the bulk Pd-Au alloy composition, which allows the further studies of the properties of this isolated Pd site in catalytic reactions.

The growth of Pd-Au alloy clusters via a sequential deposition and annealing on amorphous ultra-thin SiO_2 films has been also investigated by LEISS. The surface

composition of the Pd-Au clusters was shown to be Au-rich compared to the bulk of the cluster as observed previously for planar Pd-Au surfaces. However, the extent of Au enrichment is less for the Pd-Au clusters compared to the extended surfaces. The CO adsorption behavior on Pd-Au alloy clusters was examined by TPD and IRAS. The isolated Pd sites were identified as a unique surface ensemble. Moreover, a thermodynamically stable alloy system can be prepared after annealing at 800 K regardless of the opposite deposition order.

Furthermore, the Pd–Sn bimetallic alloy films grown on a Rh(100) substrate were studied by LEED, LEISS, CO-TPD, and CO-IRAS. The formation of c(2×2) ordered surface alloy structure was observed after annealing the Pd–Sn mixtures to 700 K. LEISS results proved the surface Pd concentration at this stage is close to 50 %. CO-IRAS and TPD studies identified all the Pd atoms on the surface are isolated by Sn. The TPD studies of acetylene to benzene reaction reveal that the isolated Pd sites are active to the benzene formation.

In this dissertation, several model catalyst systems were synthesized and characterized using various surface science techniques under UHV condition. Particularly, the approach of growing bimetallic overlayers on a third metal substrate (or an oxide support) offers a new methodology to conveniently synthesize bimetallic model catalysts with different surface vs. bulk compositions. From the observation of isolated Pd sites on disordered Pd-Au alloy surfaces to the preparation of ordered Pd-Sn alloy surfaces with perfect Pd monomers, this study shows a clear pathway for developing and designing new model catalyst systems for further atomic-level investigations. This

offers potential opportunities for investigating a spectrum of mixed-metal systems and how their surface structures relate to catalytic functions.

REFERENCES AND NOTES

(1) Somorjai, G. A. *Introduction to Surface Chemistry and Catalysis*; John Wiley & Sons, Inc.; New York; 1994.

(2) Kolasinski, K. W. *Surface Science, Foundations of Catalysis and Nanoscience*; John Wiley & Sons Ltd.; Chichester; 2002.

(3) Goodman, D. W. *Chemical Reviews* **1995**, *95*, 523.

(4) Goodman, D. W. *Journal of Physical Chemistry* **1996**, *100*, 13090.

(5) Goodman, D. W. *Journal of Catalysis* **2003**, *216*, 213.

(6) Ozensoy, E. *Polarization Modulation Infrared Reflection Absorption Spectroscopy for Heterogeneous Catalytic Applications at Elevated Pressures*; Ph. D. dissertation; Texas A&M University; College Station; 2004.

(7) Henrich, V. E.; Cox, P. A. *The Surface Science of Metal Oxides*; Cambridge University Press; Cambridge; 1994.

(8) Xu, X. P.; Vesecky, S. M.; Goodman, D. W. *Science* **1992**, *258*, 788.

(9) Ahmed, S. I. U.; Perry, S. S.; El-Bjeirami, O. *Journal of Physical Chemistry B* **2000**, *104*, 3343.

(10) Stirniman, M. J.; Huang, C.; Smith, R. S.; Joyce, S. A.; Kay, B. D. *Journal of Chemical Physics* **1996**, *105*, 1295.

(11) Wu, M. C.; Truong, C. M.; Coulter, K.; Goodman, D. W. *Journal of the American Chemical Society* **1992**, *114*, 7565.

(12) Sanchez, A.; Abbet, S.; Heiz, U.; Schneider, W. D.; Hakkinen, H.; Barnett, R. N.; Landman, U. *Journal of Physical Chemistry A* **1999**, *103*, 9573.

(13) Valden, M.; Lai, X.; Goodman, D. W. *Science* **1998**, *281*, 1647.

(14) Wahlstrom, E.; Lopez, N.; Schaub, R.; Thostrup, P.; Ronnau, A.; Africh, C.; Laegsgaard, E.; Norskov, J. K.; Besenbacher, F. *Physical Review Letters* **2003**, *90*.

(15) Henrich, V. E.; Kurtz, R. L. *Journal of Vacuum Science & Technology* **1981**, *18*, 416.

(16) Wu, M. C.; Truong, C. M.; Goodman, D. W. *Physical Review B* **1992**, *46*, 12688.

(17) Sinfelt, J. H. *Bimetallic Catalysts*; Wiley; New York; 1983.

(18) Jablonski, A.; Overbury, S. H.; Somorjai, G. A. *Surface Science* **1977**, *65*, 578.

(19) Kuntze, J.; Speller, S.; Heiland, W.; Atrei, A.; Rovida, G.; Bardi, U. *Physical Review B* **1999**, *60*, 1535.

(20) Kuntze, J.; Speller, S.; Heiland, W.; Deurinck, P.; Creemers, C.; Atrei, A.; Bardi, U. *Physical Review B* **1999**, *60*, 9010.

(21) Swartzfager, D. G.; Ziemecki, S. B.; Kelley, M. J. *Journal of Vacuum Science & Technology* **1982**, *19*, 185.

(22) Baddeley, C. J.; Ormerod, R. M.; Stephenson, A. W.; Lambert, R. M. *Journal of Physical Chemitry* **1995**, *99*, 5146.

(23) Baddeley, C. J.; Tikhov, M.; Hardacre, C.; Lomas, J. R.; Lambert, R. M. *Journal of Physical Chemistry* **1996**, *100*, 2189.

(24) Gleich, B.; Ruff, M.; Behm, R. J. *Surface Science* **1997**, *386*, 48.

(25) Koel, B. E.; Sellidj, A.; Paffett, M. T. *Physical Review B* **1992**, *46*, 7846.

(26) Ruff, M.; Frey, S.; Gleich, B.; Behm, R. J. *Applied Physics a-Materials Science & Processing* **1998**, *66*, S513.

(27) Rainer, D. R.; Wu, M. C.; Mahon, D. I.; Goodman, D. W. *Journal of Vacuum Science & Technology A* **1996**, *14*, 1184.

(28) Sadigh, B.; Asta, M.; Ozolins, V.; Schmid, A. K.; Bartelt, N. C.; Quong, A. A.; Hwang, R. Q. *Physical Review Letters* **1999**, *83*, 1379.

(29) Storm, J.; Lambert, R. M.; Memmel, N.; Onsgaard, J.; Taglauer, E. *Surface Science* **1999**, *436*, 259.

(30) Maehara, Y.; Kawanowa, H.; Gotoh, Y. *Surface Review Letters* **2003**, *10*, 425.

(31) Pavlovska, A.; Paunov, M.; Bauer, E. *Thin Solid Films* **1985**, *226*, 39.

(32) Maroun, F.; Ozanam, F.; magnussen, O. M.; Behm, R. J. *Science* **2001**, *293*, 1811.

(33) Guauthier, Y.; Schmid, M.; Padovani, S.; Lundgren, E.; Bus, V.; Kresse, G.; Redinger, J.; Varga, P. *Physical Review Letters* **2001**, *87*, 036103.

(34) Kugler, E. L.; Boudart, M. *Journal of Catalysis* **1979**, *59*, 201.

(35) Gottfried, J. M.; Schnidt, K. J.; Schroeder, S. L. M.; Christmann, K. *Surface Science* **2003**, *536*, 206.

(36) Guo, X.; Yates, J. T. *Journal of Physical Chemistry* **1989**, *90*, 6761.

(37) Hoffmann, F. M. *Surface Science Reports* **1983**, *3*, 107.

(38) Jugnet, Y.; Cadet Santos Aires, F. J.; Deranlot, C.; Piccolo, L.; Bertolini, J. C. *Surface Science* **2002**, *521*, L639.

(39) Kuhn, W. K.; Szanyi, J.; Goodman, D. W. *Surface Science Letters* **1992**, *274*, L611.

(40) Meier, D. C.; Bukhtiyarov, V.; Goodman, D. W. *Journal of Physical Chemistry B* **2003**, *107*, 12668.

(41) Ozensoy, E.; Goodman, D. W. *Physical Chemistry Chemical Physics* **2004**, *6*, 3765.

(42) Ruggiero, C.; Hollins, P. *Journal of Chemical Society. Faraday Transactions* **1996**, *92*, 4829.

(43) Szanyi, J.; Kuhn, W. K.; Goodman, D. W. *Journal of Vacuum Science & Technology A* **1993**, *11*, 1969.

(44) Maus-Friedrichs, W.; Dieckhoff, S.; Kempter, V. *Surface Science* **1991**, *249*, 149.

(45) Maus-Friedrichs, W.; Wehrhahn, M.; Dieckhoff, S.; Kempter, V. *Surface Science* **1990**, *237*, 257.

(46) Attard, G.; Barnes, C. *Surface*; Oxford University Press Inc.; New York; 1998.

(47) Ertl, G.; Kuppers, J. *Low energy electrons and surface chemistry*; VCH; Weinheim; 1985.

(48) Harada, Y.; Masuda, S.; Ozaki, H. *Chemical Reviews* **1997**, *97*, 1897.

(49) Niehus, H.; Heiland, W.; Taglauer, E. *Surface Science Reports* **1993**, *17*, 213.

(50) Leung, L. W. H.; He, J. W.; Goodman, D. W. *The Journal of Chemical Physics* **1990**, *93*, 8328.

(51) Xueping, X.; Goodman, D. W. *Applied Physics Letters* **1992**, *61*, 774.

(52) Schroeder, T.; Adelt, M.; Richter, B.; Naschitzki, M.; Baumer, M.; Freund, H. J. *Surface Review and Letters* **2000**, *7*, 7.

(53) Schroeder, T.; Hammoudeh, A.; Pykavy, M.; Magg, N.; Adelt, M.; Baumer, M.; Freund, H. J. *Solid-State Electronics* **2001**, *45*, 1471.

(54) Kim, Y. D.; Wei, T.; Goodman, D. W. *Langmuir* **2003**, *19*, 354.

(55) Dipomponio, A.; Continenza, A.; Lozzi, L.; Passacantando, M.; Santucci, S.; Picozzi, P. *Solid State Communications* **1995**, *95*, 313.

(56) Schintke, S.; Messerli, S.; Pivetta, M.; Patthey, F.; Libioulle, L.; Stengel, M.; De Vita, A.; Schneider, W. D. *Physical Review Letters* **2001**, *87*.

(57) Ochs, D.; Braun, B.; Maus-Friedrichs, W.; Kempter, V. *Surface Science* **1998**, *417*, 406.

(58) Pacchioni, G.; Ierano, G. *Physical Review B* **1998**, *57*, 818.

(59) Kim, Y. D.; Stultz, J.; Goodman, D. W. *Langmuir* **2002**, *18*, 3999.

(60) Kim, Y. D.; Stultz, J.; Goodman, D. W. *Surface Science* **2002**, *506*, 228.

(61) Boscaino, R.; Cannas, M.; Gelardi, F. M.; Leone, M. *Journal of Physics-Condensed Matter* **1996**, *8*, L545.

(62) Boscaino, R.; Cannas, M.; Gelardi, F. M.; Leone, M. *Physical Review B* **1996**, *54*, 6194.

(63) Guzzi, M.; Pio, F.; Spinolo, G.; Vedda, A.; Azzoni, C. B.; Paleari, A. *Journal of Physics-Condensed Matter* **1992**, *4*, 8635.

(64) Miller, A. J.; Leisure, R. G.; Mashkov, V. A.; Galeener, F. L. *Physical Review B* **1996**, *53*, R8818.

(65) Nishikawa, H.; Watanabe, E.; Ito, D.; Ohki, Y. *Physical Review Letters* **1994**, *72*, 2101.

(66) Nishikawa, N.; Miyake, Y.; Watanabe, E.; Ito, D.; Seol, K. S.; Ohki, Y.; Ishii, K.; Sakurai, Y.; Nagasawa, K. *Journal of Non-Crystalline Solids* **1997**, *222*, 221.

(67) Pacchioni, G.; L., S.; D.L., G. *Defects in SiO_2 and Related Dielectrics : Science and Technology*, *NATO Science Series 2002*.

(68) Trukhin, A. N.; Goldberg, M.; Jansons, J.; Fitting, H. J.; Tale, I. A. *Journal of Non-Crystalline Solids* **1998**, *223*, 114.

(69) Pacchioni, G.; Ierano, G. *Physical Review Letters* **1997**, *79*, 753.

(70) Pacchioni, G.; Ierano, G. *Physical Review B* **1997**, *56*, 7304.

(71) Pacchioni, G.; Ierano, G. *Journal of Non-Crystalline Solids* **1997**, *216*, 1.

(72) Pacchioni, G.; Ierano, G.; Marquez, A. M. *Physical Review Letters* **1998**, *81*, 377.

(73) Uchino, T.; Takahashi, M.; Yoko, T. *Physical Review Letters* **2001**, *86*, 4560.

(74) Uchino, T.; Takahashi, M.; Yoko, T. *Physical Review Letters* **2001**, *86*, 5522.

(75) Kolmakov, A.; Stultz, J.; Goodman, D. W. *Journal of Chemical Physics* **2000**, *113*, 7564.

(76) Tegenkamp, C.; Pfnur, H.; Ernst, W.; Malaske, U.; Wollschlager, J.; Peterka, D.; Schroder, K. M.; Zielasek, V.; Henzler, M. *Journal of Physics-Condensed Matter* **1999**, *11*, 9943.

(77) Jablonski, A.; Wandelt, K. *Surface Science* **1991**, *251*, 650.

(78) Wandelt, K. *Applied Surface Science* **1997**, *111*, 1.

(79) Hulse, J.; Kuppers, J.; Wandelt, K.; Ertl, G. *Applied Surface Science* **1980**, *6*, 453.

(80) Kim, Y. D.; Stultz, J.; Wei, T.; Goodman, D. W. *Journal of Physical Chemistry B* **2002**, *106*, 6827.

(81) Lopez, N.; Illas, F.; Pacchioni, G. *Journal of Physical Chemistry B* **1999**, *103*, 1712.

(82) Lopez, N.; Illas, F.; Pacchioni, G. *Journal of the American Chemical Society* **1999**, *121*, 813.

(83) Pacchioni, G.; Lopez, N.; Illas, F. *Faraday Discussions* **1999**, 209.

(84) Baumer, M.; Frank, M.; Heemeier, M.; Kuhnemuth, R.; Stempel, S.; Freund, H. J. *Surface Science* **2000**, *454*, 957.

(85) Haas, G.; Menck, A.; Brune, H.; Barth, J. V.; Venables, J. A.; Kern, K. *Physical Review B* **2000**, *61*, 11105.

(86) Abbet, S.; Sanchez, A.; Heiz, U.; Schneider, W. D.; Ferrari, A. M.; Pacchioni, G.; Rosch, N. *Journal of the American Chemical Society* **2000**, *122*, 3453.

(87) Heiz, U.; Schneider, W. D. *Journal of Physics D-Applied Physics* **2000**, *33*, R85.

(88) de Oliveira, A. L.; Wolf, A.; Schuth, F. *Catalysis Letters* **2001**, *73*, 157.

(89) Stracke, P.; Krischok, S.; Kempter, V. *Surface Science* **2001**, *473*, 86.

(90) Campbell, C. T. *Surface Science Reports* **1997**, *27*, 1.

(91) Ernst, K. H.; Ludviksson, A.; Zhang, R.; Yoshihara, J.; Campbell, C. T. *Physical Review B* **1993**, *47*, 13782.

(92) Onishi, H.; Aruga, T.; Egawa, C.; Iwasawa, Y. *Surface Science* **1990**, *233*, 261.

(93) Komiyama, M.; Shimaguchi, T. *Surface and Interface Analysis* **2001**, *32*, 189.

(94) Xu, X. P.; Szanyi, J.; Xu, Q.; Goodman, D. W. *Catalysis Today* **1994**, *21*, 57.

(95) Ferrari, A. M.; Pacchioni, G. *Journal of Physical Chemistry* **1996**, *100*, 9032.

(96) Rodriguez, J. A. *Surface Science Reports* **1996**, *24*, 223.

(97) Rodriguez, J. A.; Goodman, D. W. *Science* **1992**, *257*, 897.

(98) Besenbacher, F.; Chorkendorff, I.; Clausen, B. S.; Hammer, B.; Molenbroek, A. M.; Norskov, J. K.; Stensgaard, I. *Science* **1998**, *279*, 1913.

(99) Sachlter, J. W. A.; Van Hove, M. A.; Biberian, J. P.; Somorjai, G. A. *Physical Review Letters* **1980**, *45*, 1601.

(100) Han, Y. F.; Wang, J. H.; Kumar, D.; Yan, Z.; Goodman, D. W. *Journal of Catalysis* **2005**, *232*, 467.

(101) Provine, W. D.; Mills, P. L.; Lerou, J. J. *Studies in Surface Science and Catalysis* **1996**, *101*, 191.

(102) Stacchiola, D.; Calaza, F.; Burkholder, L.; Tysoe, W. T. *Journal of American Chemical Society* **2004**, *126*, 15384.

(103) Yi, C. W.; Luo, K.; Wei, T.; Goodman, D. W. *Journal of Physical Chemistry B* **2005**, *109*, 18335.

(104) Gruzza, B.; Gillet, E. *Thin Solid Films* **1980**, *126*, 129.

(105) Park, C.; Bauer, E.; Poppa, H. *Surface Science* **1985**, *154*, 371.

(106) Payne, S. H.; Kreuzer, H. J.; Pavlovska, A.; Bauer, E. *Surface Science* **1996**, *345*, L1.

(107) Anton, R.; Eggers, H.; Veltas, J. *Thin Solid Films* **1993**, *226*, 39.

(108) Aschoff, M.; Speller, S.; Kuntze, J.; Heiland, W.; Platzgummer, E.; Schmid, M.; Varga, P.; Baretzky, B. *Surface Science* **1998**, *415*, L1051.

(109) Varga, P.; Hetzendorf, G. *Surface Science* **1985**, *162*, 544.

(110) Lee, Y. S.; Joen, Y.; Chung, Y. D.; Lim, K. Y.; Whang, C. N.; Oh, S. J. *Journal of Korean Physical Society* **2000**, *37*, 451.

(111) Nascente, P. A. P.; Decastro, S. G. C.; Landers, R.; Kleiman, G. G. *Physical Review B* **1991**, *43*, 4659.

(112) Weissman-Wenocur, D. L.; Stefan, P. M.; Pate, B. B.; Shek, M. L.; Lindau, I.; Spicer, W. E. *Physical Review B* **1983**, *27*, 3308.

(113) Piccolo, L.; Piednoir, A.; Bertolini, J. C. *Surface Science* **2005**.

(114) Chen, M. S.; Kumar, D.; Yi, C. W.; Goodman, D. W. *Science* **2005**.

(115) Rodriguez, J. A.; Campbell, R. A.; Goodman, D. W. *Journal of Physical Chemistry* **1991**, *95*, 5716.

(116) Sellidj, A.; Koel, B. E. *Physical Review B* **1994**, *49*, 8367.

(117) Shih, H. D.; Bauer, E.; Poppa, H. *Thin Solid Films* **1982**, *88*, L121.

(118) Mezey, L. Z.; Giber, J. *Japanese Journal of Applied Physics Part 1-Regular Papers Short Notes & Review Papers* **1982**, *21*, 1569.

(119) Swartzfager, D. G.; Ziemecki, S. B.; Kelley, M. J. *Journal of Vacuum Science & Technology* **1981**, *19*, 185.

(120) Mikkelesen, A.; Ouattara, L.; Lundgren, E. *Surface Science* **2004**, *557*.

(121) Giebel, T.; Schaff, O.; Hirschmugl, C. J.; Fernandez, V.; Schindler, K. M.; theobald, A.; Bao, S.; Lindsay, R.; Berndt, W.; Bradshaw, A. M.; Baddeley, C.; Lee, A. F.; Larbert, R. M.; Woodruff, D. P. *Surface Science* **1998**, *406*, 90.

(122) Rose, M. K.; Mitsui, T.; Dunphy, J.; Borg, A.; Ogletree, D. F.; Salmeron, M.; Sautet, P. *Surface Science* **2002**, *512*, 48.

(123) Ozensoy, E.; Meier, D. C.; Goodman, D. W. *Journal of Physical Chemistry B* **2002**, *106*, 9367.

(124) Bourguignon, B.; Carrez, S.; Dragnea, B.; Dubost, H. *Surface Science* **1998**, *418*, 171.

(125) Wei, T.; Goodman, D. W., in preparation.

(126) Xu, C.; Goodman, D. W. *Surface Science* **1996**, *360*, 249.

(127) Chen, M. S.; Cai., Y.; Yan, Z.; Goodman, D. W. in preparation.

(128) Meier, D. C.; Bukhtiyarov, V.; Goodman, D. W. *Journal of Physical Chemistry* **2003**, *107*, 12668.

(129) Meier, D. C.; Goodman, D. W. *Journal of American Chemical Society* **2004**, *126*, 1892.

(130) Aaen, A. B.; Lagsgaard, E.; Ruban, A. V.; Stensgaard, I. *Surface Science* **1998**, *408*, 43.

(131) Bennett, R. A.; Poulston, S.; Price, N. J.; Reilly, J. P.; Barnes, C. J.; Bowker, M. *Surface Science* **1999**, *433-435*, 816.

(132) Baddeley, C. J.; Tikhov, M.; Hardacre, C.; Lomas, J. R.; Lambert, R. M. *Journal of Physical Chemistry* **1996**, *100*, 2189.

(133) Engelhardt, M. P.; Schmid, M.; Biedermann, A.; Denecke, R.; Steinruck, H. P.; Varga, P. *Surface Science* **2005**, *578*, 124.

(134) Gauthier, Y.; Schmid, M.; Padovani, S.; Lundgren, E.; Bus, V.; Kresse, G.; Redinger, J.; Varga, P. *Physical Review Letters* **2001**, *8703*.

(135) Rutten, F. J. M.; Nieuwenhuys, B. E.; McCoustra, M. R. S.; Chesters, M. A.; Hollins, P. *Journal of Vacuum Science & Technology A* **1997**, *15*, 1619.

(136) Pantforder, A.; Skonieczny, J.; Janssen, E.; Meister, G.; Goldmann, A.; Varga, P. *Surface Science* **1995**, *333*, 824.

(137) Pantforder, A.; Skonieczny, J.; Janssen, E.; Meister, G.; Goldmann, A.; Varga, P. *Surface Science* **1995**, *337*, 177.

(138) Schmid, M.; Stadler, H.; Varga, P. *Physical Review Letters* **1993**, *70*, 1441.

(139) Weigand, P.; Hofer, W.; Varga, P. *Surface Science* **1993**, *287*, 350.

(140) Pfnur, H.; Menzel, D.; Hoffmann, F. M.; Ortega, A.; Bradshaw, A. M. *Surface Science* **1980**, *93*, 431.

(141) Davis, R. J.; Boudart, M. *Journal of Physical Chemistry* **1994**, *98*, 5471.

(142) Kaszkur, Z. *Physical Chemistry Chemical Physics* **2004**, *6*, 193.

(143) Reifsnyder, S. N.; Lamb, H. H. *Journal of Physical Chemistry B* **1999**, *103*, 321.

(144) Luo, K.; Kim, D. Y.; Goodman, D. W. *Journal of Molecular Catalysis a-Chemical* **2001**, *167*, 191.

(145) Min, B. K.; Santra, A. K.; Goodman, D. W. *Journal of Vacuum Science & Technology B* **2003**, *21*, 2319.

(146) Min, B. K.; Santra, A. K.; Goodman, D. W. *Catalysis Today* **2003**, *85*, 113.

(147) Min, B. K.; Wallace, W. T.; Santra, A. K.; Goodman, D. W. *Journal of Physical Chemistry B* **2004**, *108*, 16339.

(148) Carlsson, A. F.; Naschitzki, M.; Baumer, M.; Freund, H. J. *Journal of Physical Chemistry B* **2003**, *107*, 778.

(149) Unterhalt, H.; Rupprechter, G.; Freund, H. J. *Journal of Physical Chemistry B* **2002**, *106*, 356.

(150) Wolter, K.; Seiferth, O.; Kuhlenbeck, H.; Baumer, M.; Freund, H. J. *Surface Science* **1998**, *399*, 190.

(151) Lemire, C.; Meyer, R.; Shaikhutdinov, S. K.; Freund, H. J. *Surface Science* **2004**, *552*, 27.

(152) Gelin, P.; Siedle, A. R.; Yates, J. T. *Journal of Physical Chemistry* **1984**, *88*, 2978.

(153) Overbury, S. H.; Mullins, D. R.; Paffett, M. T.; Koel, B. E. *Surface Science* **1991**, *254*, 45.

(154) Paffett, M. T.; Gebhard, S. C.; Windham, R. G.; Koel, B. E. *Journal of Physical Chemistry* **1990**, *94*, 6831.

(155) Paffett, M. T.; Logan, A. D.; Simonson, R. J.; Koel, B. E. *Surface Science* **1991**, *250*, 123.

(156) Paffett, M. T.; Windham, R. G. *Surface Science* **1989**, *208*, 34.

(157) Hayden, B. E.; Rendall, M. E.; South, O. *Journal of the American Chemical Society* **2003**, *125*, 7738.

(158) Peck, J. W.; Koel, B. E. *Journal of the American Chemical Society* **1996**, *118*, 2708.

(159) Rodriguez, J. A.; Jirsak, T.; Chaturvedi, S.; Hrbek, J. *Journal of the American Chemical Society* **1998**, *120*, 11149.

(160) Stamenkovic, V. R.; Arenz, M.; Lucas, C. A.; Gallagher, M. E.; Ross, P. N.; Markovic, N. M. *Journal of the American Chemical Society* **2003**, *125*, 2736.

(161) Szanyi, J.; Paffett, M. T. *Journal of the American Chemical Society* **1995**, *117*, 1034.

(162) Xu, C.; Peck, J. W.; Koel, B. E. *Journal of the American Chemical Society* **1993**, *115*, 751.

(163) Hamm, G.; Schmidt, T.; Breitbach, J.; Franke, D.; Becker, C.; Wandelt, K. *Surface Science* **2004**, *562*, 170.

(164) Lee, A. F.; Baddeley, C. J.; Tikhov, M. S.; Lambert, R. M. *Surface Science* **1997**, *373*, 195.

(165) Logan, A. D.; Paffett, M. T. *Journal of Catalysis* **1992**, *133*, 179.

(166) Tsud, N.; Skala, T.; Sutara, F.; Veltruska, K.; Dudr, V.; Fabik, S.; Sedlacek, L.; Chab, V.; Prince, K. C.; Matolin, V. *Surface Science* **2005**, *595*, 138.

(167) Luo, K.; Wei, T.; Yi, C. W.; Axnanda, S.; Goodman, D. W. *Journal of Physical Chemistry B* **2005**, *109*, 23517.

(168) Yi, C. W.; Luo, K.; Wei, T.; Goodman, D. W. *Journal of Physical Chemistry B* **2005**, *109*, 18535.

(169) Wei, T.; Wang, J. H.; Goodman, D. W. in preparation.

(170) Haner, A. N.; Ross, P. N.; Bardi, U. *Surface Science* **1991**, *249*, 15.

(171) Szanyi, J.; Kuhn, W. K.; Goodman, D. W. *Journal of Vacuum Science & Technology a-Vacuum Surfaces and Films* **1993**, *11*, 1969.

(172) Ortega, A.; Huffman, F. M.; Bradshaw, A. M. *Surface Science* **1982**, *119*, 79.

(173) Sesselmann, W.; Woratschek, B.; Ertl, G.; Kuppers, J.; Haberland, H. *Surface Science* **1983**, *130*, 245.

(174) Tysoe, W. T.; Nyberg, G. L.; Lambert, R. M. *Journal of the Chemical Society-Chemical Communications* **1983**, 623.

(175) Tysoe, W. T.; Nyberg, G. L.; Lambert, R. M. *Surface Science* **1983**, *135*, 128.

(176) Gentle, T. M.; Muetterties, E. L. *Journal of Physical Chemistry* **1983**, *87*, 2469.

(177) Rucker, T. G.; Logan, M. A.; Gentle, T. M.; Muetterties, E. L.; Somorjai, G. A. *Journal of Physical Chemistry* **1986**, *90*, 2703.

(178) Ormerod, R. M.; Baddeley, C. J.; Lambert, R. M. *Surface Science* **1991**, *259*, L709.

(179) Tysoe, W. T.; Ormerod, R. M.; Lambert, R. M.; Zgrablich, G.; Ramirezcuesta, A. *Journal of Physical Chemistry* **1993**, *97*, 3365.

(180) Baddeley, C. J.; Ormerod, R. M.; Stephenson, A. W.; Lambert, R. M. *Journal of Physical Chemistry* **1995**, *99*, 5146.

(181) Lee, A. F.; Baddeley, C. J.; Hardacre, C.; Ormerod, R. M.; Lambert, R. M.; Schmid, G.; West, H. *Journal of Physical Chemistry* **1995**, *99*, 6096.

(182) Ormerod, R. M.; Lambert, R. M. *Journal of Physical Chemistry* **1992**, *96*, 8111.

VITA

Tao Wei
Department of Chemistry
Texas A&M University
College Station, TX 77843-3255

EDUCATION

2001-2006 Texas A&M University, College Station, Texas
Ph. D. Chemistry

1996-2001 University of Science & Technology of China, Hefei, Anhui, China
B. S. Chemistry

SELECTED PUBLICATIONS

Wei, T.; Wang, J. H.; Goodman, D. W. "The chemical properties of Pd–Au alloy surfaces", in preparation.

Wei, T.; Luo, K.; Axnanda, S.; Goodman, D. W. "The chemical properties of Pd–Sn alloy surfaces", in preparation.

Wei, T.; Luo, K.; Yi, C. W.; Goodman, D. W. "Acetylene trimerization to benzene on isolate Pd sites", in preparation.

Luo, K.; **Wei, T**.; Yi, C.-W.; Axnanda, S.; Goodman, D.W. "Preparation and characterization of silica supported Au-Pd model catalysts." *Journal of Physical Chemistry B* **2005**, 109, 23517.

Yi, C.-W.; Luo, K.; **Wei, T;** Goodman, D.W. "Surface composition and structure of Pd - Au surfaces." *Journal of Physical Chemistry B* **2005**,109,18535.

Chen, M. S.; Luo, K.; **Wei, T.**; Yan, Z.; Kumar, D.; Yi, C.-W.; Goodman, D. W. "The nature of the active site for vinyl acetate synthesis over Pd-Au." *Catalysis Today*, in press.